

THESIS

---

Multi-Color Interferometry  
for Lock Acquisition of Laser Interferometric  
Gravitational-wave Detectors

---

BY  
KIWAMU IZUMI  
DEPARTMENT OF ASTRONOMY  
THE UNIVERSITY OF TOKYO

July, 2012



# Abstract

There have been worldwide efforts to directly detect gravitational-wave (GW) for the first time. The highest sensitivity to mid-frequency GWs at around 100 Hz has been achieved by the laser interferometric detector. However the direct detection has not been yet achieved. To increase the detection rate by enlarging the observable volume in the Universe, the km-scale interferometers are currently being upgraded or constructed. It is expected that these interferometers will be able to detect GWs with a sufficient detection rate of a few events per year.

The modern GW interferometer is a variant of the Michelson interferometer enhanced by the addition of the optical cavities in the arms as well as the input and output sides of the Michelson interferometer. The optical lengths of those cavities must be controlled against the seismic vibration such that the proper interferometric condition is always maintained.

To operate such a complicated interferometer, one of the big challenges is lock acquisition, in which the interferometer is brought from the initial state, where the lengths are at arbitrary values and hence random interference happens, to the final state, where the lengths are interferometrically controlled at the operating point. During lock acquisition essentially there are no reliable optical signals that provide the proper lengths information until all the lengths are simultaneously on the operating point. This is due to the fact that the response of the interferometer is highly nonlinear and also the optical cavities are coupled to each other. These facts make lock acquisition difficult and strongly hinder the lock acquisition progression. Thereby it can potentially result in a serious reduction in the observational duty cycle of the upcoming km-scale interferometers.

In order to address the difficulty, a new multi-color interferometric technique has been proposed. In the technique frequency-doubled auxiliary lasers, phase locked to the main interferometer laser, is introduced to serve as a sensor which can readout only the length of the arm Fabry-Pérot cavities with a significantly wider linear range. Therefore the nonlinearity is mitigated. This technique enables us to control the arm lengths independently of the condition of the rest of the interferometer. Therefore it decouples the arm cavities from the rest of the interferometer and consequently enables us to perform a more deterministic and repeatable lock progression.

In this thesis an experimental demonstration of the multi-color interferometric technique, conducted in a 40-meter baseline prototype interferometer,

---

is presented. It is shown that the resultant stability in the arm length successfully surpasses the requirement. In addition to it, the other important function — arbitrarily tuning the length of the arm cavity — is demonstrated. Moreover a noise study has been performed by utilizing a linear control model. According to the noise study the feasibility of the technique in the km-scale interferometer is discussed and confirmed.

Thus the use of this technique should allow for a significantly higher duty cycle in the upcoming km-scale interferometer.

# Contents

<b>Acronyms</b>	<b>xiii</b>
<b>Introduction</b>	<b>1</b>
<b>1 Background</b>	<b>5</b>
1.1 Gravitational-wave	6
1.1.1 Introduction	6
1.1.2 GW as a Solution of Einstein's Equation	6
1.1.3 Polarization	7
1.1.4 Radiation	9
1.2 Astrophysical Gravitational-wave Sources	12
1.2.1 Coalescence of Compact Binary Stars	12
1.2.2 Spin of Compact Stars	13
1.2.3 Supernovae	15
1.2.4 Stochastic Gravitational-wave Background	15
1.3 Terrestrial Laser Interferometers	15
1.3.1 Introduction	15
1.3.2 The 2nd Generation Interferometers	16
1.3.3 Working Principle	17
1.3.4 Enhancement by the Fabry-Pérot Arms	21
1.3.5 Further Improvement with the Dual-Recycling	25
1.3.6 Worldwide Detector Network	28
1.4 Length Sensing and Control of the Interferometer	30
1.4.1 Introduction	30
1.4.2 Various Noise Sources	30
1.4.3 Null Measurement due to the Length Control	32
1.5 Summary of the Chapter	33
<b>2 Basics in Laser Interferometry</b>	<b>35</b>
2.1 Michelson Interferometer	35
2.2 Optical Cavities	36
2.2.1 Overview	36
2.2.2 Static Responses	36
2.2.3 Characteristic Quantities	39
2.2.4 Dynamical Responses	40
2.3 Frontal Modulation Scheme for Length Sensing	44

## CONTENTS

---

2.3.1	Introduction . . . . .	44
2.3.2	A Primitive Picture . . . . .	45
2.3.3	The Sideband Picture . . . . .	46
2.3.4	Photo Detection and Demodulation . . . . .	47
2.4	Examples of the Frontal Modulation Scheme . . . . .	49
2.4.1	A Single Fabry-Pérot Cavity . . . . .	49
2.4.2	Michelson Interferometer . . . . .	52
2.5	Third Harmonic Demodulation Technique . . . . .	55
2.6	Second-Harmonic Generation . . . . .	55
2.6.1	Overview . . . . .	55
2.6.2	Conversion Efficiency . . . . .	56
2.6.3	Phase-Matching and Coherence Length . . . . .	57
2.6.4	Quasi Phase-Matching with Periodically Poled Crystal . . . . .	58
2.6.5	SHG with a Focused Gaussian Beam . . . . .	62
2.7	Summary of the Chapter . . . . .	66
<b>3</b>	<b>Multi-Color Interferometry for Lock Acquisition</b> . . . . .	<b>67</b>
3.1	Introduction . . . . .	68
3.1.1	Lock Acquisition . . . . .	68
3.1.2	Example : Single Fabry-Pérot Cavity . . . . .	68
3.1.3	Toward the 2nd Generation Interferometer and Beyond . . . . .	70
3.2	Difficulties in a Single Fabry-Pérot Cavity . . . . .	71
3.2.1	Kinematic Limit . . . . .	71
3.2.2	Distortion in Signals . . . . .	72
3.2.3	Acquisition Failure . . . . .	72
3.2.4	Mitigations . . . . .	72
3.3	Difficulties in Multiply-Coupled Optical Cavities . . . . .	74
3.3.1	Overview . . . . .	74
3.3.2	Length Degrees of Freedom . . . . .	75
3.3.3	The Lock Acquisition Progression . . . . .	77
3.3.4	Obstruction from the Arm Cavities . . . . .	78
3.3.5	Arm Length Stabilisation as a Mitigation . . . . .	80
3.4	Multi-Color Interferometry for Arm Length Stabilisation . . . . .	81
3.4.1	Overview . . . . .	81
3.4.2	Auxiliary Lasers for Sensing the Arm Length . . . . .	82
3.4.3	The Main Laser as a Reference . . . . .	83
3.4.4	Arm Length Stabilisation . . . . .	84
3.4.5	Requirements . . . . .	86

3.5	Full Lock Acquisition with the Multi-Color Interferometry . . .	87
3.5.1	The Planned Lock Acquisition Process . . . . .	87
3.6	Summary of the Chapter . . . . .	89
<b>4</b>	<b>The 40-meter Prototype Interferometer</b>	<b>91</b>
4.1	Overview . . . . .	91
4.2	Vacuum System . . . . .	92
4.3	Input Optics . . . . .	94
4.3.1	Main Laser Source . . . . .	94
4.3.2	Pre-Mode Cleaner . . . . .	96
4.3.3	Electro-Optic Phase Modulator . . . . .	97
4.3.4	13-meter Mode Cleaner . . . . .	98
4.3.5	Monitors . . . . .	98
4.4	Core Optics . . . . .	99
4.4.1	Dichroic Mirror Coatings . . . . .	101
4.5	Photo Detection System . . . . .	101
4.5.1	Photo Detectors . . . . .	101
4.5.2	Demodulation System . . . . .	102
4.6	Digital Control System . . . . .	103
4.6.1	Realtime Signal Processing . . . . .	104
4.6.2	Digital Control of the Interferometer . . . . .	105
4.7	Suspensions and Their Controls . . . . .	107
4.7.1	The Small Optic Suspension . . . . .	107
4.7.2	Local Controls . . . . .	107
4.8	Second-Harmonic Generation . . . . .	108
4.8.1	The Setup . . . . .	109
4.8.2	Adjustments . . . . .	109
4.9	Auxiliary Laser Setup . . . . .	110
4.9.1	Optical Layout . . . . .	111
4.9.2	Phase Modulation . . . . .	111
4.9.3	The Frequency Locking . . . . .	112
4.10	Summary of the Chapter . . . . .	113
<b>5</b>	<b>Demonstration of Arm Length Stabilisation</b>	<b>115</b>
5.1	Experimental Arrangement . . . . .	115
5.1.1	Single Arm Fabry-Pérot Cavity . . . . .	115
5.1.2	AUX Light Source and Frequency Doubling . . . . .	117
5.1.3	Delay-line Frequency Discriminator . . . . .	118

## CONTENTS

---

5.2	Automation of the Control Sequence . . . . .	119
5.2.1	Digital Control . . . . .	119
5.2.2	The Control Sequence . . . . .	120
5.2.3	Automation . . . . .	121
5.3	Demonstration of the Length Tunability . . . . .	124
5.4	Discussions and Summary of the Chapter . . . . .	124
5.4.1	Discussions . . . . .	124
5.4.2	Summary . . . . .	125
<b>6</b>	<b>Modeling and Noise Analysis</b>	<b>127</b>
6.1	Control Model . . . . .	127
6.1.1	AUX-Cavity Loop . . . . .	127
6.1.2	PSL-MC Loop . . . . .	129
6.1.3	Beat-note Detection . . . . .	129
6.1.4	Arm Length Servo . . . . .	131
6.1.5	PSL PDH Sensing . . . . .	131
6.2	Stability and Noise Analysis . . . . .	132
6.2.1	Fundamental Cavity Noise Sources . . . . .	132
6.2.2	Technical Noise Sources . . . . .	137
6.3	Scaling Noise Sources for aLIGO . . . . .	140
6.3.1	Residual Displacement in aLIGO . . . . .	140
6.4	Control Model Transfer Functions . . . . .	144
6.5	Discussions and Summary of the Chapter . . . . .	144
6.5.1	Discussions . . . . .	144
6.5.2	Summary . . . . .	145
<b>7</b>	<b>Conclusion and Future Directions</b>	<b>149</b>
7.1	Conclusion . . . . .	149
7.2	Future Directions . . . . .	149
7.2.1	Application of Multi-Color Interferometry . . . . .	149
7.2.2	Modern Controls . . . . .	151
<b>A</b>	<b>Characterization of the Dual-Recycled Michelson Interferometer</b>	<b>153</b>
A.1	Overview . . . . .	153
A.1.1	The Characterization List . . . . .	154
A.2	Interferometer as MIMO . . . . .	158
A.2.1	Sensing Matrix . . . . .	158

## CONTENTS

---

A.2.2	Radar Chart . . . . .	159
A.2.3	Output Matrix . . . . .	160
A.3	Experimental Arrangement . . . . .	162
A.3.1	Macroscopic Cavity Lengths . . . . .	162
A.3.2	Schnupp Asymmetry . . . . .	163
A.3.3	Second Harmonic Demodulation for Power Monitor . . . . .	164
A.4	Interferometer Modeling . . . . .	164
A.4.1	Model Interferometer . . . . .	164
A.5	Characterization of the 40-meter Prototype . . . . .	166
A.5.1	Measurement of Schnupp Asymmetry . . . . .	166
A.5.2	Calibration of Coil Magnet Actuators . . . . .	167
A.5.3	Measurement of the Power Recycling Gain . . . . .	169
A.5.4	Verification of the Sensing Matrix . . . . .	170
<b>B</b>	<b>Triple Resonant EOM</b>	<b>173</b>
B.1	Modulation Methods . . . . .	173
B.2	The Circuit . . . . .	174
B.2.1	Optimally Coupled EOM . . . . .	174
B.2.2	The Designed Circuit . . . . .	175
B.3	Performance Test . . . . .	176
	<b>Acknowledgement</b>	<b>179</b>



# List of Figures

1.1	Polarization of gravitational-wave . . . . .	8
1.2	The chirp signal from a $1.4 M_{\odot}$ - $1.4 M_{\odot}$ neutronstar binary, calculated. . . . .	12
1.3	The maximum amplitude of the know pulsars . . . . .	14
1.4	Typical configuration of the 2nd generation laser interferometer	17
1.5	The Michelson interferometer as a gravitational-wave detector	18
1.6	Frequency response of the Michelson and Fabry-Pérot Michelson interferometers . . . . .	20
1.7	The Fabry-Pérot Michelson interferometer as a gravitational-wave detector . . . . .	22
1.8	The Fabry-Pérot arm cavity formed by two mirrors . . . . .	22
1.9	Configurations for the recyclings and resonant sideband extraction schemes . . . . .	26
2.1	Schematic view of the Fabry-Pérot cavity. . . . .	37
2.2	Static response of an FP cavity . . . . .	38
2.3	Bode plot of the dynamical responses . . . . .	41
2.4	Equivalent diagram of the noise transfer in an FP cavity . . . . .	43
2.5	Primitive picture of the frontal modulation scheme . . . . .	45
2.6	Phase-modulated field in the sideband picture . . . . .	46
2.7	Setup for an FP cavity with the Pound-Drever-Hall scheme . . . . .	50
2.8	Intra-cavity power and PDH signal in the vicinity of a resonance	51
2.9	Phasor picture of frontal modulation sensing . . . . .	53
2.10	Periodically poled crystal . . . . .	59
2.11	Second-harmonic power as a function of travel distance through a crystal . . . . .	59
2.12	Conversion efficiency of a PPKTP crystal as a function of temperature . . . . .	61
2.13	Conversion efficiency of a PPKTP crystal as a function of the beam waist size . . . . .	64
3.1	Setup for locking a single suspended Fabry-Pérot cavity. . . . .	68
3.2	Intra-cavity power and PDH signal of an FP cavity as a function of displacement . . . . .	69
3.3	Definition of the canonical length degrees of freedom . . . . .	75
3.4	Simplified diagram of the DRFPMI locking . . . . .	78

## LIST OF FIGURES

---

3.5	Intra-cavity power against displacement in the ETM position . . .	80
3.6	Schematic view of the multi-color interferometry setup for arm length stabilisation. . . . .	82
3.7	The planned full lock acquisition steps. . . . .	88
4.1	Schematic of the optical layout of the 40 meter prototype . . .	92
4.2	Picture of the 40 meter prototype facility . . . . .	93
4.3	Schematic view of the vacuum envelope . . . . .	93
4.4	Schematic of the optical layout for the input optics . . . . .	95
4.5	Spectrum of the incident field, measured . . . . .	96
4.6	Setup for frequency stabilisation of the main laser . . . . .	98
4.7	Bode plot of the PSL frequency stabilisation loop . . . . .	99
4.8	Picture of one of the core optics . . . . .	100
4.9	Spectral reflectivity of one of the dichroic cavity mirrors . . .	100
4.10	Block diagram of the demodulation system . . . . .	101
4.11	Block diagram of the digital realtime control . . . . .	104
4.12	Schematic view of the small optic suspension . . . . .	106
4.13	Schematic view of the OSEM . . . . .	106
4.14	Schematic view of an optical lever setup . . . . .	108
4.15	The beam radii of the incident beam on one of the SHG crystals	109
4.16	Second harmonic power as a function of temperature, measured	110
4.17	Schematic of the auxiliary laser setup . . . . .	111
5.1	Experimental setup . . . . .	116
5.2	Schematic of delay-line frequency discriminator . . . . .	118
5.3	Schematic of the arm length stabilisation loop . . . . .	120
5.4	Sequence of the arm length control . . . . .	121
5.5	Control flow chart. . . . .	122
5.6	Acquisition of the arm length stabilisation servo in time series	123
5.7	Sweep of cavity length control offset . . . . .	125
6.1	Block diagram of the model of control scheme . . . . .	128
6.2	Bode plot of control model transfer function . . . . .	130
6.3	Residual displacement noise at 1064 nm and noise budget of the locked cavity . . . . .	133
6.4	Expected residual displacement in aLIGO arm cavity and noise budget . . . . .	141

---

## LIST OF FIGURES

---

6.5	Expected residual displacement in aLIGO arm cavity and noise budget with the improvements . . . . .	142
A.1	PRC intra-cavity power of two sidebands against the macroscopic scan of the PRC length . . . . .	155
A.2	Radar chart for visualization of input matrix . . . . .	159
A.3	Experimental arrangement of the DRMI characterization . . . . .	161
A.4	Time series of the DRMI lock . . . . .	165
A.5	Sensing matrix of the DRMI, simulated . . . . .	166
A.6	AC response of the coil magnet actuators . . . . .	168
A.7	Contour maps of the mode overwrap and loss in the power recycling cavity . . . . .	169
A.8	Sensing matrix of the DRMI, measured . . . . .	171
B.1	Equivalent circuit of an EOM . . . . .	174
B.2	Schematic of the designed circuit for the triple resonant EOM . . . . .	175
B.3	Modulation depth as a function of frequency, measured. . . . .	177



# Acronyms

Acronym	Definition
1G	1st generation
2G	2nd generation
aLIGO	advanced LIGO
ADC	Analog to Digital Convertor
ALS	Arm Length Stabilisation
AS	Anti Symmetric
AUX	Auxiliary
BPM	Bulk birefringent Phase Matching
BS	Beam Splitter
CARM	Common motion in the Arms
DAC	Digital to Analog Convertor
DARM	Differential Arm motion
DFD	Delay-line Frequency Discriminator
DOF	Degrees of Freedom
DRFPMI	Dual Recycled Fabry-Pérot Michelson Interferometer
DRMI	Dual Recycled Michelson Interferometer
EOM	Electro Optic Modulator
ET	Einstein Telescope
ETM	End Test Mass
FP	Fabry-Pérot
FSR	Free Spectral Range
FWHM	Full Width at Half Maximum
GW	Gravitational-wave
IIR	Infinite Impulse Response
ISCO	Innermost Stable Circular Orbit
ITM	Input Test Mass
I-phase	In-phase
KTP	KTiOPO <sub>4</sub>
LSC	Length Sensing and Control
MC	Mode Cleaner
MICH	Michelson
MIMO	Multiple Input and Multiple Output
MMT	Mode Matching Telescope
Nd:YAG	Nd doped Y <sub>3</sub> Al <sub>5</sub> O <sub>12</sub>

---

<b>Acronym</b>	<b>Definition</b>
NPRO	Non Planar Ring Oscillator
OSA	Optical Spectrum Analyzer
PD	Photo Detector
PDH	Pound-Drever-Hall
PLL	Phase-Locked Loop
PMC	Pre Mode Cleaner
PO	Pick Off
POP	Pick Off from Power recycling cavity
PP	Periodically Poled
PPKTP	Periodically Poled KTiOPO <sub>4</sub>
PRC	Power Recycling Cavity
PRCL	Power Recycling Cavity Length
PRM	Power Recycling Mirror
PSL	Pre-Stabilised Laser
QPD	Quadrant Photo Detector
Q-phase	Quadrature phase
QPM	Quasi-Phase Matching
RAM	Residual Amplitude Modulation
REFL	Reflection
RF	Radio Frequency
RFPD	Radio Frequency Photo Detector
RMS	Root Mean Square
RTP	RbTiOPO <sub>4</sub>
SHG	Second-Harmonic Generation
SPI	Suspension Point or Platform Interferometry
SRC	Signal Recycling Cavity
SRCL	Signal Recycling Cavity Length
SRM	Signal Recycling Mirror
THD	Third Harmonic Demodulation
TO	Thermo-Optic
VCO	Voltage Controlled Oscillator

---

# Introduction

First of all the purpose of this thesis is not only to present new scientific results but also to accelerate the commissioning works of the km-scale laser interferometric detectors that will be performed over the world in the coming years. So for the reason an independent topic is additionally presented in appendix A.

There have been worldwide efforts to directly observe gravitational-wave (GW) from astrophysical sources with the terrestrial laser interferometric detectors. GW was predicted by A. Einstein in 1918 [1] based on his general theory of relativity [2]. An indirect detection was performed by R. Hulse and J. Taylor [3, 4]. They have observed the binary pulsar PSR 1913+16 and found that the orbital period decreased as the GW was emitted from the system. In addition to it recently OJ 287, known as a quasar, agrees with a binary black hole model, system of which radiates GW [5], and thus this also supports the existence of GW. The importance of GW detection increases as our understanding of the Universe becomes deeper, but no direct observation was ever achieved over approximately a hundred year after the prediction.

In order to detect GWs so-called 1st generation interferometers such as TAMA [6], GEO [7], VIRGO [8] and LIGO [9] were built and operated over the past years and conducted several times of the observational runs. However none of them could detect GWs. Now the 2nd generation interferometers, such as advanced LIGO, KAGRA [10] and advanced VIRGO are being upgraded or constructed. Their sensitivity will be increased by a factor of approximately 10 compared with that of the 1st generation interferometers. They are strongly expected to detect GW from astrophysical sources with a detection rate of roughly a few events per year or even more [11]. Therefore once they are fully tuned and become online, they are to be hoped to make the first detection and hence open a new astronomical window — gravitational-wave astronomy.

The 2nd generation interferometer typically consists of a Michelson interferometer enhanced by the addition of a long Fabry-Pérot (FP) cavity in each arm as well as in the input and output sides of the Michelson interferometer, forming the Dual-Recycled Fabry-Pérot Michelson interferometer.

A challenge in the use of such a complicated interferometer is lock acquisition. Lock acquisition is a progression to bring the interferometer from the initial state, where all the optical lengths are at arbitrary values and hence a random interference happens, to the final state, where all the length are

## INTRODUCTION

---

brought to the operating point and hence the desired interference is achieved.

Difficulties in lock acquisition come from two facts. One is that the response of the interferometer is highly nonlinear and the other one is that the optical cavities are optically coupled to each other. Once all the optical lengths are brought to the vicinity of their operating points, the response becomes linear. However until then, there are no reliable signals that provide the proper length information. Therefore the lock acquisition process is not straightforward.

In order to address the issues and make the process robust, a new multi-color interferometric technique has been proposed and chosen to be a standard technique in advanced LIGO and KAGRA. The technique utilizes frequency-doubled auxiliary Nd:YAG lasers, phase locked to the main laser source to serve as a new sensor for the arm lengths [12] with a significantly wider linear range. Thus the technique mitigates the issues related to the nonlinearity. Since only the arm cavity lengths are sensed independently of the rest of the interferometer, it allows us to bring the arm lengths to a value where the arms are decoupled from the rest of the interferometer. Therefore it mitigates also the issues related to the multiply-coupled optical cavities. As a consequence it enables us to perform a robust and repeatable lock progression.

In this thesis an experimental demonstration of the multi-color interferometric technique, conducted in a 40-meter baseline prototype interferometer, is presented. It is shown that the resultant stability in the arm length surpasses the requirement of about 1 nm. In addition to it, the other important function — arbitrarily tuning the length of the arm cavity — is demonstrated. Moreover a noise study has been performed by utilizing a linear control model, which allows us to estimate the contributions from various noise sources to the residual arm stability. According to the noise study the feasibility of the technique in the km-scale interferometer is discussed and confirmed. Thus the use of this technique should allow for a significantly higher duty cycle in the upcoming 2nd generation interferometers.

The following paragraphs attempt to explain the contents of this thesis and the contribution of the author to the research presented in this thesis.

Chapter 1 briefly describes the background of the research. It includes the derivation of GW, its possible astrophysical sources and an introduction of the laser interferometric detectors.

Chapter 2 describes a set of the relevant basics for the laser interferometry, such as the interferometric devices, length readout technique and second-

harmonic generation. There are no new results or original researches in this chapter.

Chapter 3 introduces lock acquisition of the GW interferometer and the multi-color interferometric technique, which is the main topic of this thesis. The multi-color technique was proposed by the collaborators of the author.

Chapter 4 explains the 40-meter baseline prototype interferometer, in which all the experiments described in this thesis have been conducted. The prototype is a project led by the LIGO laboratory of California Institute of Technology. The prototype undertook a major upgrade from 2009 for approximately a year. During the upgrade the author was one of the main persons who implemented the necessary optical hardwares, prepared and installed the digital control system and analog circuits. The tuning of the local control and global control was also done largely by the author.

Chapter 5 describes the experimental demonstration of the arm length stabilisation using the multi-color interferometry. The hardware design and implementation were done largely by the author with a help from the collaborators, listed as coauthors in reference [13]. The automated locking sequence, implemented for the prototype test, is an original work done by the author. Although the working principle had been already demonstrated [12] in a short cavity setup, the experimental test presented in this thesis is the first test where the multi-color technique was applied to a realistic GW interferometer.

Chapter 6 describes a noise analysis for the prototype and aLIGO to confirm the feasibility of the use of the technique in aLIGO. It utilizes a linear control model, which allows to estimate the contribution of various noise sources to the residual length motion. The author built the model, measured and estimated the possible noise sources, and analyzed the noise contributions. The resultant noise budget of the prototype test, which represents the contributions from the possible noise sources, is presented for the first time by the author.

Appendix A is dedicated for the commissioning of the dual-recycled Michelson interferometer, which is the other key of the 2nd generation interferometer. This project was led by the author. Although the dual-recycling itself is not a new technique, the author attempted to fully characterize the dual-recycled interferometer that is designed for aLIGO in prior to the commissioning of the aLIGO interferometers. Tuning of lock acquisition of the dual-recycled Michelson interferometer was done by the author. The aLIGO-style dual-recycled Michelson interferometer was locked for the first time by the author.

## INTRODUCTION

---

Appendix [B](#) describes a new electro-optic hardware called the triple resonant electro-optic phase modulator. The original idea was proposed by the collaborators of the author. A further analysis, tuning and installation have been done by the author.

# 1

## Background

Detection of gravitational-wave (GW) is a significantly challenging objective because the interaction of gravity with masses is inherently weak. In fact creation of GW with a detectable amplitude in a laboratory is impossible with the current available technologies. Therefore it is natural for us to expect radiation of GWs from astronomical and cosmological sources, system of which can be extremely massive and highly accelerated. From this point of view astronomy and GW are inseparable. Moreover it is expected that observations of GWs from astronomical sources will give us unique information of the Universe. This is essentially because GWs are unaffected by the matter they encounter. So that the direct observation of GWs will open a new window to the Universe — this window is called *Gravitational-wave Astronomy*.

Nowadays the most sensitive detector at around 100 Hz is the laser interferometric GW detector. The sensitivity of the interferometer has been continuously improved over the course of the years. Therefore the laser interferometer is expected to make the first detection and successively pioneer GW astronomy.

This chapter is dedicated to explaining GW astronomy and the laser interferometric detector as a background of this thesis. In section 1.1 we briefly review the derivation of GW based on the general theory of relativity. Then the polarization of GW is described by discussing an example. Section 1.2 describes possible astrophysical sources which are regarded as main targets of the leaser interferometric detectors. In section 1.3 the laser interferometric detector, which is the main topic of this thesis, is introduced. Section 1.4 gives a short introduction for the length sensing and control of the GW interferometer.

### 1.1 Gravitational-wave

---

#### 1.1.1 Introduction

GW is a ripple of space-time and propagates at the speed of light. On the basis of the general theory of relativity [2], GW was predicted by A. Einstein in 1918 [1].

In Newton's theory of gravitation, there was no such waves. In Newton's theory once the spatial distribution of masses are given, the gravitational potential  $\phi$  induced by them is *instantaneously* determined. This is because that Poisson's equation doesn't contain a time dependent term :

$$\Delta\phi = 4\pi G\rho, \tag{1.1}$$

where  $G$  is the gravitational constant and  $\rho$  is the mass density. Therefore it doesn't allow  $\phi$  to propagate as a wave.

On the other hand, GW is a natural consequence of the general theory of relativity. In the theory, gravitation is considered as distortion in space-time, expressed by a physical quantity called the metric instead of  $\phi$ . Moreover the metric follows Einstein's equation which contains the second derivative of the metric with respect to time. Thus it tells us that the metric can evolve as a function of time. In fact a small perturbation in the metric can propagate as a wave through space-time — the wave is known as GW.

#### 1.1.2 GW as a Solution of Einstein's Equation

Here we briefly review the derivation of GW. GW can be derived as a solution of Einstein's equation when a small perturbation in space-time is introduced. For more details of the derivation, see reference [14] for instance.

The interval of two separated events in space-time is described with the metric tensor  $g_{\mu\nu}$  as,

$$ds^2 = g_{\mu\nu}dx^\mu dx^\nu, \tag{1.2}$$

where Greek indices run from 0 to 3, so that  $\mu, \nu = 0, 1, 2, 3, 4$ . With this notation space-time can be simply expressed by  $x^\mu = (ct, x, y, z)$ .

The most important equation in the theory, Einstein's equation, is expressed by

$$R_{\mu\nu}(g_{\mu\nu}) - \frac{1}{2}g_{\mu\nu}R(g_{\mu\nu}) = \frac{8\pi G}{c^4}T_{\mu\nu}, \tag{1.3}$$

## 1.1. GRAVITATIONAL-WAVE

---

where  $R_{\mu\nu}$  is the Ricci tensor,  $R = g^{\mu\nu} R_{\mu\nu}$  is the Ricci scalar curvature, and  $T_{\mu\nu}$  is the stress-energy-momentum tensor. Since  $R_{\mu\nu}$  and  $R$  are functions of  $g_{\mu\nu}$ , it is clear that the lefthand side of the equation is a function of  $g_{\mu\nu}$ . Beauty of this equation is that the equation connects gravity  $g_{\mu\nu}$  (or distortion in space-time) with the energy  $T_{\mu\nu}$  (or presence of masses).

To derive GW we let the metric deviate from the flat space-time, the Minkowsky space-time. The metric can be expressed by the sum of the first order perturbation  $h_{\mu\nu}$  and the Minkowsky metric  $\eta_{\mu\nu}$ :

$$g_{\mu\nu} = \eta_{\mu\nu} + h_{\mu\nu}. \quad (1.4)$$

Considering vacuum, where  $T_{\mu\nu} = 0$ , then applying the above equation to equation (1.3), and neglecting higher order terms while leaving the first order terms of  $h$ , one can obtain the linearized Einstein's equation,

$$\left( -\frac{1}{c^2} \frac{\partial^2}{\partial t^2} + \frac{\partial^2}{\partial x_i^2} \right) h_{\mu\nu} = 0. \quad (1.5)$$

This is a three-dimensional wave equation describing the propagation of GW  $h_{\mu\nu}$ . It indicates that GW propagates at the speed of light  $c$ .

When we choose a spatial coordinate such that a GW travels in the  $z$  direction, the plane wave solution can be summarized into the following expressions,

$$h_{\mu\nu} = A_{\mu\nu} \exp(i\omega_g(t - z/c)), \quad (1.6)$$

$$A_{\mu\nu} = \begin{pmatrix} 0 & 0 & 0 & 0 \\ 0 & h_+ & h_\times & 0 \\ 0 & h_\times & -h_+ & 0 \\ 0 & 0 & 0 & 0 \end{pmatrix}, \quad (1.7)$$

where  $\omega_g$  is the angular frequency of the GW,  $h_+$  and  $h_\times$  are independent constants. As we will see in the next subsection, they denote two independent polarizations.

### 1.1.3 Polarization

Consider a case, where two free particles are placed at spatially separated locations — one at the origin of the coordinate and the other at  $x^i = (L, 0, 0)$ .

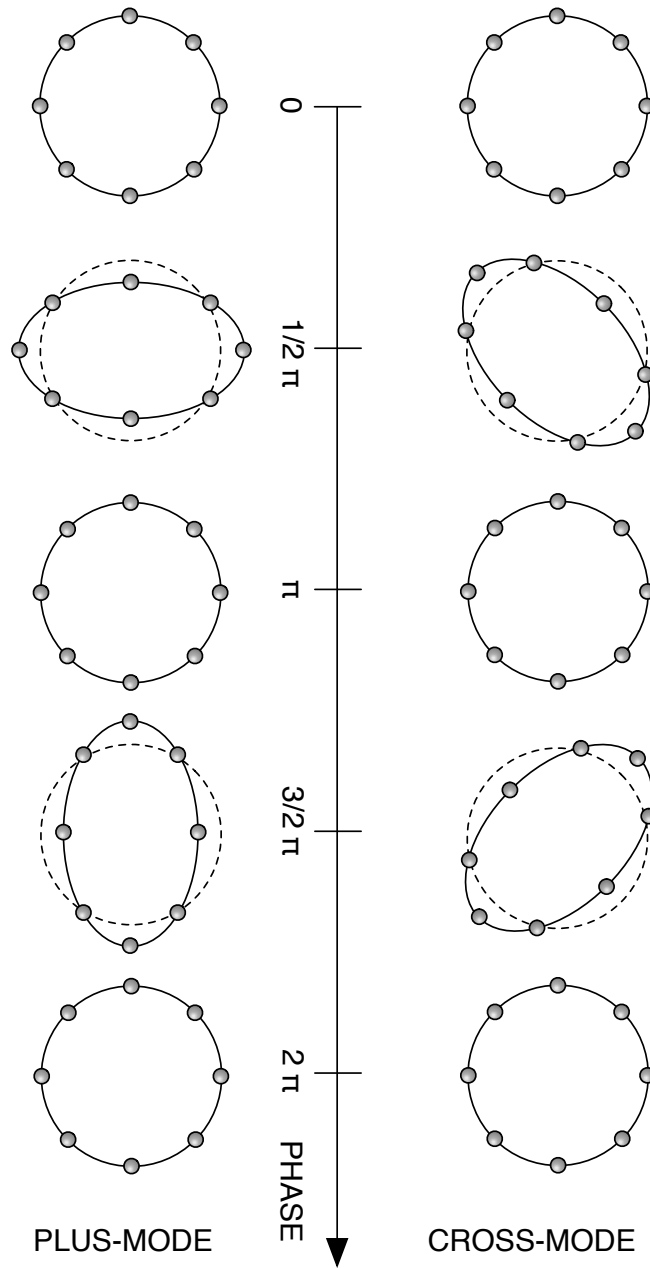


Figure 1.1: Polarization of gravitational-wave. (Left) point masses displaced by the plus-mode GW. (Right) point masses displaced by the cross-mode GW.

## 1.1. GRAVITATIONAL-WAVE

---

Suppose that each of them is at rest initially, and GW passes along the  $z$ -axis. The proper distance between them  $L'$  can be expressed by

$$L' \equiv \int |ds^2|^{1/2} = \int_0^L |g_{11}|^{1/2} dx \approx L + \frac{1}{2} h_{11} L. \quad (1.8)$$

Therefore GW varies the proper distance as it passes through. The amount of change in the distance  $\Delta L \equiv L' - L$  is in proportion to both the initial distance  $L$  and amplitude  $h$ .

As shown in equation (1.7), there are two independent polarizations in GWs — amplitude of which are expressed by  $h_+$  and  $h_\times$ , and they are referred to as *plus*- and *cross*-mode respectively. To understand the characteristic of those modes, consider a similar gedanken experiment in which a plane wave passes along the  $z$ -axis through a number of free particles arranged on the  $x$ - $y$  plane. According to equation (1.8) if a proper distance between them was initially at  $L^i = (L^x, L^y, 0)$ , the displacement  $\Delta L$  is found to be

$$\begin{pmatrix} \Delta L^x \\ \Delta L^y \end{pmatrix} = \frac{1}{2} \begin{pmatrix} h_+ & h_\times \\ h_\times & -h_+ \end{pmatrix} \begin{pmatrix} L^x \\ L^y \end{pmatrix} \exp(i\omega_g(t - z/c)), \quad (1.9)$$

$$= \frac{1}{2} h_+ \begin{pmatrix} L^x \\ L^y \end{pmatrix} e^{i\omega_g(t-z/c)} + \frac{1}{2} h_\times \begin{pmatrix} L^y \\ L^x \end{pmatrix} e^{i\omega_g(t-z/c)}. \quad (1.10)$$

Figure 1.1 illustrates the response of free particles to GW for both the plus- and cross-modes. It is apparent that the plus mode distorts space and makes their spatial arrangement a “plus”-shape, while the cross mode makes it a “cross”-shape.

### 1.1.4 Radiation

#### Analogy to Electro-Magnetic Radiation

GW can be radiated by masses as they accelerate similarly to the radiation of electro-magnetic waves which are induced by a charged particle as it accelerates. However a big difference is that the radiation of GW requires a quadrupole (or higher) moment instead of a dipole moment which is the leading term for the electro-magnetic radiation.

To discuss the difference further, quote the Larmor formula as an example. The formula indicates that the luminosity of an electro-magnetic wave  $L_e$  is

## CHAPTER 1. BACKGROUND

---

given by

$$L_e = \frac{2}{3c^2} \ddot{\mathbf{d}}^2, \quad (1.11)$$

where  $\mathbf{d}$  is the sum over the electric dipole moment of charged particles, so that  $\mathbf{d} = \sum_i q_i \mathbf{r}_i$ . It is clear that the radiation of electro-magnetic wave is intimately related to the time-evolution of the dipole moment.

Now the same argument is applied to the radiation of GW. Considering the dimension of the physical units in equation (1.11), one would end up with the GW luminosity  $L_g$  in the following form,

$$L_g \propto \frac{G}{c^3} \ddot{\mathbf{d}}^2, \quad (1.12)$$

$$\ddot{\mathbf{d}} = \sum_i m_i \ddot{\mathbf{r}}_i = \sum_i \dot{\mathbf{P}}_i, \quad (1.13)$$

where  $\mathbf{P}_i$  is the kinematic momentum of  $i$ -th particle. Instead of charged particles, the kinematic moment is introduced since GW is generated from masses. However the kinematic momentum is always conserved in an isolated system. It means that the kinematic dipole  $\mathbf{d}$  doesn't evolve as a function of time and hence no GW can be radiated by a kinematic dipole moment.

The next lowest moment is the quadrupole moment and in fact this turns out to be the leading term for radiating GWs. By introducing the mass quadrupole moment  $I_{jk}$ , a GW version of the Larmor formula [15] can be expressed by,

$$L_g = \frac{1}{5} \frac{G}{c^5} \langle (\ddot{I}_{jk})^2 \rangle, \quad (1.14)$$

$$I_{jk} \equiv \sum_A m_A \left[ x_j^A x_k^A - \frac{1}{3} \delta_{jk} (x^A)^2 \right], \quad (1.15)$$

where  $A$  represents the label of  $A$ -th particle. Therefore radiation of GW requires a quadrupole moment so as to evolve as a function of time.

### Order Estimation of Radiated Energy

Here we estimate the amount of the energy radiated as GWs based on equation (1.14). The third derivative of the quadrupole moment with respect to time has an order of

$$\ddot{\ddot{I}}_{jk} \sim \frac{MR^2}{T^3} \sim \frac{Mv^3}{R}, \quad (1.16)$$

---

## 1.1. GRAVITATIONAL-WAVE

where  $M, R, T, v$  are the characteristic mass, spatial size, time scale and velocity of a system. Plugging the above approximation into equation (1.14), one can obtain

$$L_g \sim 1.8 \times 10^{58} [\text{erg/s}] \left( \frac{r_{\text{sch}}}{R} \right)^2 \left( \frac{v}{c} \right)^6, \quad (1.17)$$

where  $r_{\text{sch}}$  is the Schwarzschild radius defined by  $r_{\text{sch}} = 2GM/c^2$ .

From a practical point of view, it is reasonable to think about an astronomical system, which is usually bounded by its self-gravity. In this case the kinetic energy and gravitational potential are comparable, so that

$$Mv^2 \sim \frac{GM^2}{R}. \quad (1.18)$$

With this relation, the luminosity (1.17) can be rewritten as

$$L_g \sim 2.3 \times 10^{57} [\text{erg/s}] \left( \frac{r_{\text{sch}}}{R} \right)^5. \quad (1.19)$$

This result indicates that the size of the object is a matter for the GW luminosity when an astronomical system is of interest. This is exactly the reason why the compact stars, such as black holes and neutron stars, are considered as the main GW sources.

### Order Estimation of Amplitudes

Lastly we estimate the order of the amplitude  $h$  based on the approximation [15]:

$$h \sim \frac{r_{\text{sch}}}{r} \left( \frac{v}{c} \right)^2, \quad (1.20)$$

where  $r$  is the distance between the system and an observer. We can parameterize the emission efficiency of GW by writing,

$$\varepsilon \sim \left( \frac{r_{\text{sch}}}{R} \right)^{7/2}. \quad (1.21)$$

Plugging the above equation into equation (1.20), we obtain the following order estimation,

$$h \sim \varepsilon^{2/7} \frac{r_{\text{sch}}}{2r} \sim 1.5 \times 10^{-21} \left( \frac{\varepsilon}{0.1} \right)^{2/7} \frac{(M/M_\odot)}{(r/17 \text{ Mpc})}. \quad (1.22)$$

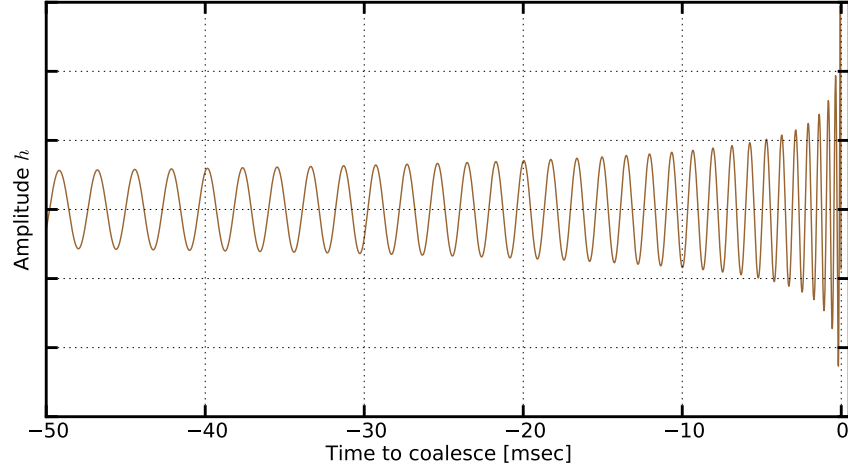


Figure 1.2: The chirp signal from a  $1.4 M_{\odot}$ - $1.4 M_{\odot}$  neutronstar binary, calculated.

The distance  $r$  is scaled by that from the Earth to the Virgo cluster of about 17 Mpc. Even if an optimistic efficiency of  $\varepsilon = 10\%$  is assumed, the amplitude of the GW from a system as heavy as  $M_{\odot}$  is still extremely small. For instance such a GW displaces the proper distance between two free masses, located apart by 4 km, by approximately  $6 \times 10^{-18}$  m according to the relation  $\Delta L = hL$ .

## 1.2 Astrophysical Gravitational-wave Sources

---

In this section we briefly review what kind of GW sources are expected for the terrestrial laser interferometric detectors. For some more details see reference [16].

### 1.2.1 Coalescence of Compact Binary Stars

A binary system, formed by two compact stars such as a black hole, neutronstar and white dwarf are thought to be a main candidate of the GW sources. Its wave form, known as the *chirp* signal, is predictable and thereby they are

## 1.2. ASTROPHYSICAL GRAVITATIONAL-WAVE SOURCES

---

considered as a promising GW source. Figure 1.2 shows a calculated chirp signal from a binary system formed by two of  $1.4 M_{\odot}$  neutronstars.

As shown in figure 1.2, the frequency of a chirp GW signal  $f_g$  grows up as a function of time. This is a consequence of the fact that the angular momentum of the system is deposited to the GW radiation and hence the separation distance of the starts gradually and monotonically becomes smaller. The frequency evolution of a chirp signal can be approximated by

$$f_g(\tau) \approx 134 \text{ Hz} \left( \frac{1.21 M_{\odot}}{\mathcal{M}} \right)^{5/8} \left( \frac{1 \text{ s}}{\tau} \right), \quad (1.23)$$

$$\mathcal{M} \equiv \frac{(m_1 m_2)^{3/5}}{(m_1 + m_2)^{1/5}}, \quad (1.24)$$

where  $\tau$  is the time to coalescence of the starts,  $\mathcal{M}$  is the chirp mass defined by the masses of the binary starts  $m_1$  and  $m_2$ .

When the orbital radius becomes smaller than the innermost stable circular orbit (ISCO), where stable circular orbits are no longer allowed, two stars eventually plunge toward each other and coalesce. For instance a neutronstar-neutronstar binary is expected to reach a frequency of about 800 Hz when they are at the ISCO.

Additionally such binary systems are to be hoped to serve as a standard siren [17], which is an analogy to the standard candles used in the electromagnetic wave observations. Once a chirp signal is detected, the amplitude provides the information of the luminosity distance. On the other hand, the frequency of the signal gives the information about the red shift. Therefore it allows one to perform cosmological measurement.

### 1.2.2 Spin of Compact Stars

Spinning compact starts, such as neutronstarts, are expected to be sources of a continuous GW, frequency of which can be rather stable. In order for a neutronstar to radiate GW by the spin, the mass density must not be axisymmetric about the spin axis because an axisymmetric system doesn't have a quadrupole moment.

The expected GW amplitude from a spinning rigid object can be estimated as

$$h \approx 1.06 \times 10^{-25} \left( \frac{\epsilon}{10^{-6}} \right) \left( \frac{I}{10^{38} \text{ kg m}^2} \right) \left( \frac{10 \text{ kpc}}{r} \right) \left( \frac{f_g}{1 \text{ kHz}} \right)^2. \quad (1.25)$$

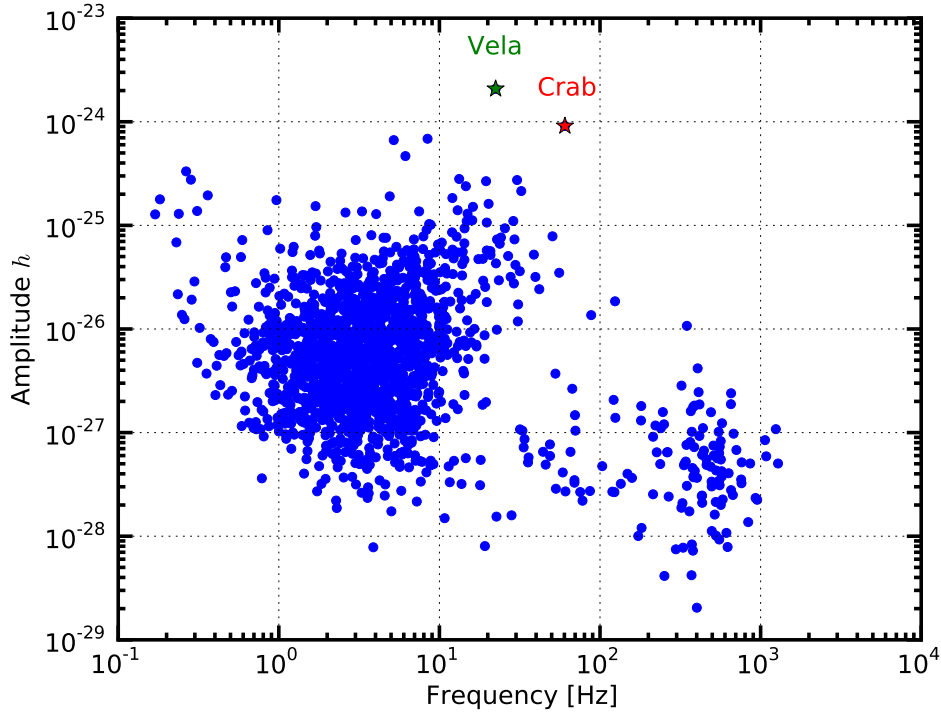


Figure 1.3: The maximum amplitude of the known spinning pulsars as a function of the gravitational-wave frequency. Red and green star-symbols represent that of the Crab and Vela pulsars.

where  $\epsilon$  is the ellipticity,  $I$  is the inertia along the spin axis. Note that the frequency of the GW is twice of the actual spin frequency  $f_{\text{spin}}$ , so that  $f_g = 2f_{\text{spin}}$ .

The spinning pulsars are targets of the terrestrial laser interferometric detectors as the frequency of some pulsars are in the observational band. Figure 1.3 shows the maximum allowed amplitude from the known pulsars [18], calculated under the assumption that the observed spin-down rate is fully dominated by the GW emission. They broadly spread across a frequency band from 100 mHz to 1 kHz. Recently upper limits have been set on the GW amplitudes from the Crab pulsar and some other pulsars by observations of the terrestrial laser interferometric detectors [19].

## 1.3. TERRESTRIAL LASER INTERFEROMETERS

---

### 1.2.3 Supernovae

It is natural to expect GW from a supernova explosion because it dramatically accelerates a large amount of masses in a short time scale. Due to the short time scale a burst signal is expected to be emitted from the supernova.

However the prediction of the waveform is rather difficult because the explosion mechanism is not well understood. Even though, we can estimate the order of the amplitude. Assuming that the mass of a system is about  $M_{\odot}$ , and the characteristic velocity of  $v/c \sim 0.1$ , we can estimate the amplitude according to equation (1.20),

$$h \sim 9.6 \times 10^{-20} \left( \frac{10 \text{ kpc}}{r} \right). \quad (1.26)$$

Therefore a supernova happening in our Galaxy can be a reasonable target. Most of the explosion models suggest that the frequency of such GW signals widely spread, but below 1 kHz. Therefore it is in the observational band of the terrestrial interferometers.

### 1.2.4 Stochastic Gravitational-wave Background

A stochastic background of GW is expected to arise from a superposition of a large number of unresolved GW sources of astrophysical and cosmological origin. It should carry unique signatures from the earliest epochs in the evolution of the Universe, inaccessible to standard astrophysical observations. Direct measurements of the amplitude of this background are therefore of fundamental importance for understanding the evolution of the Universe when it was younger than one minute.

Recently a simultaneous observation of the terrestrial laser interferometers has set an upper limit on the spectral density of the GW background and hence has set an upper limit on the cosmological energy density of GW [20].

## 1.3 Terrestrial Laser Interferometers

---

### 1.3.1 Introduction

Following after the famous J. Weber's resonant bar experiment in 1960's [21], people began developing the laser interferometer to detect GWs in the

## CHAPTER 1. BACKGROUND

---

early 1970's [22]. Over the course of decades the sensitivity of the terrestrial laser interferometers have been improved significantly and also a number of new schemes have been developed. A big advantage in the use of the laser interferometer is that the observational bandwidth can be much greater than that of the resonant bar detector. The bandwidth is typically chosen to be that from 10 Hz to 1 kHz.

In the past decade there have been worldwide efforts to detect GWs with km-scale interferometers. Currently the km-scale interferometers are being upgraded or newly constructed in order to increase the sensitivity by roughly a factor of 10 compared with the previously running interferometers. These new interferometers are called *2nd generation* (2G) interferometers.

### 1.3.2 The 2nd Generation Interferometers

So far people built a number of 100-meter and km-scale interferometers over the world. These interferometers are called *1st generation* (1G) interferometers. The 1G interferometer projects were successful in the sense that the designed sensitivity were achieved in the most of the frequency band after several years of continuous tuning and commissioning. Moreover they conducted several science runs successively.

Currently the 1G interferometers are being upgraded, and also some are newly being constructed. These interferometers will form a worldwide detector network and serve as the 2G interferometers to fully open GW astronomy. The 2G interferometers will enable us to detect a binary coalescence at a distance of approximately 200 Mpc with a sufficient signal-to-noise ratio. With such sensitivities the GW events will be detected with an event rate of a few events per year. Details on the estimation of the event rate are extensively summarized in reference [11].

The 2G interferometer typically consists of a Michelson interferometer enhanced by the addition of a long baseline Fabry-Pérot (FP) cavity to each arm of the Michelson interferometer, and of partial reflectors to both the input and output side of the Michelson interferometer. This particular configuration is called *the dual-recycled Fabry-Pérot Michelson interferometer* (DRFPMI). Figure 1.4 shows a schematic view of the typical 2G interferometer, that is the DRFPMI.

## 1.3. TERRESTRIAL LASER INTERFEROMETERS

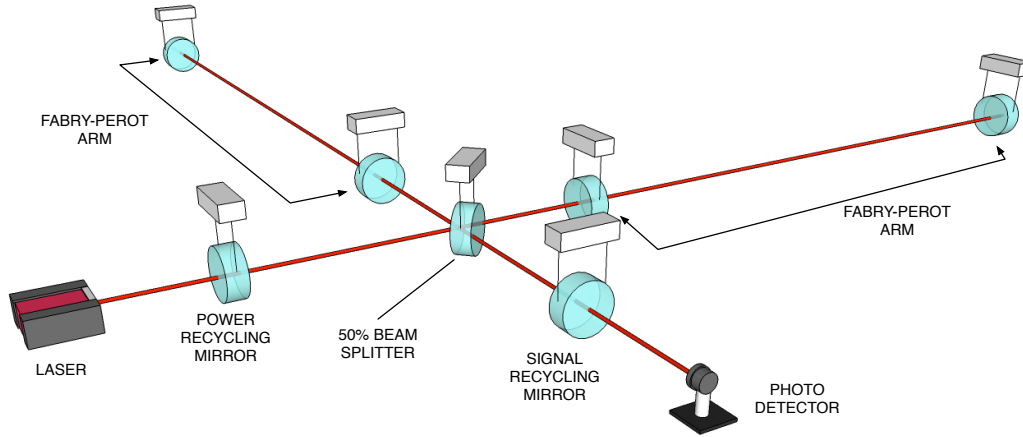


Figure 1.4: Schematic view of a typical configuration of the 2nd generation laser interferometer. The mirrors are suspended by wires.

### 1.3.3 Working Principle

#### Overview

As illustrated in figure 1.4 the 2G interferometer configuration is a variant of the Michelson interferometer with the mirrors suspended by wires. The suspended mirror not only provides seismic isolation but also makes the mirrors effectively free masses longitudinally with respect to the propagation direction of the laser beam in the observational frequency band.

When GW of a certain frequency passes through the interferometer, it modulates the microscopic optical length of the arm FP cavities by  $\Delta L$  as explained in section 1.1.3 at the same frequency. The microscopic lengths change is differential in two arms — one arm shrinks (expands) while the other expands (shrinks). As a result the GW changes the interference condition of the output laser field leaving off from the Michelson interferometer.

Therefore GWs can be observed as an intensity variation at a photo detector (PD) placed at the output side of the Michelson interferometer. If the wavelength of the GW is much longer than the arm lengths, the amount of the change is proportional to the macroscopic arm lengths  $L$ , so that

$$\Delta L \sim hL, \quad (1.27)$$

## CHAPTER 1. BACKGROUND

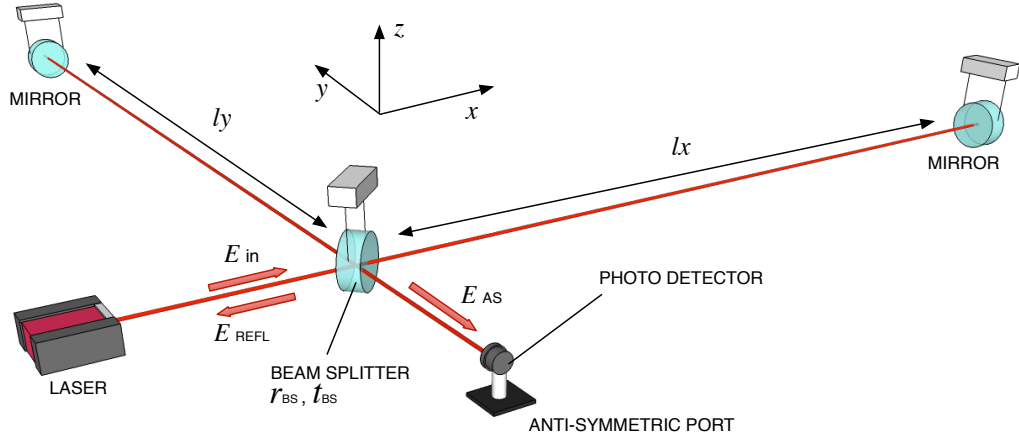


Figure 1.5: The Michelson interferometer as a gravitational-wave detector.

where  $h$  is the amplitude of the GW. Therefore it is natural to build a large interferometer to increase the sensitivity.

In the rest of this subsection, we see the detection principle of the Michelson interferometer. The detection principle holds true even for the DRFPMI.

### Detection with Michelson Interferometer

The Michelson interferometer is an interferometric device which enables us to readout the optical phase of laser field. It consists of a beam splitter (BS) and two end mirrors as shown in figure 1.5. Laser light illuminates the BS and is split into two paths at the BS — one is transmitted through it and the other is reflected. Each beam is reflected at each end mirror, then returns to the BS and is re-combined, resulting in interference. At the detection port, called anti-symmetric (AS) port, a PD observes the power of the electric field.

Suppose that GW, polarizing in the plus-mode, passes along the  $z$ -axis through the Michelson interferometer, placed in the  $x$ - $y$  plane as shown in figure 1.5. The interval (1.2) can be expressed by

$$ds^2 = -(cdt)^2 + (1 + h(t)) dx^2 + (1 - h(t)) dy^2 + dz^2. \quad (1.28)$$

Since the light travels along the world line of  $ds^2 = 0$ , the light traveling on

### 1.3. TERRESTRIAL LASER INTERFEROMETERS

---

the  $x$ -axis satisfies,

$$cdt = (1 + h(t)) dx. \quad (1.29)$$

Integrating  $dx$  over the round trip path from the BS to the end mirror, we obtain

$$\int_{t-\tau_x}^t \frac{t'}{\sqrt{1+h(t')}} dt \approx \int_{t-\tau_x}^t \left(1 - \frac{1}{2}h(t')\right) dt' = \frac{2l_x}{c}, \quad (1.30)$$

where  $\tau_x$  represents the duration for the light to round-trip in the  $x$  arm and  $l_x$  denotes the length of the  $x$  arm. Therefore,

$$\tau_x = \frac{2l_x}{c} + \frac{1}{2} \int_{t-\tau_x}^t h(t') dt' \approx \frac{2l_x}{c} + \frac{1}{2} \int_{t-2l_x/c}^t h(t') dt'. \quad (1.31)$$

In the last expression,  $\tau_x$  is approximated by  $2l_x/c$  because  $h \ll 1$ . Therefore the net change in the optical phase is

$$\phi_x = \omega_0 \tau_x = \frac{2\omega_0 l_x}{c} + \frac{\omega_0}{2} \int_{t-2l_x/c}^t h(t') dt', \quad (1.32)$$

where  $\omega_0$  is the angular frequency of the laser field. In the right hand side of the equation, the first term denotes the static phase rotation due to the light traveling a length of  $2l_x$  while the second term denotes the phase deviation induced by the GW. Similarly, the light traveling along the  $y$  axis acquires the net phase rotation of

$$\phi_y = \frac{2\omega_0 l_y}{c} - \frac{\omega_0}{2} \int_{t-2l_y/c}^t h(t') dt', \quad (1.33)$$

with  $l_y$  the length of the  $y$  arm.

Therefore if the arm lengths are almost identical,  $l_x \approx l_y = l$ , the phase difference between that of  $x$  and  $y$  arm is

$$\phi_x - \phi_y = \frac{2\omega_0 (l_x - l_y)}{c} + \Delta\phi_g, \quad (1.34)$$

$$\Delta\phi_g \equiv \omega_0 \int_{t-2l/c}^t h(t') dt'. \quad (1.35)$$

Therefore GW changes the interference condition and hence it is observable as power fluctuation at the PD. When GW has a long wavelength such that the induced phase shift doesn't vary as fast as the round trip time of  $2l/c$ , it is approximated as,

$$\Delta\phi_g \approx \frac{2\omega_0 l}{c} h. \quad (1.36)$$

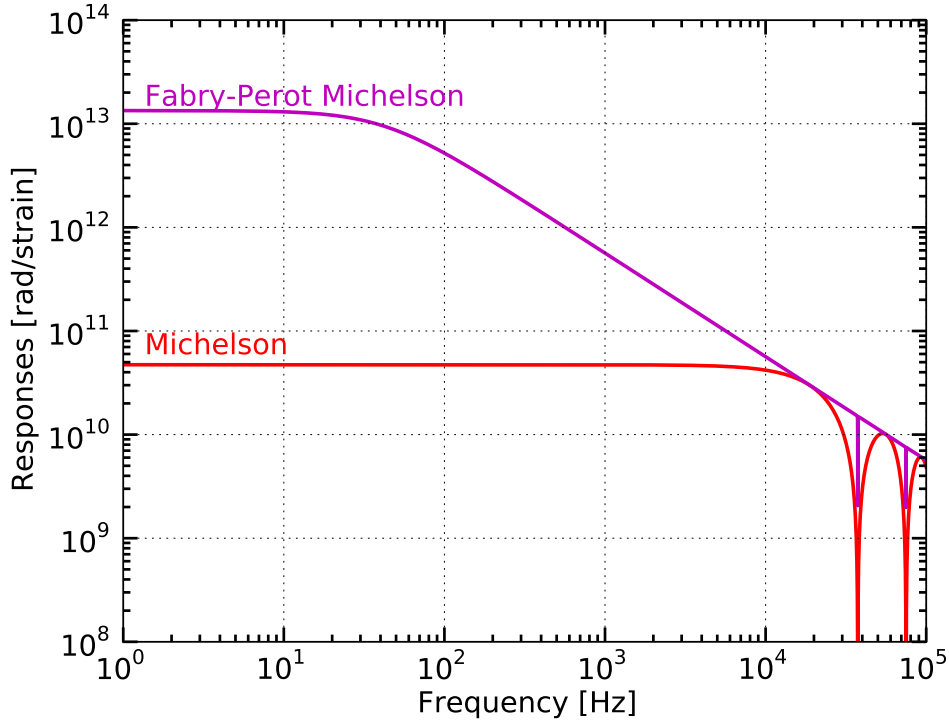


Figure 1.6: Frequency response of the Michelson and Fabry-Pérot Michelson interferometers. In both cases, the length of the arms are set to be 4 km. For the Fabry-Pérot Michelson configuration,  $t_1^2 = 0.014$  and  $t_2^2 = 50$  ppm are assumed.

### Frequency Response of the Michelson Interferometer

Consider that GW is monochromatic and at an angular frequency of  $\omega_g$ , so that

$$h(t) = h e^{i\omega_g t}. \quad (1.37)$$

Plugging this equation into equation (1.35), we find

$$H_{\text{MI}}(\omega_g, l) \equiv \frac{\Delta\phi_g}{h e^{i\omega_g t}} = \frac{2\omega_0}{\omega_g} \sin\left(\frac{\omega_g l}{c}\right) e^{-i\frac{\omega_g l}{c}} \quad (1.38)$$

This is the frequency response of a Michelson interferometer to GW [23, 24]. The response curve  $H_{\text{MI}}(\omega_g)$  is shown in figure 1.6 when the length of both

### 1.3. TERRESTRIAL LASER INTERFEROMETERS

---

arms is set to be at 4 km, which is the typical baseline length of the 2G interferometers. At low frequencies the response can be approximated as

$$H_{\text{MI}} \approx \frac{2\omega_0 l}{c}. \quad (1.39)$$

This is consistent with equation (1.36).

When the frequency of GW becomes higher than the inverse of the round trip time  $c/2l$ , the above approximation is not valid any more because the phase of the GW signal starts cancellation during the light trips in the arms. This effect appears as a cut off in the response curve in figure 1.6.

This effect leads to an issue because the bandwidth of the Michelson interferometer depends on the baseline length of the arms. If one desires to set the highest sensitivity at around 1 kHz and below, in which a neutronstar-neutronstar binary can be detected (see section 1.2.1), the length needs to be at  $l = 75$  km. Nevertheless this length is not practical. So for the reason a simple Michelson interferometer is not a realistic solution as a terrestrial detector.

#### 1.3.4 Enhancement by the Fabry-Pérot Arms

##### Overview

To increase the sensitivity with a given baseline length, embedding a Fabry-Pérot (FP) cavity in each arm of the Michelson interferometer is a solution. The optical configuration is shown in figure 1.7. Insertion of an FP cavity enables the laser field to bounce multiple times in the arm so that the interaction time of the light with GWs is elongated. From this point of view, it is said that the effective length is elongated.

The response of the FP Michelson interferometer can be calculated as follows. First of all we will consider just a single FP cavity without a Michelson interferometer as shown in figure 1.8 and then introduce a perturbation which is due to GW. Successively we derive the response of the single cavity. Later we will add the Michelson interferometer and the other FP cavity to the calculation.

##### Perturbation in a Single Fabry-Pérot Cavity

Here we consider a single FP cavity. In the static case (where no deviations in the length or the laser frequency), a set of the field equations can be written

## CHAPTER 1. BACKGROUND

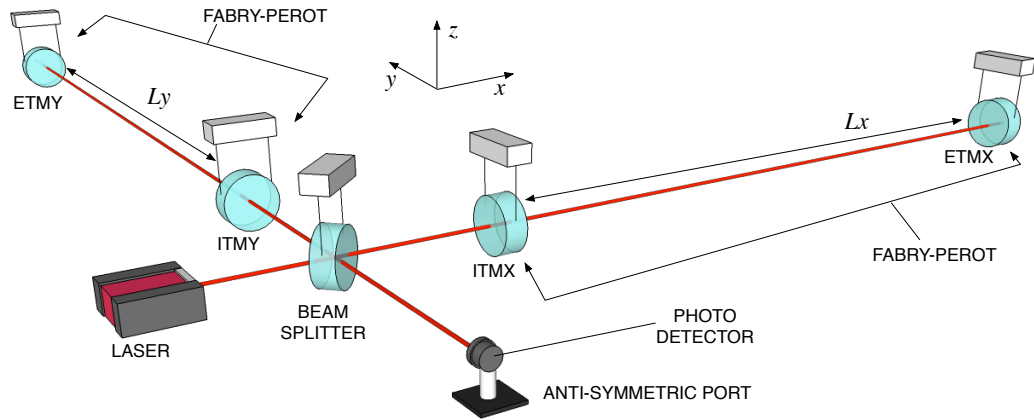


Figure 1.7: The Fabry-Pérot Michelson interferometer as a gravitational-wave detector. Each arm of the Michelson interferometer is replaced by a long FP cavity in order to increase the sensitivity.

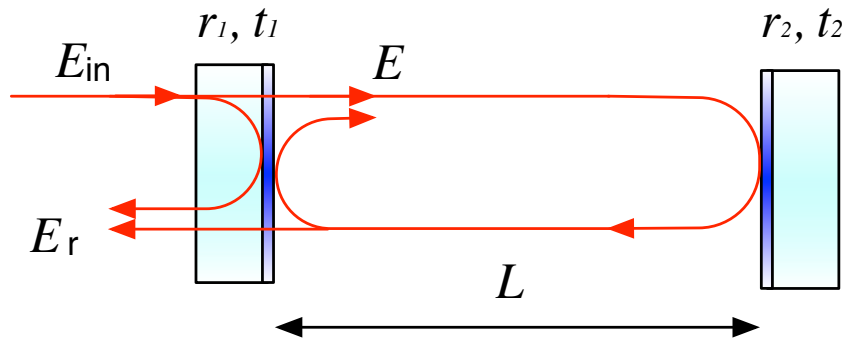


Figure 1.8: The Fabry-Pérot arm cavity formed by two mirrors.

### 1.3. TERRESTRIAL LASER INTERFEROMETERS

---

as,

$$E(t) = t_1 E_{\text{in}} + r_1 r_2 E(t - 2T) e^{-i\Delta\phi(t)}, \quad (1.40)$$

$$E_r(t) = -r_1 E_{\text{in}} + r_2 t_1 E(t - 2T) e^{-i\Delta\phi(t)}, \quad (1.41)$$

where  $E_{\text{in}}$ ,  $E$  and  $E_r$  denote the incident, intra-cavity and reflected fields respectively,  $r_j$  and  $t_j$  are the amplitude reflectivity and transmissivity of  $j$ -th mirror,  $L$  denotes the distance between two mirrors,  $T \equiv L/c$  is the one way trip time and  $\Delta\phi$  is the phase rotation. On the basis of equation (1.32) the phase shift can be redefined as,

$$\Delta\phi(t) = \frac{\omega_0}{2} \int_{t-\frac{2L}{c}}^t h(t') dt', \quad (1.42)$$

where we assumed that the static phase rotation satisfies  $2\omega_0 L/c = 2\pi n$  with  $n$  an integer — in fact this is the resonant condition of the FP cavity (see section 2.2.2). Therefore  $\Delta\phi$  is induced purely by GW in this case.

Suppose that  $\Delta\phi$  then induces a perturbation in the intra-cavity field. In this case the intra-cavity field can be redefined as,

$$E(t) = \bar{E} + \delta E(t), \quad (1.43)$$

where  $\bar{E}$  is the static solution and  $\delta E(t)$  denotes the deviation from the static solution. Then we assume that the phase rotation is so small that the phase term can be approximated by

$$e^{-i\Delta\phi} \approx 1 - i\Delta\phi. \quad (1.44)$$

Plugging last two equations into equation (1.40), we obtain

$$\bar{E} + \delta E(t) \approx -r_1 E_{\text{in}} + r_1 r_2 \bar{E} + r_1 r_2 \delta E(t - 2T) - i r_1 r_2 \bar{E} \Delta\phi, \quad (1.45)$$

where we neglected a higher order term, which contains the product of  $\Delta\phi$  and  $\delta E$ . Using the static solution expressed by

$$\bar{E} = t_1 E_{\text{in}} + r_1 r_2 \bar{E}, \quad (1.46)$$

we can remove the static terms from equation (1.45),

$$\delta E(t) = r_1 r_2 \delta E(t - 2T) - i r_1 r_2 \bar{E} \Delta\phi. \quad (1.47)$$

## CHAPTER 1. BACKGROUND

---

By applying the Laplace transform, the fluctuation in the intra-cavity field can be expressed by

$$\delta E(s) = -i \frac{r_1 r_2 \bar{E}}{1 - r_1 r_2 e^{-2sT}} \Delta\phi(s). \quad (1.48)$$

This is the deviation induced by the GW in the intra-cavity field. Using this result, we will derive the response of the Fabry-Pérot Michelson interferometer in the remaining subsections.

### Response of a Single Fabry-Pérot Cavity

As a first step we compute the perturbation in the reflected field using equation (1.48) because the reflected light carries the information of GWs in the FP Michelson interferometer.

Combining equations (1.40) and (1.41), we obtain

$$E_r(t) = \frac{t_1}{r_1} E(t) - \frac{t_1^2 + r_1^2}{r_1} E_{\text{in}} \quad (1.49)$$

If there are no perturbation where  $E_r \rightarrow \bar{E}_r = \text{constant}$  and  $E \rightarrow \bar{E} = \text{const}$ , the solution of the above equation should be

$$\bar{E}_r = \left( \frac{r_2 (r_1^2 + t_1^2) - r_1}{t_1} \right) \bar{E}. \quad (1.50)$$

Return to equation (1.49). A small deviation in the reflected field  $\delta E_r$  is related to the deviation in the intra-cavity field  $\delta E$  via,

$$\delta E_r(s) = \frac{t_1}{r_1} \delta E(s). \quad (1.51)$$

Using equation (1.48) and the last equation we can derive the resultant phase rotation in the reflected field,

$$\Delta\phi_r(s) \equiv \frac{\delta E_r(s)}{\bar{E}_r} = \frac{t_1^2 r_2}{(t_1^2 + r_1^2) r_2 - r_1} \frac{\Delta\phi(s)}{1 - r_1 r_2 e^{-2sT}}, \quad (1.52)$$

This indicates that the induced phase shift  $\Delta\phi$  is amplified by the frequency-dependent factor when it is observed at the reflected field.

### 1.3. TERRESTRIAL LASER INTERFEROMETERS

---

#### Response of the Fabry-Pérot Michelson Interferometer

Usually the arm lengths of the short Michelson interferometer (the one consisting of the BS and two mirrors nearby) is much shorter than the baseline of the arm FP cavity. Therefore it is reasonable to neglect the contribution from the Michelson interferometer. In this case the Michelson interferometer works only as a device which subtracts the optical phases between that from the  $x$  and  $y$  arms. This is merely a repeat of equation (1.34).

When GW, polarizing in the plus-mode, passes along the  $z$ -axis through the FP Michelson interferometer placed in the  $x$ - $y$  plane as shown in figure 1.7, the phase shift due to the GW in the  $x$  arm has a different sign from that of the  $y$  arm. Therefore the output field from the Michelson has a phase shift of  $2\Delta\phi_r$  if both arms have the same baseline length. As a result the frequency response of the FP Michelson interferometer is found to be

$$H_{\text{FPMI}}(\omega_g) \equiv \frac{2\Delta\phi_r(\omega_g)}{h(\omega_g)}, \quad (1.53)$$

$$= \frac{t_1^2 r_2}{(t_1^2 + r_1^2) r_2 - r_1} \frac{H_{\text{MI}}(\omega_g, L)}{1 - r_1 r_2 \exp(-2i\omega_g L/c)}, \quad (1.54)$$

where we used the fact  $\Delta\phi = H_{\text{MI}}h/2$ . Thus the addition of the FP cavities modifies the Michelson response  $H_{\text{MI}}$  and increases the sensitivity at low frequencies as shown in figure 1.6.

#### 1.3.5 Further Improvement with the Dual-Recycling

##### Introduction

Besides the arm FP cavities, the 2G interferometers will employ another scheme called the *Dual-Recycling*. The scheme enables one to further improve the sensitivity and optimize the observational bandwidth by the addition of two more mirrors to the FP Michelson interferometer or Michelson interferometer. The FP Michelson interferometer enhanced by the dual-recycling is referred to as dual-recycled Fabry-Pérot Michelson interferometer (DRF-PMI), the configuration of which is shown in figure 1.4.

The dual-recycling is a conjunction of two independent techniques — the *power recycling* and *signal recycling* techniques. The signal-recycling technique can be further divided into two modes — the *signal recycling* and *resonant sideband extraction* modes. In the rest of this section these techniques are briefly explained.

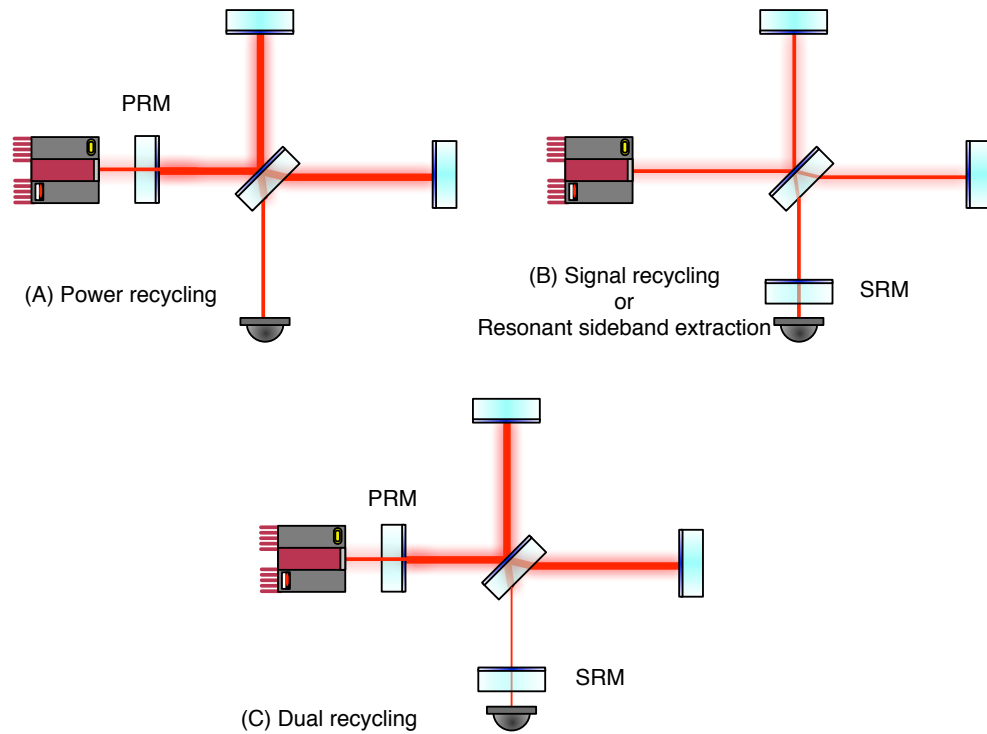


Figure 1.9: Configurations for the recyclings and resonant sidebands extraction schemes. (A) Power recycling scheme. (B) Signal recycling or resonant sideband extraction scheme. (C) Dual-recycling scheme.

### Power Recycling Scheme

The power recycling scheme utilizes an additional partial-reflector, called power recycling mirror (PRM) at the input side of the Michelson interferometer as shown in (A) of figure 1.9. The addition of the mirror enables one to reflect the light, which would otherwise leave the interferometer as a reflection, and propagate it back to the interferometer again. The idea of the power recycling scheme was invented in the early 90's [25] and it has been used in the 1G interferometers. The primary intention is to increase the amount of laser power illuminating the BS in order to reduce shot noise (see section 1.4.2).

### 1.3. TERRESTRIAL LASER INTERFEROMETERS

---

#### Signal Recycling Scheme

Similarly to the power recycling, the signal recycling enables us to recycle the the signal fields which are induced by GWs and propagate it back to the interferometer [26]. This technique requires an additional partial mirror, called signal recycling mirror (SRM) at the output side of the Michelson interferometer. (B) of figure 1.9 shows the configuration for the signal recycling. The SRM couples with the differential motion of two FP arm cavities (or the arms of a Michelson interferometer) such that the effective finesse for GW signals increases. As a consequence the storage time increases, resulting in a higher sensitivity at low frequencies. On the other hand it leads to a narrower observational bandwidth.

#### Resonant Sideband Extraction Scheme

The resonant sideband extraction scheme employs the same optical configuration as that for the signal recycling, but it decreases the effective finesse [27] instead of increasing it. Therefore it enables us to expand the observational bandwidth at the expense of the sensitivity at low frequencies. The configuration is shown in (B) of figure 1.9.

The signal recycling and resonant sideband extraction can essentially be switched to each other by just changing the interference condition without modifying the optical configuration.

#### Dual-Recycling Scheme

These recycling schemes, introduced above, are independent of each other — the power recycling increases the effective laser power while the signal recycling or resonant sideband extraction modifies the response of the FP arm cavities (or arms of the Michelson interferometer). Therefore the power recycling scheme can be independently introduced together with the signal recycling or resonant sideband extraction scheme. This particular combination is called the dual-recycling. The configuration is shown in (C) of figure 1.9. Note that the quantum-noise-limited sensitivity of the DRFPMI have been studied [28, 29].

## CHAPTER 1. BACKGROUND

---

Project	Baseline	Configuration	Place
LIGO	4 km	DRFPMI	Livingston/Hanford USA
KAGRA	3 km	DRFPMI	Gifu JAPAN
VIRGO	3 km	DRFPMI	Pisa ITALY
GEO	600 m	DRMI	Hannover GERMANY
ET	10 km	DRFPMI	under discussion

Table 1.1: Summary of the interferometers that will form the worldwide detector network. DRMI stands for dual-recycled Michelson interferometer. ET stands for Einstein Telescope.

### 1.3.6 Worldwide Detector Network

In order to fully open GW astronomy, a worldwide detector network is necessary. Distributing the interferometers over the world — called worldwide detector network — allows us to perform a triangulation to locate a GW event on the sky. Therefore it is important to build a number of the GW interferometers over the world. In this section the interferometers, which form the network, and a future interferometer are introduced. Additionally table 1.1 summarizes the interferometers.

#### LIGO

LIGO or Laser Interferometer Gravitational-wave Observatory [9] is a US project. The project owns two observatories; one in the desert of Hanford in Washington and the other in the forest at Livingston in Louisiana. Each observatory has a 4-km baseline interferometer and currently they are being upgraded to so-called advanced LIGO (aLIGO) in order to further increase the sensitivity. The aLIGO interferometers are expected to be online in 2014 as a 2G interferometer. Before the upgrade started, LIGO had been running for approximately 8 years, and they successfully achieved the design sensitivities and conducted remarkable science runs.

#### KAGRA

KAGRA, also known as LCGT or Large Cryogenic Gravitational-wave Telescope, is a Japanese 2G interferometer project [10]. Perhaps KAGRA can

### 1.3. TERRESTRIAL LASER INTERFEROMETERS

---

be considered as a 2.5 generation interferometer because two futuristic keys will be employed. The first key is cryogenic mirrors — the mirrors are cooled down to decrease thermal noises associated with the mirrors and their suspensions. The other key is underground — the interferometer will be built in the Kamioka mine under the Kamioka mountain in Gifu prefecture in order to take advantage of the quiet environment. The baseline length is designed to be 3 km. Currently the tunnel is being excavated and a first test run will take place by 2016.

#### **VIRGO**

VIRGO is a project led by French and Italian groups [8]. The interferometer is placed at Pisa in Italy and the baseline length is 3 km. Similarly to aLIGO, the facilities and interferometer are currently being upgraded to be a 2G interferometer, called advanced VIRGO. In the past years, VIRGO conducted several science runs and have performed coincidence GW searches with LIGO. One of the greatest feature in the interferometer is that the vibration isolation system is sophisticated and in fact the low frequency sensitivity was better than that of LIGO despite of the shorter baseline length.

#### **GEO**

GEO is a project led by German and UK groups [7]. The baseline length is 600 m. Unlike the other interferometers listed above, GEO employs the delay-line arms, where the laser path is folded by mirrors, resulting in an effective arm length of 1200 m. A remarkable success in GEO is that they have succeeded in a stable operation of the interferometer with the quantum squeezing technique, surpassing the standard quantum noise limit [30].

#### **Einstein Telescope**

Einstein telescope is a European 3rd generation project [31] and is to be hoped to serve as a “telescope” in the sense it will frequently detect GW signals like the standard electro-magnetic wave telescopes. A number of cutting-edge technologies will be applied to the interferometer such as, cooling of test masses, non-Gaussian laser beam, sophisticated vibration isolation systems, and so forth. Intensive studies have been conducted to design the optical configurations and facilities in the past several years. Einstein telescope will be online in 2020’s.

### 1.4 Length Sensing and Control of the Interferometer

---

#### 1.4.1 Introduction

Length sensing and control (LSC) of the laser interferometric detector is essential in order to maintain the design sensitivity. Since the interferometric condition is generally a function of the optical lengths and laser frequency, they must always satisfy a particular condition. However in reality the mirror positions are always excited by seismic noise and also the laser frequency itself fluctuates from the nominal value, resulting in destruction of the interferometric condition. So for the reason, it is almost impossible to robustly maintain the interferometric condition without active controls for the lengths (and also the laser frequency).

Besides seismic and laser frequency noises, there are some other noises which hinder the precision control. With active control, the optical lengths need to be precisely controlled such that the interferometric condition is maintained. However the use of the active control can impose some noises. Various noise sources relevant to the precision control are listed below.

#### 1.4.2 Various Noise Sources

##### Seismic Noise

Seismic noise is one of the biggest noise sources. It displaces the position of the mirrors, resulting in variation in the optical lengths. Although the mirrors are suspended by wires to reduce seismic noise, there still remains non-negligible amount of the vibration. Seismic noise leads to an issue — it fluctuates the length of optical cavities by an amount of more than their resonance linewidth at low frequencies. As a consequence the optical cavities can not be at rest exactly on the operating point without active controls. For instance, typical seismic noise expected in the 2G interferometer is an order of 100 nm, which is already large enough to pop the FP arm cavities out of their full linewidth of about 1 nm.

## 1.4. LENGTH SENSING AND CONTROL OF THE INTERFEROMETER

---

### Laser Noises

A free running laser generally exhibits fluctuation in both the amplitude and frequency (or phase) of its field. Since any photo detection measurement involves an intensity measurement of the laser, the amplitude noise can couple with the resultant photo current in various ways. Therefore the amplitude noise can introduce errors via photo detection. On the other hand the frequency noise directly poses an issue in LSC because the frequency determines the interferometric condition of the interferometer. Therefore the frequency noise must be suppressed (or the optical lengths must be corrected as compensation) with active control. Typically a free running Nd:YAG NPRO (non planar ring oscillator) shows frequency noise with spectrum approximated by a power law as,

$$\Delta\nu \sim 1 \times 10^3 \left( \frac{1 \text{ Hz}}{f} \right) \text{ Hz}/\sqrt{\text{Hz}}. \quad (1.55)$$

### Quantum Shot Noise

Quantum shot noise or simply shot noise is fundamental and hence inevitable noise because of the nature of quantum mechanics. This limits the precision of measurements. In a classical view, shot noise was understood as photon counting error at a PD [24]. In a modern picture [32, 33], it can be considered as a consequence of the vacuum fluctuations in the electric magnetic field, which enters the interferometer from any open ports. It results in white noise and its level can be improved by increasing the laser power because it is in proportion to the inverse of the square root of the laser power.

### Radiation Pressure Noise

Similarly to shot noise, fluctuations in numbers of photons then fluctuates the momentum of the suspended mirrors through the radiation pressure. This phenomenon is also well explained by the vacuum fluctuation model. In the 1G interferometers, the radiation pressure noise were not a dominant noise source as the seismic noise were prominent, but it can potentially be a dominant noise source in the future interferometer. Shot noise and radiation pressure noise have been analytically studied in references [28, 29].

## CHAPTER 1. BACKGROUND

---

### Thermal Noises

The mirrors and their suspension systems of an interferometer fluctuate thermally because they are at a finite temperature. These thermal fluctuations induce undesired variations in the optical lengths of the interferometer, called *thermal noise*. When the suspension has a finite temperature, it excites the mechanical mode of the suspension, resulting in a displacement of the mirror hung from the suspension [34]. With the same argument the mirror itself exhibits the thermally induced fluctuation. Nowadays they are further categorized into two kinds: Brownian noise [35] and thermo-optic noise [36].

### Control Noises

When an active control is applied to the length of an optical cavity, it potentially wobbles the optical length unnecessarily. This is because that the active control can introduce some technical noises, such as electronics noises, sensor noises and so forth. Eventually they are fed back to the length. In order to reduce control noises the design of the active control systems needs to be proceeded with care. Since the GW interferometer usually employs more than 100 of the active controls, a modeling of the interferometric control system is necessary in order to systematically identify and reduce the control noises.

### 1.4.3 Null Measurement due to the Length Control

With the active control on the optical lengths, the detection method of GW becomes a particular type known as the *null measurement* [24]. When GW passes through the interferometer it changes the optical phase of the laser as explained in section 1.3.3. However, since the phase shift is equivalent to a displacement in the optical length, the active control will suppress the phase shift by correcting the length. This doesn't mean that the active control diminish the GW signal because the signal can be reconstructed from the information of the amount of the length correction. Therefore the active control doesn't diminish GW signals, but forces the detection to be null measurement.

## 1.5 Summary of the Chapter

---

- Gravitational-wave was predicted on the basis of the general theory of relativity, but it has not been directly observed yet.
- The first detection of gravitational-wave will open a new window to the Universe, called gravitational-wave astronomy.
- There are a number of possible astrophysical gravitational-wave sources, which can be detected by the terrestrial laser interferometric detectors.
- The 2nd generation interferometric gravitational-wave detectors are recently upgraded or newly constructed over the world in order to further increase the sensitivity. These interferometers are to be hoped to make the first detection.
- The 2nd generation interferometer is a variant of the Michelson interferometer enhanced by the addition of a number of optical cavities.
- The laser interferometer needs active length control against seismic noise and some other various noises in order to maintain the desired interferometric state.



# 2

## Basics in Laser Interferometry

This chapter describes a set of basics necessary to understand laser interferometry. In this chapter three main topics are introduced — the interferometric devices in sections 2.1 and 2.2, a technique to readout the lengths of the interferometric devices in sections 2.3, 2.4 and 2.5, and the second-harmonic generation in section 2.6.

### 2.1 Michelson Interferometer

---

The Michelson interferometer can be considered as an optical phase detector, while it is broadly used as a Fourier transform spectrometer in astronomical telescopes [37].

Consider a Michelson interferometer as shown in figure 1.5. The incident field  $E_{\text{in}}$  illuminating the beam splitter (BS) can be written as,

$$E_{\text{in}} = A_0 e^{i\omega_0 t}, \quad (2.1)$$

where  $A_0$  is the amplitude and  $\omega_0$  is the angular frequency of the laser field. At any arbitrary time  $t$ , the output field exiting from the BS to the Anti-Symmetric (AS) port is expressed by

$$E_{\text{AS}} = -t_{\text{BS}} r_{\text{BS}} r A_0 e^{i(\omega_0 t - \phi_x)} + t_{\text{BS}} r_{\text{BS}} r A_0 e^{i(\omega_0 t - \phi_y)}, \quad (2.2)$$

where  $t_{\text{BS}}$  and  $r_{\text{BS}}$  denote respectively the amplitude reflectivity and transmissivity of the BS,  $r$  denotes the amplitude reflectivity of the end mirrors and  $\phi_x$  and  $\phi_y$  are the phase shift due to the light traveling in the  $x$  and  $y$  arms respectively. After some algebra one can rewrite the last equation as,

$$E_{\text{AS}} = 2it_{\text{BS}} r_{\text{BS}} r A_0 e^{i(\omega_0 t - (\phi_x + \phi_y)/2)} \sin\left(\frac{\phi_x - \phi_y}{2}\right). \quad (2.3)$$

## CHAPTER 2. BASICS IN LASER INTERFEROMETRY

---

Similarly, the field reflected back toward the laser source can be written as

$$E_{\text{REFL}} = 2t_{\text{BS}}r_{\text{BS}}rA_0e^{i(\omega_0t - (\phi_x + \phi_y)/2)} \cos\left(\frac{\phi_x - \phi_y}{2}\right). \quad (2.4)$$

Therefore the output fields can be dealt as a single field. We find that the phase of the field rotates by the averaged phase shift of  $(\phi_x + \phi_y)/2$ , while the amplitude is a function of the difference between two phases  $\phi_x - \phi_y$ . The power can be obtained by squaring the last two equations,

$$P_{\text{AS}} = 2(r_{\text{BS}}t_{\text{BS}}rA_0)^2 [1 - \cos(\phi_x - \phi_y)], \quad (2.5)$$

$$P_{\text{REFL}} = 2(r_{\text{BS}}t_{\text{BS}}rA_0)^2 [1 + \cos(\phi_x - \phi_y)]. \quad (2.6)$$

So that the photo current from a photo detector (PD) is a function of the phase difference  $\phi_x - \phi_y$ . Therefore the Michelson interferometer is sensitive to the optical phase and hence able to detect GWs.

## 2.2 Optical Cavities

---

### 2.2.1 Overview

The optical cavity or equivalently Fabry-Pérot (FP) cavity is a device formed by two or more partial reflectors to store photons (or to reject them) in the cavity. In particular, those formed by two mirrors facing each other is known as the FP cavity, as depicted in figure 2.1. Note that the dual-recycling (see section 1.3.5) introduces two optical cavities formed by four mirrors and therefore they are also a type of the optical cavity.

In this section we consider only the FP cavity because the fundamental properties can be applied to those formed by three or more mirrors. As a first step the static response is introduced in section 2.2.2 and then the characteristic quantities are introduced in section 2.2.3. Finally the dynamical response, which is indispensable when controlling the cavities, is discussed in section 2.2.4.

### 2.2.2 Static Responses

When the cavity is under the static condition, where there are no rapid variations either in the fields or the cavity length, a set of the fields associated

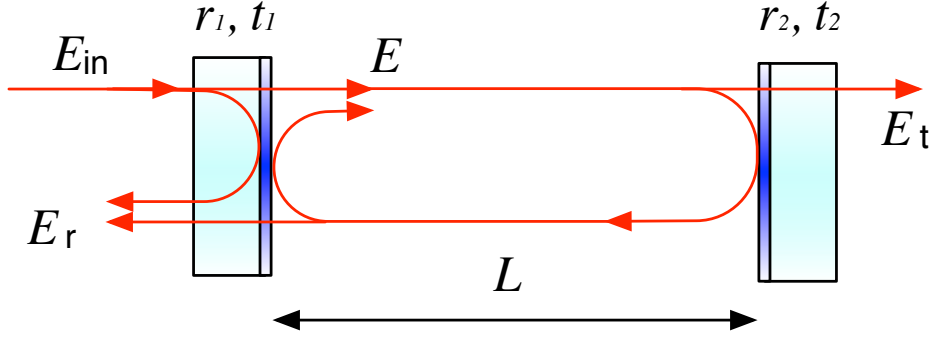


Figure 2.1: Schematic view of the Fabry-Pérot cavity.

with the cavity can be simply expressed by

$$E = t_1 E_{\text{in}} + r_1 r_2 E e^{-2ikL}, \quad (2.7)$$

$$E_r = -r_1 E_{\text{in}} + \frac{t_1}{r_1} (E - t_1 E_{\text{in}}), \quad (2.8)$$

$$E_t = t_2 E, \quad (2.9)$$

where  $E_{\text{in}}$ ,  $E$ ,  $E_r$  and  $E_t$  are the incident, intra-cavity, reflected and transmitted fields respectively,  $r_j$  and  $t_j$  are the amplitude reflectivity and transmissivity of  $j$ -th mirrors ( $j = 1, 2$ ), and  $k$  and  $L$  are the wave number and baseline length respectively. A schematic of the FP cavity is illustrated in figure 2.1. From equation (2.7), one can obtain the intra-cavity field,

$$E = \frac{t_1}{1 - r_1 r_2 e^{-2ikL}} E_{\text{in}}. \quad (2.10)$$

The intra-cavity power  $P_{\text{FP}}$ , which represents the amount of the laser power stored in the cavity, can be defined by

$$P_{\text{FP}} \equiv |E|^2 = \frac{t_1^2}{|1 - r_1 r_2 e^{-2ikL}|^2} |E_{\text{in}}|^2 \quad (2.11)$$

The intra-cavity power is shown in figure 2.2 as a function of the displacement in  $L$ . The resonance condition of the FP cavity depends on the round trip phase, defined by

$$\phi_{\text{rt}} \equiv 2kL = \frac{4\pi L}{\lambda}, \quad (2.12)$$

## CHAPTER 2. BASICS IN LASER INTERFEROMETRY

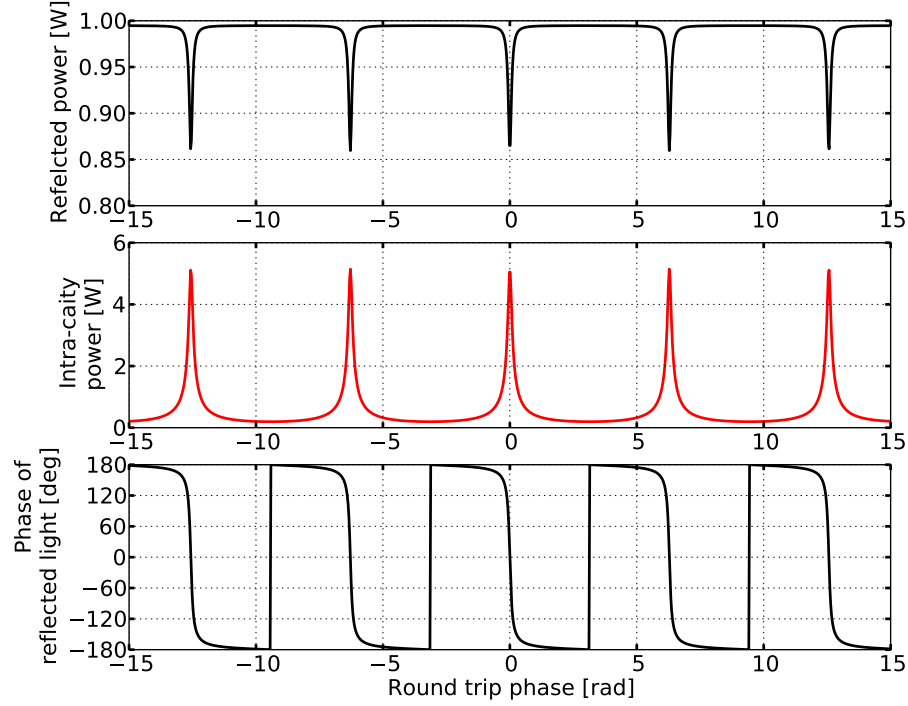


Figure 2.2: Static response of an FP cavity, calculated. (Upper plot) Power of the reflected light (Middle plot) intra-cavity power (Lower plot) the phase rotation in the reflected field. An incident laser of 1 W, transmissivities of  $t_1^2 = 0.014$ , and  $t_2^2 = 50$  ppm are assumed.

with  $\lambda$  the laser wavelength. The FP cavity is on resonance when the round trip phase satisfies the following condition,

$$\phi_{\text{rtp}} = 2\pi n \quad (n = 0, \pm 1, \pm 2, \dots). \quad (2.13)$$

When the cavity is on resonance, the intra-cavity power reaches the maximum because the incident field constructively interferes with the intra-cavity field and consequently the intra-cavity power builds up.

Plugging equation (2.7) to equation (2.8), one can define the reflectivity of the cavity as,

$$r_{\text{FP}} \equiv \frac{E_r}{E_{\text{in}}} = -r_1 + \frac{r_2 t_1^2 e^{-2ikL}}{1 - r_1 r_2 e^{-2ikL}}. \quad (2.14)$$

As shown in the above equation, the reflected field is made of the prompt reflection appearing as the first term, and the leakage field from the cavity, appearing as the second term. Figure 2.2 shows also the reflected power and its phase. As it is shown, the phase dramatically rotates when the cavity is in the vicinity of a resonance. This rapid rotation of the phase corresponds to the phase enhancement explained in section 1.3.4.

### 2.2.3 Characteristic Quantities

In this section we briefly summarize a number of important physical quantities that characterize an FP cavity. For more details of the derivations, see for instance reference [38].

#### Free Spectral Range

Free Spectral Range (FSR) is a measure of the separation between the neighboring resonances in terms of the laser frequency. It is defined by,

$$f_{\text{FSR}} = \frac{c}{2L}. \quad (2.15)$$

#### Finesse and Linewidth

The finesse  $\mathcal{F}$  represents the sharpness of the resonances. It can be approximated by the following form,

$$\mathcal{F} = \frac{\pi\sqrt{r_1 r_2}}{1 - r_1 r_2}. \quad (2.16)$$

Once the finesse is determined one can compute the corresponding linewidth in terms of the full width at half maximum (FWHM),

$$\nu_{\text{FWHM}} = \frac{f_{\text{FSR}}}{\mathcal{F}}, \quad (2.17)$$

$$L_{\text{FWHM}} = \frac{\lambda}{2\mathcal{F}}, \quad (2.18)$$

where  $\nu_{\text{FWHM}}$  denotes the linewidth with respect to the laser frequency while  $L_{\text{FWHM}}$  is that with respect to the displacement in the baseline length.

## CHAPTER 2. BASICS IN LASER INTERFEROMETRY

---

### Storage Time and Cavity Pole

The storage time  $\tau_s$  represents the mean duration for a photon to stay in the cavity. It is expressed by

$$\tau_s = \frac{2L}{c} \frac{1}{\ln(r_1 r_2)} \approx \frac{2L}{\pi c} \mathcal{F}, \quad (2.19)$$

The last approximation is valid as long as  $r_1 r_2 \sim 1$ .

The cavity pole  $f_c$  denotes the frequency above of which an induced variation in the intra-cavity field cancels. The cavity pole essentially originates from the fact that a cavity has a finite storage time. It is related with the storage time in the following form,

$$f_c = \frac{1}{2\pi\tau_s}. \quad (2.20)$$

### 2.2.4 Dynamical Responses

In most of applications of the optical cavity in the gravitational-wave (GW) interferometer, the dynamical responses must be considered. Since the optical cavities can be a part of the active control loops, it is necessary to consider the dynamical responses (or equivalently frequency responses).

In this section two specific dynamical responses are discussed — a response with respect to fluctuation in the laser frequency and a response with respect to fluctuation in the baseline length. For both of them we start from applying a perturbation and then derive the corresponding transfer functions by approximating the system as linear.

#### Response to Laser Frequency

Consider the case where the phase of the incident field varies as a function of time. In this case the incident field can be expressed by,

$$E_{\text{in}}(t) = A e^{i\Psi(t)}, \quad (2.21)$$

where  $A$  is a constant, representing the amplitude of the incident field, and  $\Psi(t)$  is fluctuation in the phase. In this case the intra-cavity field (1.40) can be rewritten as

$$E(t) = t_1 A e^{i\Psi(t)} + r_1 r_2 E(t - 2T). \quad (2.22)$$

## 2.2. OPTICAL CAVITIES

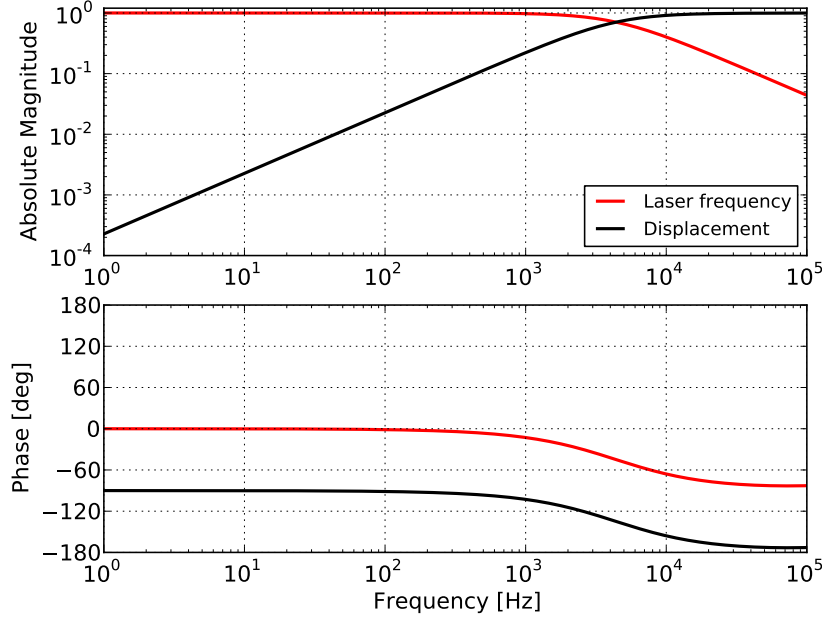


Figure 2.3: Bode plot of the dynamical responses. (Red) Transfer function from the laser frequency to that of the intra-cavity field. (Black) The transfer function from the length displacement in terms of the laser frequency to the frequency of the intra-cavity field. In the calculation  $\lambda = 1064$  nm,  $L = 40$  m,  $t_1^2 = 0.014$ , and  $t_2^2 = 50$  ppm are assumed.

where  $T$  is the one-way trip time defined by  $T \equiv L/c$  and we assumed that the resonant condition (2.13) is satisfied. If the phase fluctuation  $\Psi$  is small, we can approximate the phase term by

$$e^{i\Psi(t)} \approx 1 + i\Psi(t). \quad (2.23)$$

Since the phase term is now off from the nominal value of 1, we expect that the solution of equation (2.22) can be in a similar form of

$$E(t) = \bar{E} + \delta E(t), \quad (2.24)$$

where  $\bar{E}$  is the static solution and  $\delta E(t)$  is the perturbed field. Using the last two expressions one can rewrite equation (2.22) as,

$$\delta E(t) = it_1 A \Psi(t) + r_1 r_2 \delta E(t - 2T), \quad (2.25)$$

## CHAPTER 2. BASICS IN LASER INTERFEROMETRY

---

where we used the static solution of  $\bar{E} = t_1 A + r_1 r_2 \bar{E}$ . Applying the Laplace transform, one can obtain

$$\delta E(s) = i \frac{t_1 A}{1 - r_1 r_2 e^{-2sT}} \Psi(s). \quad (2.26)$$

Therefore the phase rotation induced by the deviation of the laser frequency is

$$\Delta\phi(s) \equiv -i \frac{\delta E(s)}{\bar{E}} = \frac{1 - r_1 r_2}{1 - r_1 r_2 e^{-2sT}} \Psi(s). \quad (2.27)$$

Applying  $-is/2\pi$  on both sides of the equation, we obtain a transfer function of

$$C(s) = \frac{\Delta\nu}{\Delta\nu_{\text{laser}}} = \frac{1 - r_1 r_2}{1 - r_1 r_2 e^{-2sT}}, \quad (2.28)$$

where  $\Delta\nu \equiv -i(s/2\pi)\Delta\phi$  is the induced frequency fluctuation of the intra-cavity field, and  $\Delta\nu_{\text{laser}} \equiv -i(s/2\pi)\Psi$  is the frequency fluctuation in the incident laser field. This is the transfer function from the laser frequency deviation to the frequency of the intra-cavity field. The bode plot of this transfer function is shown in figure 2.3 as a function of the frequency. As shown in the figure  $C(s)$  is flat below the cavity pole  $f_c$  and starts rolling off above it. Hence  $C(s)$  can be approximated by

$$C(f) \approx \frac{1}{1 + if/f_c}, \quad (2.29)$$

where we used  $s = 2i\pi f$ .

### Response to Displacement

Suppose that the baseline length is displaced by  $\xi$  from the nominal length of  $L$  which meets the resonance condition (2.13). The corresponding change in the optical phase can be expressed by  $2k\xi(t)$ . From equation (1.48) we can obtain

$$\Delta\phi(s) \equiv -i \frac{\delta E(s)}{\bar{E}} = -2k \frac{r_1 r_2}{1 - r_1 r_2 e^{-2sT}} \xi(s), \quad (2.30)$$

where  $\Delta\phi$  is the induced phase shift in the intra-cavity field. Converting equation (2.30) into the frequency of the field by multiplying both sides by a factor of  $-is/2\pi$ , we can obtain

$$H_x(s) \equiv \frac{\Delta\nu}{\xi(s)} = i \frac{k}{\pi} \frac{r_1 r_2 s}{1 - r_1 r_2 e^{-2sT}}, \quad (2.31)$$

## 2.2. OPTICAL CAVITIES

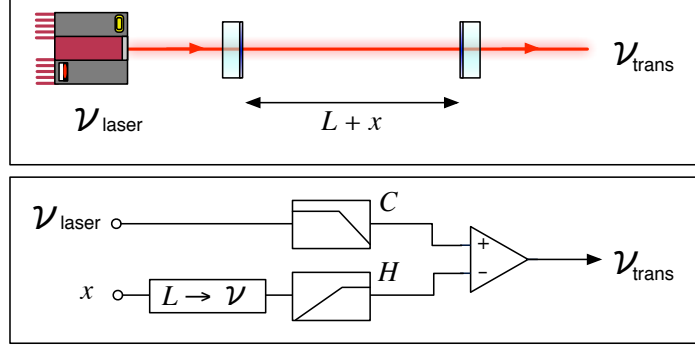


Figure 2.4: (Upper) A schematic of an FP cavity illuminated by a laser. (Lower) The equivalent diagram of the noise transfer in the FP cavity. The “ $L \rightarrow \nu$ ” block denotes the conversion coefficient defined by  $\nu/L$ . The block labeled “C” represents the low-pass filter (2.29) and the one labeled “B” represents the high-pass filter (2.34) with its sign flipped.

where  $\Delta\nu \equiv -i(s/2\pi)\Delta\phi$  is the resultant frequency fluctuation in the intra-cavity field. This is the transfer function from the displacement to the frequency of the intra-cavity field. For a practical use, it is useful to treat the displacement as a frequency variation in the eigen frequency of the cavity. The eigen frequency of the cavity and displacement is connected via

$$-\frac{\delta\nu}{f_{\text{FSR}}} = \frac{\xi}{\lambda/2}. \quad (2.32)$$

Using this relation, one can obtain another form of the transfer function,

$$H_\nu(s) = -2sT \frac{r_1 r_2}{1 - r_1 r_2 e^{-2sT}}. \quad (2.33)$$

Figure 2.3 shows the transfer function  $H_\nu$ . As shown in the figure the transfer function is a high-pass filter and it becomes flat above the cavity pole. For most of modeling works, it can be approximated by

$$H_\nu(f) = -\frac{if/f_c}{1 + if/f_c}. \quad (2.34)$$

This is valid as long as  $r_1 r_2 \sim 1$  and the frequency of interest is far below the FSR.

## CHAPTER 2. BASICS IN LASER INTERFEROMETRY

---

This transfer function can be intuitively understood as follows. Displacement in the length causes a phase modulation in the intra-cavity field. Due to the cavity pole effect, the phase is low-passed above the cavity pole frequency. Therefore the transfer function can be a form of  $1/(1 + if/f_c)$  at this point. Then converting the phase into the frequency introduces another  $s$ , resulting in the form shown in the last equation.

Combining these two filtering effects, one can construct a linear model for the frequency of the transmitted light as shown in figure 2.4.

## 2.3 Frontal Modulation Scheme for Length Sensing

---

### 2.3.1 Introduction

The frontal modulation scheme enables us to extract the length information by phase-modulating the incident laser field and by synchronously demodulating the observed powers. The scheme was invented in 1983 [39] and was meant to readout the length of a single FP cavity (or the laser frequency). Today it has been extended to a Michelson interferometer and even multiply-coupled optical cavities, such as the GW interferometer. In this thesis, when the scheme is applied to a single optical cavity such as an FP cavity, it is specifically called Pound-Drever-Hall (PDH) technique. For more detailed derivations and discussions, reference [40] can be useful as it gives a comprehensive view of the length sensing.

The frontal modulation scheme can be considered as a *Heterodyne* detection analogously to that in the radio communication fields. In the scheme, there are three key processes — the phase modulation, optical heterodyne and electrical demodulation. With the last two processes the frequency of signals are down-converted from several 100 THz (which is the laser frequency) to DC so that the signal can be used for the active length control.

This section introduces the frontal modulation scheme and its mathematical treatment, starting from a primitive picture in section 2.3.2. To further understand the phase modulation, the *sideband picture* is introduced in section 2.3.3. Then the photo detection and electrical demodulation are explained in section 2.3.4. Two practical applications are discussed in detail in section 2.4.

## 2.3. FRONTAL MODULATION SCHEME FOR LENGTH SENSING

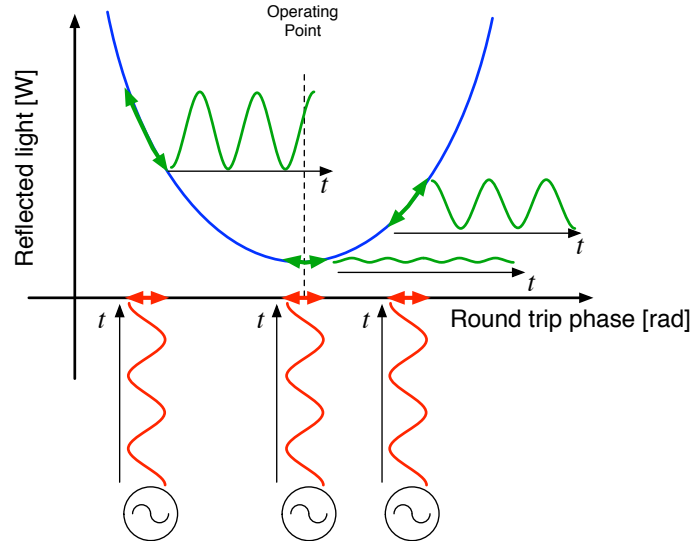


Figure 2.5: Primitive picture of the frontal modulation scheme. The reflected light from an FP cavity is also modulated when the phase is modulated. (Blue trace) the reflected light from the FP cavity as a function of the round trip phase. The trace is quadratic around the operating point and therefore one can not reproduce the length information from this. (Red) The applied phase modulations. It results in an intensity modulation at the same frequency. (Green) Resultant intensity modulations due to the phase modulations.

### 2.3.2 A Primitive Picture

Suppose that, for instance, an FP cavity is illuminated by a laser. As explained in section 2.2.2, both the transmitted and reflected field is a function of the baseline length or equivalently the optical phase. In principle it is possible to extract the length information from the raw power of the reflected or transmitted light by photo detection.

An issue is that the reflected or transmitted light exhibits a quadratic trace around the operating point (e.g. the resonance point) in most of cases. The blue curve in figure 2.5 illustrates the situation when the reflected power is observed. This is problematic since the signal is not linear and hence one can not reproduce the length information from it. Note that one can still use the raw power signals if the FP cavity needs to be slightly off from a resonance at which the raw power signal can be approximated as a linear

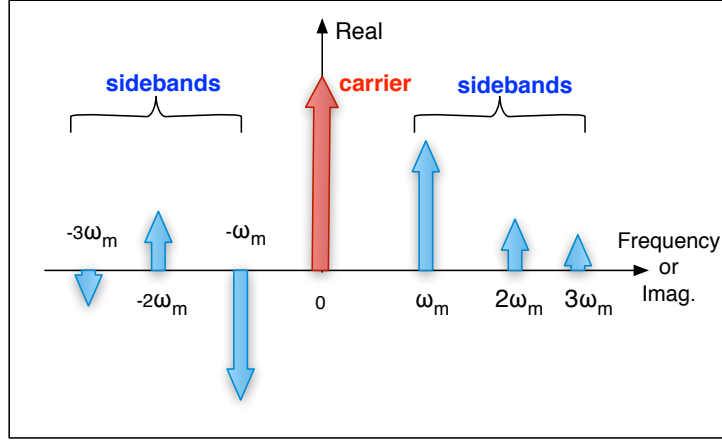


Figure 2.6: Phase-modulated field in the sideband picture. The  $x$ -axis is frequency of the field and also imaginary part of each field. The  $y$ -axis is the real part of the amplitude of each field.

signal.

To avoid the issue, the idea is to modulate either the optical phase or length at a certain frequency such that the resultant power gets modulated at the same frequency as shown in figure 2.5. If such an intensity-modulated power is observed, one can obtain essentially the derivative of the trace, which is linear, by synchronously demodulating the intensity-modulated power. This is the idea of the frontal modulation scheme.

### 2.3.3 The Sideband Picture

If a laser field of  $\omega_0$  is phase-modulated at  $\omega_m$ , it can be expressed by,

$$E = E_0 \exp [i (\omega_0 t + \Gamma \sin \omega_m t)], \quad (2.35)$$

where  $\Gamma$  represents the amount of the phase modulation, called modulation depth or modulation index. The modulation frequency  $\omega_m$  is typically chosen to be at Radio Frequencies (RFs) where laser noises are generally small. Expanding the last equation by using the Jacobi-Anger expansion, one can

## 2.3. FRONTAL MODULATION SCHEME FOR LENGTH SENSING

obtain,

$$E = E_0 e^{i\omega_0 t} \sum_{k=-\infty}^{\infty} J_k(\Gamma) e^{ik\omega_m t}, \quad (2.36)$$

where  $J_k(\Gamma)$  is the Bessel function of the first kind which is now a function of an integer  $k$  and the modulation depth  $\Gamma$ .

It is clear that a monochromatic phase modulation splits the incident field into multiple components. The field with  $k = 0$  is called the *carrier* and oscillates at  $\omega_0$ . On the other hand the fields with  $k \neq 0$  are called the *sidebands* and oscillate at  $\omega_0 + k\omega_m$ . In order to visualize the carrier and sidebands, usually the summed terms in equation (2.36) are concerned and it is referred to as *phasor*. The phasor for a monochromatically phase-modulated field is depicted in figure 2.6.

The carrier has the biggest amplitude and the sidebands have smaller amplitude if  $\Gamma \ll 1$ . As the absolute magnitude of  $k$  increases from zero, the Bessel function  $J_k$  gets smaller because it can be approximated by

$$J_k(\Gamma) \approx \frac{1}{k!} \left(\frac{\Gamma}{2}\right)^k. \quad (2.37)$$

Therefore the amplitude of the sidebands decreases as  $k$  runs away from zero.

### 2.3.4 Photo Detection and Demodulation

The phase-modulated laser gets affected by an interferometer via reflection or transmission — the phase of the carrier and sidebands rotate and also their amplitude are affected. After the photo detection and subsequent electrical demodulation of the photo current, it yields a linear signal with respect to the optical length (as well as the laser frequency).

#### Photo Detection (Squared Detection)

When the light exits off from the interferometer, the field going toward a photo detector (PD)  $E_{\text{PD}}$  can be expressed in the following general form:

$$E_{\text{PD}} = E_0 e^{i\omega_0 t} \sum_k x_k E_k, \quad (2.38)$$

$$x_k \equiv x(k\omega_m), \quad (2.39)$$

$$E_k \equiv J_k(\Gamma) e^{ik\omega_m t}, \quad (2.40)$$

## CHAPTER 2. BASICS IN LASER INTERFEROMETRY

---

where  $x_k$  denotes the response of the interferometer at  $k\omega_m$  and is usually a complex number, and  $E_k$  is  $k$ -th harmonic sideband or the carrier field for  $k = 0$ . When the field hits the PD it results in a photo current of

$$i_{\text{PD}} = \eta |E_{\text{PD}}|^2, \quad (2.41)$$

where  $\eta$  is the responsivity of the photo diode.

Because the photo detection is a *squared detection*, it produces the cross terms that are the products between each sideband and carrier. This is a key for extraction of the length signal. In this process, the information that the laser oscillates at  $\sim 100$  THz is lost, but however the phase information survives owing to the squared detection.

The length information (or equivalently the phase information) is encoded in the photo current oscillating at  $n\omega_m$  with  $n$  an integer. The resultant photo current can be expanded as,

$$i_{\text{PD}} = i_{\text{PD, DC}} + i_{\text{PD,}\omega_m} + i_{\text{PD,}2\omega_m} + i_{\text{PD,}3\omega_m} + \dots \quad (2.42)$$

where,

$$i_{\text{PD, DC}} = \eta |E_0|^2 \sum |x_k E_k|^2, \quad (2.43)$$

$$i_{\text{PD,}\omega_m} = \eta |E_0|^2 \sum (x_k E_k (x_{k+1} E_{k+1})^* e^{-i\omega_m t} + \text{c.c.}), \quad (2.44)$$

$$i_{\text{PD,}2\omega_m} = \eta |E_0|^2 \sum (x_k E_k (x_{k+2} E_{k+3})^* e^{-2i\omega_m t} + \text{c.c.}), \quad (2.45)$$

$$i_{\text{PD,}3\omega_m} = \eta |E_0|^2 \sum (x_k E_k (x_{k+3} E_{k+3})^* e^{-3i\omega_m t} + \text{c.c.}), \quad (2.46)$$

where c.c. stands for “complex conjugate”. The DC photo current (2.43) corresponds to the raw response drawn in blue in figure 2.5. The photo current of  $\omega_m$  (2.44) corresponds to the intensity modulation drawn in green in figure 2.5. This process is sometimes referred to as the optical heterodyne.

### Electrical Demodulation

In order to extract the length information, one needs to electrically demodulate the photo current of  $\omega_m$  (2.44) at the same frequency. Note that it is possible to extract the length signal by using the photo current of  $3\omega_m$ , which is explained in section 2.5.

In the demodulation process, there are two choices depending on the phase of the demodulation signal. One can use either sine signal or cosine

## 2.4. EXAMPLES OF THE FRONTAL MODULATION SCHEME

---

signal as a demodulation signal. Therefore there are also two independent demodulated signals as follows,

$$V^{(I)}(t) = \frac{1}{\tau} \int_{t-\tau}^t i_{\text{PD}}(t') \times \sin \omega_m t' dt', \quad (2.47)$$

$$V^{(Q)}(t) = \frac{1}{\tau} \int_{t-\tau}^t i_{\text{PD}}(t') \times \cos \omega_m t' dt', \quad (2.48)$$

where  $V^{(I)}$  is called the *in-phase* or simply I-phase signal,  $V^{(Q)}(t)$  is called the *quadrature-phase* or Q-phase signal and we set the I-V conversion factor to be 1 for simplicity. In a practical situation, the integration over time can be realized by inserting a low pass filter with a cut off frequency of  $1/\tau$ . Substituting equation (2.44) into the last equations, one can obtain

$$V^{(I)} = \eta \sum \text{Re} [x_k E_k (x_{k+1} E_{k+1})^*] \quad (2.49)$$

$$V^{(Q)} = \eta \sum \text{Im} [x_k E_k (x_{k+1} E_{k+1})^*] \quad (2.50)$$

Since  $x_k$  is the response of the interferometer and is a function of the length, the electrical demodulation yields the length information.

## 2.4 Examples of the Frontal Modulation Scheme

---

### 2.4.1 A Single Fabry-Pérot Cavity

The setup is shown in figure 2.7 where a laser illuminates an FP cavity through an electro-optic modulator (EOM). The EOM modulates the phase of the incident field at a frequency of  $\omega_m$ . Then the reflected light off from the cavity is picked off and delivered to a PD. After the demodulation of the signal, it is low-passed and yields a linear signal.

In the following calculations, only the carrier and first harmonics are taken into account for simplicity. From equation (2.36), the incident field is now reduced to a sum of three fields,

$$E = E_0 e^{i\omega_0 t} [-J_1(\Gamma) e^{-i\omega_m t} + J_0(\Gamma) + J_1(\Gamma) e^{i\omega_m t}]. \quad (2.51)$$

where we used the fact  $-J_1 = J_{-1}$ . Once these three fields couple with the cavity, the reflected light can be expressed by replacing  $x$  by the amplitude reflectivity  $r$  in equation (2.38),

$$E_{\text{PD}} = E_0 e^{i\omega_0 t} [-J_1 r(-\omega_m) e^{-i\omega_m t} + J_0 r(0) + J_1 r(\omega_m) e^{i\omega_m t}], \quad (2.52)$$

## CHAPTER 2. BASICS IN LASER INTERFEROMETRY

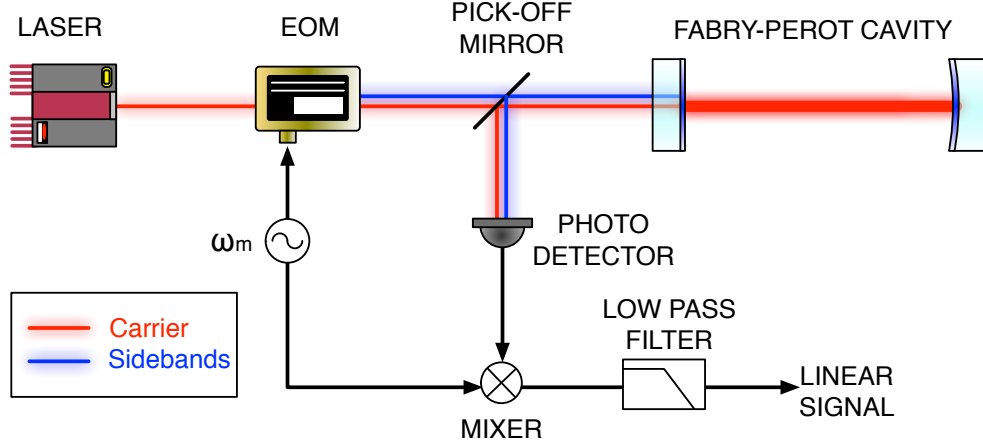


Figure 2.7: Setup for sensing the length of an FP cavity using the Pound-Drever-Hall scheme. A pair of upper and lower sidebands is imposed on the incident field by an EOM. The reflected light is delivered to a photo detector and then the photo current is electrically demodulated.

where  $r(\omega)$  is the amplitude reflectivity of the cavity at an angular frequency of  $\omega_0 + \omega$ , defined in equation (2.14). Then the squared detection is applied when the field hits the PD. We look into a specific current of  $\omega_m$ . From equation (2.44) we obtain a photo current of

$$i_{\text{PD}}(\omega_m) = 2J_0J_1 |E_0|^2 \text{Re} [r(0)r^*(\omega_m) - r^*(0)r(-\omega_m)] \cos \omega_m t + 2J_0J_1 |E_0|^2 \text{Im} [r(0)r^*(\omega_m) - r^*(0)r(-\omega_m)] \sin \omega_m t. \quad (2.53)$$

In the above equation the first term corresponds to the Q-signal and the second one corresponds to the I-signal. For simplicity the responsivity  $\eta$  is set to be 1. With the synchronous demodulation, we obtain the I-phase signal,

$$V^{(I)} = -2J_0J_1 |E_0|^2 \text{Im} [r(0)r^*(\omega_m) - r^*(0)r(-\omega_m)], \quad (2.54)$$

while the Q-phase signal doesn't give a meaningful signal. A calculated signal is shown in figure 2.8 as a function of the displacement in the baseline length.

To see the linearity of the signal, assume that the reflectivity for both the sidebands are identical and are real numbers when the carrier is in the vicinity of the resonance, so that  $r(\omega_m) \approx r(-\omega_m) \equiv r_s$ . In this case the I

## 2.4. EXAMPLES OF THE FRONTAL MODULATION SCHEME

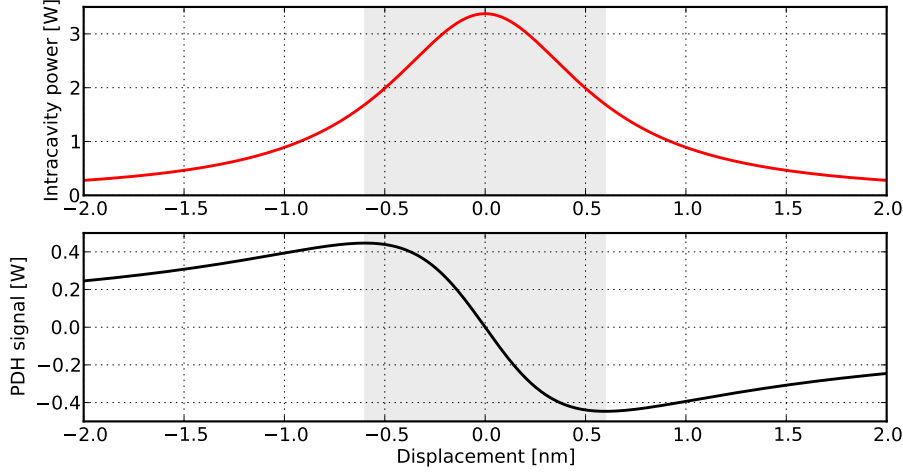


Figure 2.8: Intra-cavity power and PDH signal in the vicinity of the resonance. The shaded region corresponds to the cavity's full linewidth of 1.2 nm for  $\lambda = 1064$  nm,  $t_1^2 = 0.014$  and  $t_2^2 = 50$  ppm. The incident power of 1 W is assumed.

phase signal can be approximated by

$$V^{(I)} \approx -2J_0J_1|E_0|^2r_s \frac{t_1^2r_2}{(1-r_1r_2)^2} \phi_{\text{rtip}}. \quad (2.55)$$

It is clear that the signal is linear with respect to the round trip phase  $\phi_{\text{rtip}}$ . Therefore this is linear with respect to the length according to equation (2.12). Additionally the signal is also linear with respect to the laser frequency. The approximation is valid when it is within the linewidth as shown in figure 2.8.

Typically the modulation frequency is chosen such that the first order sidebands are close to the anti-resonance, when the carrier is on resonance. This condition makes the sensitivity higher and prevents the sidebands from the phase rotation as the sidebands are far from the resonance. However it is not preferable to choose the frequency exactly on the anti-resonance because under such a condition the second harmonic sidebands will resonate in the cavity simultaneously.

## CHAPTER 2. BASICS IN LASER INTERFEROMETRY

---

### Reading the Carrier's Phase

In the case of the single FP cavity the modulation scheme can be considered as a sensor reading out the carrier's phase. When the carrier is in the vicinity of a resonance the phase of the carrier drastically rotates while neither the amplitude nor phase of the sidebands are affected. Write the carrier field  $E_c$  as

$$E_c = E_0 e^{i(\omega_0 t - \Delta\phi)} \approx E_0 e^{i\omega_0 t} (1 - i\Delta\phi), \quad (2.56)$$

where  $\Delta\phi$  is the phase rotation due to the reflection by the cavity. The frequency of this field is then down converted to an RF of  $\omega_m$  through the squared detection at the PD, resulting in a photo current of

$$i_{\text{PD}, \omega_m} \propto (1 - i\Delta\phi) e^{i\omega_m t} + \text{c.c.} = \Delta\phi \sin \omega_m t + \cos \omega_m t. \quad (2.57)$$

An important point is that the sidebands serve as a local oscillator field — a reference oscillator which doesn't carry the information of the cavity but is used merely for down conversion of the frequency. From the last equation, it is clear that the information of the phase rotation is encoded in the I-phase signal (i.e.  $\sin \omega_m t$ ) while not in the Q-phase.

Figure 2.9 illustrate this situation by the phasor. The emphasis here is that the displacement of the FP cavity introduces the rotation of the phase for the carrier while it doesn't affect the sidebands. Hence the sidebands act as a local oscillator field and down-convert the frequency of the signals down to the RF.

### 2.4.2 Michelson Interferometer

In the case of a Michelson interferometer, the underlying physical process is slightly different from that of the FP cavity — the sidebands are affected instead of the carrier field.

According to equations (2.3) and (2.4), the reflectivity and transmissivity of a Michelson can be expressed by

$$r_{\text{MI}}(\omega) = -r \exp \left[ j \frac{\omega}{c} (l_x + l_y) \right] \cos \frac{\omega}{c} (l_x - l_y), \quad (2.58)$$

$$t_{\text{MI}}(\omega) = jr \exp \left[ j \frac{\omega}{c} (l_x + l_y) \right] \sin \frac{\omega}{c} (l_x - l_y), \quad (2.59)$$

## 2.4. EXAMPLES OF THE FRONTAL MODULATION SCHEME

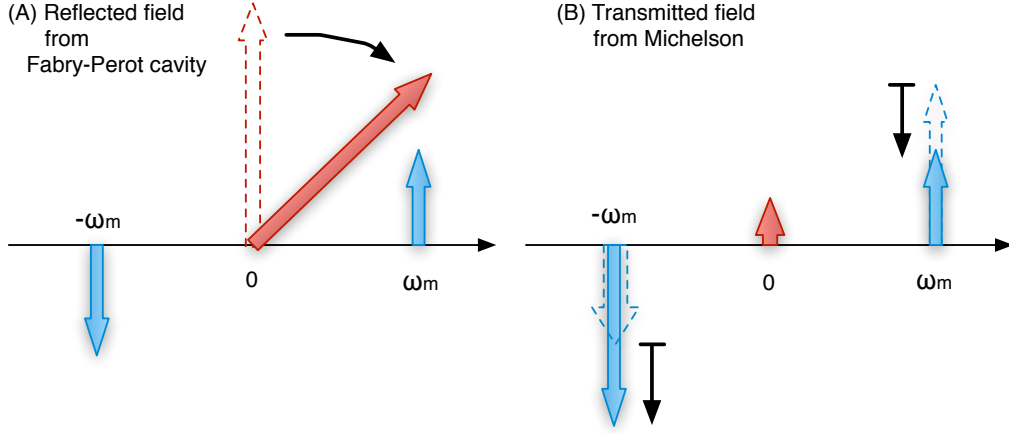


Figure 2.9: Phasor picture of (A) reflected field from an FP cavity and (B) transmitted field of a Michelson interferometer.

where  $r$  is the reflectivity of the end mirrors and we assumed a symmetric BS of  $r_{\text{BS}} = t_{\text{BS}} = 1/\sqrt{2}$ . By squaring the last two equations the power reflectivity and transmissivity,  $R_{\text{MI}}$  and  $T_{\text{MI}}$  are expressed as

$$R_{\text{MI}}(\omega) = \frac{r^2}{2} \left( 1 + \cos \frac{2\omega}{c} (l_x - l_y) \right), \quad (2.60)$$

$$T_{\text{MI}}(\omega) = \frac{r^2}{2} \left( 1 - \cos \frac{2\omega}{c} (l_x - l_y) \right). \quad (2.61)$$

The desired operating point for the Michelson in the GW interferometer is the dark fringe, where the transmissivity for the carrier becomes zero. To achieve the condition the frequency of the carrier and the lengths must satisfy the following relation,

$$\frac{2\omega_0}{c} (l_x - l_y) = 2\pi n \quad (n = 0, \pm 1, \pm 2, \dots). \quad (2.62)$$

### Schnupp Asymmetry

Consider a sideband, frequency of which is apart from the carrier by  $\omega_m$ . When the carrier is on the dark fringe the power transmissivity for the side-

## CHAPTER 2. BASICS IN LASER INTERFEROMETRY

---

band becomes,

$$T_{\text{MI}}(\omega_0 + \omega_m) = \frac{R}{2} \left( 1 - \cos \frac{2\omega_m}{c} (l_x - l_y) \right). \quad (2.63)$$

If the arm lengths are exactly the same,  $l_x = l_y$ , the transmissivity for the sidebands also becomes zero regardless of at what frequency the sideband is. This situation is not preferable as neither the carrier nor sidebands comes out to the anti-symmetric (AS) port and hence no information can be obtained. This is true even for the reflected light because the Michelson interferometer becomes a frequency-independent mirror.

A common trick to mitigate this issue is to introduce a macroscopic length difference, known as the *Schnupp asymmetry* invented in the late 1980's [41]. By introducing the Schnupp asymmetry, some fraction of the sideband becomes able to be transmitted through the Michelson interferometer and enables us to perform the modulation scheme. With a finite amount of the Schnupp asymmetry, the transmissivity of the sideband becomes,

$$T_{\text{MI}}(\omega_0 + \omega_m) \approx \frac{R}{2} \left( 1 - \cos \frac{2\omega_m}{c} l_{\text{sch}} \right), \quad (2.64)$$

where  $l_{\text{sch}} \equiv l_x - l_y$  denotes the Schnupp asymmetry.

### Reading the Amplitude Imbalance of the Sidebands

According to equation (2.44), a PD, placed at the reflection side, produces the photo current of  $\omega_m$ ,

$$i_{\text{PD}, \omega_m} = 2J_0 J_1 r(0) |E_0|^2 \text{Re} [r(\omega_m) - r(-\omega_m)] \cos \omega_m t, \quad (2.65)$$

where we neglected the 2nd and higher harmonic fields for simplicity. The current contains the subtraction between the upper and lower sidebands, appearing as  $r(\omega_m) - r(-\omega_m)$ . This means that the signal is derived from the imbalance in the amplitude of the reflected sidebands. After some algebra one can find

$$V^{(\text{Q})} = -J_0 J_1 r^2 E_0^2 \sin \left( \frac{2\omega_0}{c} \delta l \right) \sin \left( \frac{\omega_m}{c} l_{\text{sch}} \right), \quad (2.66)$$

where  $\delta l = l_x - l_y$  is the microscopic length variation that we desire to read out. The signal from the Michelson interferometer is a sine curve with a

---

## 2.5. THIRD HARMONIC DEMODULATION TECHNIQUE

---

period of  $\pi c/\omega_0$  in terms of  $\delta l$ . Note that this signal shows up only in the Q-phase.

A phasor picture of the transmitted field is given in figure 2.9. The way the fields behave is different from that of the FP cavity since the carrier light is not affected by the displacement, while the the amplitude of both the upper and lower sidebands are affected. One of the sidebands shrinks while the other expands or vice versa. Therefore in the case of a Michelson interferometer, the carrier plays a role of the local oscillator field and the signal is derived from the imbalance in the amplitude of the sidebands.

## 2.5 Third Harmonic Demodulation Technique

---

The 3rd Harmonic Demodulation (THD) technique is a family of the frontal modulation scheme, invented in 2000 [42]. It utilizes the third harmonic frequency for the electric demodulation, instead of the fundamental frequency. It decodes the phase information mainly from the first and second harmonic sidebands rather than a combination the carrier and the first harmonic sidebands such that it is less sensitive to variations in the carrier field.

A big advantage in the use of THD is that it can sense the dual-recycled Michelson interferometer (DRMI) without a significant obstruction from an arm FP cavity, which dramatically changes both the phase and amplitude of the carrier light during the lock acquisition process. The further discussions can be found in section 3.5.

One drawback is that the amplitude of the THD signal is smaller than that demodulated at the fundamental frequency  $\omega_m$ , and hence it has a lesser signal-to-noise ratio. According to equation (2.37), the cross term made by the first and second harmonic sidebands have an amplitude proportional to  $\Gamma^3$ , while that of the fundamental frequency demodulation technique has an amplitude of  $\Gamma$ . Thus the THD signal is smaller by a factor of  $\Gamma^2$  when  $\Gamma < 1$ .

## 2.6 Second-Harmonic Generation

---

### 2.6.1 Overview

Using a nonlinear crystal one can obtain the second-harmonic of an electric field — the process is referred to as second-harmonic generation (SHG). In

## CHAPTER 2. BASICS IN LASER INTERFEROMETRY

---

the process, part of the energy of an electric field of frequency  $\omega$  propagating through a crystal is converted to that of a wave at  $2\omega$  [43]. The first experimental demonstration of SHG was reported in 1961 [44].

When an electromagnetic field enters a dielectric medium under the condition that its frequency is far from the electron resonances of the medium, the polarization of the electrons in the medium is given by

$$p = \epsilon_0 (\chi^{(1)} E + \chi^{(2)} E^2 + \chi^{(3)} E^3 + \dots), \quad (2.67)$$

where  $\epsilon_0$  is the permittivity of vacuum,  $E$  is the applied electric field, and  $\chi^{(1)}$ ,  $\chi^{(2)}$ , and  $\chi^{(3)}$  are the linear or first-order, second-order, and third-order susceptibilities of the medium, respectively. Since the second term in the last equation is made of the square of the fundamental field, it produces a polarization at  $2\omega$ . This is the trick to produce the second-harmonic field.

### 2.6.2 Conversion Efficiency

A fundamental and its second-harmonic fields propagating in a nonlinear crystal along the  $z$ -axis follows the following equations [45],

$$\frac{dE^{(\omega)}}{dz} = -\frac{\sigma}{2} \sqrt{\frac{\mu}{\epsilon}} E^{(\omega)} - i\frac{\omega}{2} \sqrt{\frac{\mu}{\epsilon}} dE^{(2\omega)} (E^{(\omega)})^* e^{-i\Delta kz}, \quad (2.68)$$

$$\frac{dE^{(2\omega)}}{dz} = -\frac{\sigma}{2} \sqrt{\frac{\mu}{\epsilon}} E^{(2\omega)} - i\omega \sqrt{\frac{\mu}{\epsilon}} d (E^{(2\omega)})^2 e^{i\Delta kz}, \quad (2.69)$$

where  $E^{(\omega)}$  and  $E^{(2\omega)}$  are the fundamental and second-harmonic fields respectively,  $\sigma$  is the conductivity,  $\mu$  is the magnetic permeability,  $\epsilon$  is the permittivity,  $d$  is the nonlinear coefficient of the medium, and  $\Delta k$  is the phase difference in the wave numbers defined by,

$$\Delta k \equiv k^{(2\omega)} - k^{(\omega)}, \quad (2.70)$$

where the superscripts  $(\omega)$  and  $(2\omega)$  represent that they belong to the fundamental and second-harmonic fields respectively. Those are the basic equations for interaction of  $E^{(\omega)}$  and  $E^{(2\omega)}$ . It is shown that they are coupled to each other via the nonlinear constant  $d$  — without  $d$  the two fields are independent and hence  $E^{(\omega)}$  can not pump up  $E^{(2\omega)}$  at all.

Neglecting the absorption in the medium ( $\sigma = 0$ ) and assuming no depletion in the fundamental field, we obtain an equation for the approximated

---

## 2.6. SECOND-HARMONIC GENERATION

---

second-harmonic field,

$$\frac{dE^{(2\omega)}}{dz} = -i\omega\sqrt{\frac{\mu}{\epsilon}}d(E^{(2\omega)})^2 e^{i\Delta kz}. \quad (2.71)$$

Integrating the equation along the  $z$ -axis from 0 to the crystal length of  $l$ , and squaring the both sides of the equation, one can obtain

$$|E^{(2\omega)}(l)|^2 = \left(\frac{\mu}{\epsilon_0}\right)^{3/2} \frac{\omega^2 d^2 l^2 \sin^2(\Delta kl/2)}{n^2 (\Delta kl/2)^2}, \quad (2.72)$$

where we used the relation  $\epsilon = n^2 \epsilon_0$  with  $n$  the refractive index. Assuming the beam is confined in a cross section of  $A$ , one can define the total power as,

$$P = \frac{A}{2} \sqrt{\frac{\epsilon}{\mu}} |E|^2. \quad (2.73)$$

Using the last two equations, we obtain the conversion efficiency,

$$\eta_{\text{SHG}} \equiv \frac{P^{(2\omega)}}{(P^{(\omega)})^2} = 2 \left(\frac{\mu}{\epsilon_0}\right)^{3/2} \frac{\omega^3 d^2 l^2 \sin^2(\Delta kl/2)}{An^3 (\Delta kl/2)^2}. \quad (2.74)$$

Note that the conversion efficiency has an unit of per watts or conventionally %/W.

The efficiency  $\eta_{\text{SHG}}$  depends on the cross section  $A$  as well as the phase difference  $\Delta k$ . It indicates that a tightly focused beam could result in a high second-harmonic power, but however it is not so straightforward. The issue related to  $A$  is discussed in section 2.6.5, and those related to  $\Delta k$  is discussed in the following sections.

### 2.6.3 Phase-Matching and Coherence Length

In order to exploit the second-harmonic power in an efficient manner, one needs to consider the phase matching — the fundamental field must coherently pump up the second-harmonic field along its propagation through a medium.

An efficient SHG is achieved when  $\Delta k = 0$  according to equation (2.74). Hence the wave numbers for the fundamental and second-harmonic fields satisfy the following condition,

$$k^{(2\omega)} - k^{(\omega)} = 0. \quad (2.75)$$

Such a condition is referred to as bulk birefringent phase-matching (BPM). The BPM condition can be achieved by carefully choosing the relation between the propagation and crystal axes [46, 47]. The second-harmonic power with BPM is drawn in figure 2.11 as a function of the crystal length  $l$ . The power increases in proportion to  $l^2$ .

Although BPM is convenient, it has a few severe disadvantages. The phase matching range is restricted by the birefringent and dispersive properties of the nonlinear material. Moreover, the effective nonlinear coefficients vary, depending on both the propagation and polarization directions of the interacting beams.

On the other hand if  $\Delta k \neq 0$ , the second-harmonic field at a certain propagation distance is not in-phase to the one at another distance. As a consequence they are not coherently pumped up and the resultant second-harmonic power is reduced by the factor of

$$\frac{\sin^2(\Delta kl/2)}{(\Delta kl/2)^2}. \quad (2.76)$$

Analyzing this factor one can define the coherence length  $l_c$ , which is a measure of the maximum crystal length that is useful in producing the second-harmonic power. It is defined by

$$l_c = \frac{2\pi}{\Delta k}. \quad (2.77)$$

If the length of a crystal is at  $l = l_c$ , the interference term expressed by equation (2.76) reaches a local maximum, and hence this is efficient. However once the length becomes longer than the coherence length, the produced power then starts decreasing. Therefore elongation of the interaction length doesn't help the efficiency any more. Figure 2.11 shows the second-harmonic power as a function of the crystal length with  $\Delta k \neq 0$ . Note that the coherence length wouldn't be longer than 0.1 mm in most cases [48].

### 2.6.4 Quasi Phase-Matching with Periodically Poled Crystal

An alternative approach to satisfy the phase-matching condition is the quasi phase-matching (QPM) technique [49]. QPM is a relatively new technique, but is getting more popular nowadays because quasi-phase-matched crystals have access to the largest nonlinear coefficient for nonlinear optical processes.

## 2.6. SECOND-HARMONIC GENERATION



Figure 2.10: (Left) A homogeneous single crystal. (Right) A periodically poled crystal where the positive crystalline axis alternates in orientation with a certain period.

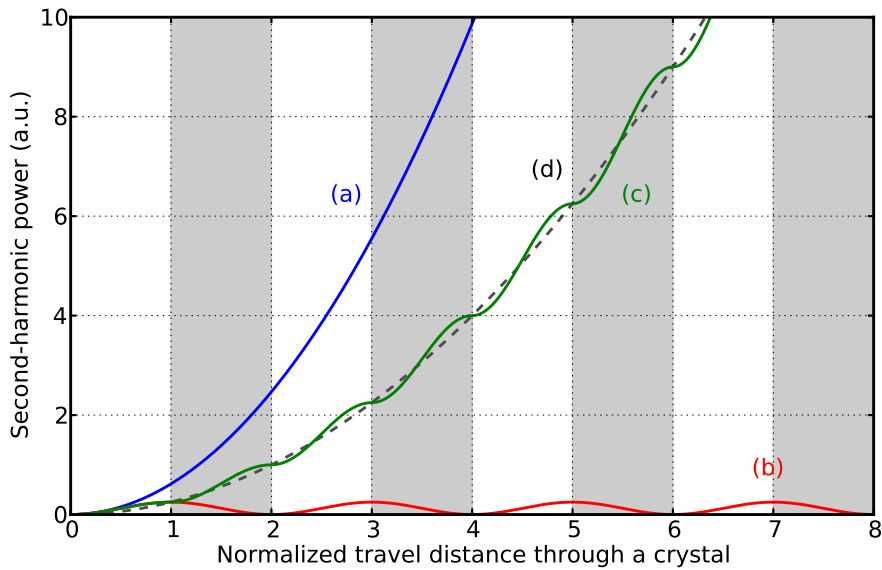


Figure 2.11: Second-harmonic power as a function of the normalized travel distance through a crystal. The  $x$ -axis is scaled such that the value denotes the number of the PP domains that the field encounters. The shaded regions represent the domains that have the opposite nonlinear coefficient. (a) BPM with  $\Delta k = 0$ . (b) non-phase matched case, where  $\Delta k \neq 0$ . (c) QPM with a PP crystal ( $\Delta k' = 0$  for  $m = 1$ ). (d) Approximated curve for QPM.

## CHAPTER 2. BASICS IN LASER INTERFEROMETRY

---

In the technique, a periodically poled (PP) crystal is used. The PP crystals are fashioned in such a way that the direction of one of its principal axes is reversed periodically as shown in figure 2.10. There are several advantages in the use of QPM. QPM can be achieved even with a material which has a small birefringence, and also QPM allows any choice of the wavelength by a correct choice of the period of the domain inversion as long as the material is transparent at the wavelengths .

Consider a crystal with its nonlinear coefficient  $d$  periodically changing along the propagation axis, say  $z$ -axis. With the Fourier transform, the periodic coefficient can be expanded as

$$d(z) = d_{\text{bulk}} \sum_{m=-\infty}^{\infty} a_m \exp\left(im \frac{2\pi}{\Lambda} z\right), \quad (2.78)$$

where  $\Lambda$  is the period of  $d(z)$  and

$$a_m = \frac{1}{\Lambda} \int_0^{\Lambda} \frac{d(z)}{d_{\text{bulk}}} \exp\left(-im \frac{2\pi}{\Lambda} z\right) dz. \quad (2.79)$$

By using  $d(z)$ , equations (2.68) and (2.69) can be rewritten as

$$\frac{dE^{(\omega)}}{dz} = -\frac{i\omega}{2} d_{\text{bulk}} E^{(\omega)} (E^{(2\omega)})^* \sum_{m=-\infty}^{\infty} a_m \exp(i\Delta k' z), \quad (2.80)$$

$$\frac{dE^{(2\omega)}}{dz} = -i\omega d_{\text{bulk}} (E^{(\omega)})^2 \sum_{m=-\infty}^{\infty} a_m \exp(i\Delta k' z), \quad (2.81)$$

where we neglected the absorption term by letting  $\sigma = 0$  for clarity, and  $\Delta k'$  is the phase-mismatch in the wave numbers defined by  $\Delta k' \equiv 2\pi m/\Lambda - k^{2\omega} + k^{(\omega)}$ .

Similarly to the phase-matching condition of BPM (2.75), the phase-matching condition for QPM can be achieved when

$$\Delta k' = m \frac{2\pi}{\Lambda} - k^{(2\omega)} + k^{(\omega)} = 0. \quad (2.82)$$

A nonlinear crystal for QPM is typically fabricated such that  $d(z)$  is spatially periodic with  $d(z)$  that switches from  $d_{\text{bulk}}$  to  $-d_{\text{bulk}}$  every  $\Lambda/2$ . In this case

$$a_m = \frac{1 - \cos m\pi}{m\pi} \quad \text{for } m \neq 0, \quad (2.83)$$

## 2.6. SECOND-HARMONIC GENERATION

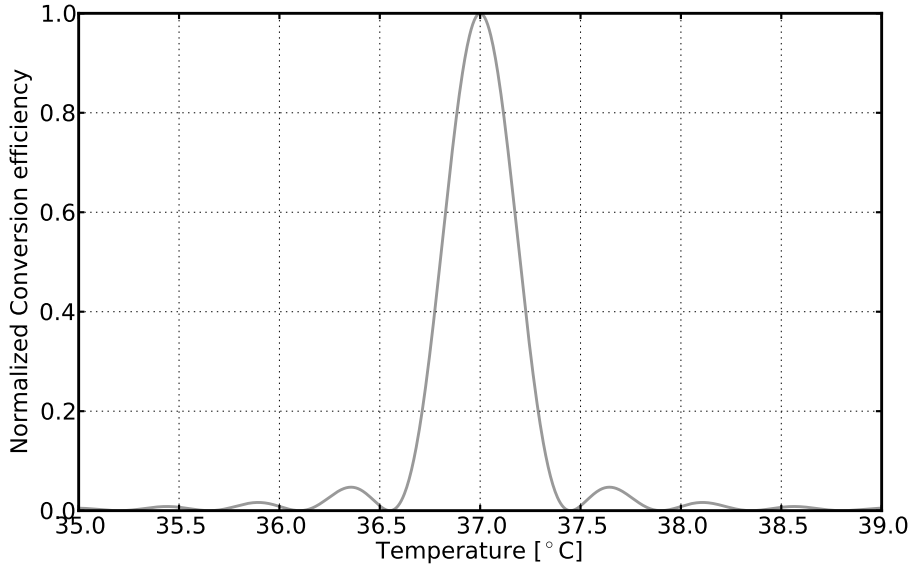


Figure 2.12: Conversion efficiency of a PPKTP crystal as a function of temperature.  $T_0 = 37.0$  °C,  $\alpha = 6 \times 10^{-6}$ , and  $l = 30$  mm are assumed.

so that choosing  $m = 1$ , the effective nonlinear coefficient is given by,

$$d_{\text{eff}} = a_m d_{\text{bulk}} = \frac{2}{\pi} d_{\text{bulk}}. \quad (2.84)$$

Therefore the QPM configurations can give rise to the same conversion efficiency as that in BPM, except that a longer interaction length is required to achieve it due to the factor of  $2/\pi$  in equation (2.84).

Figure 2.11 shows the second-harmonic power with the use of QPM as a function of the travel distance through a crystal. As shown in the figure the power grows up while it oscillates as the domain flips periodically. This is the consequence of the fact that the sign of  $d$  flips before the second-harmonic power starts decreasing due to  $\Delta k \neq 0$ . The power in QPM can be approximated by using equations (2.74) and (2.84), and it is also shown in the figure as a dashed-curve.

### Conversion Efficiency Against Temperature

Since the temperature of a crystal expands the grating period of  $\Lambda$ , it results in a mismatch in  $\Delta k'$  and hence leads to a variation in the conversion efficiency [50]. Therefore it is necessary to stabilise the temperature to efficiently exploit the second-harmonic power.

A mismatch in the wave numbers caused by the temperature can be given by

$$\Delta k' = \frac{2\pi}{\Lambda(T)} - \frac{2\pi}{\Lambda_0}, \quad (2.85)$$

where  $\Lambda(T)$  is a variation in the grating period driven by the temperature and  $\Lambda_0$  is the nominal grating period when the temperature is at a nominal value of  $T_0$ . In this case  $\Lambda(T)$  can be expressed by

$$\Lambda(T) = \Lambda_0 + \alpha l (T - T_0), \quad (2.86)$$

where  $\alpha$  is the expansion coefficient. Figure 2.12 depicts the normalized conversion efficiency of a periodically poled  $\text{KTiOPO}_4$  (PPKTP) crystal [51] against the temperature. As shown in the figure the maximum efficiency can be achieved at around  $T_0$  with a range of about  $1^\circ\text{C}$  when the length is set to be 30 mm.

### 2.6.5 SHG with a Focused Gaussian Beam

In the design phase of an interferometric experiment in which the QPM technique is utilized for SHG, the estimation of the second-harmonic power or equivalently conversion efficiency is crucial. This is because it potentially limits the sensitivity of the interferometric system and may limit even the choice of apparatuses.

According to equation (2.74), key factors are the phase relation  $\Delta k$  and the cross section of the beam  $A$ . As described in the previous section the phase relation can be optimized by controlling the temperature. In this section we consider the remaining factor, that is the beam size.

The objective here is to estimate the conversion efficiency of a PP crystal as a function of the waist size of the beam that propagates through the crystal. In the GW interferometer the Gaussian beam is generally used as a standard mode of the laser beam.

If the beam is tightly focused on a crystal, it could give us a high efficiency because the efficiency is inversely proportional to  $A$ . However SHG occurs

## 2.6. SECOND-HARMONIC GENERATION

---

mainly in a region around the focal point because a tightly focused beam expands rapidly and hence the other region of the crystal is not efficiently used. Therefore one must find a proper waist size at which the second-harmonic power is maximized. Two analytical solutions, which are helpful for coarse estimation, and a numerical calculation are described in detail below.

### A. Cylindrical Plane Wave

Consider a cylindrical beam, radius of which is approximated by that of a Gaussian beam at  $z = l/2$ , and assume that the wavefront is always plane normal to the propagation axis. In this case the radius is given by,

$$w = w_0 \sqrt{1 + \frac{l}{2Z_R}}, \quad (2.87)$$

where  $w_0$  is the waist size and  $Z_R = 2\pi n w_0^2 / \lambda$  is the Rayleigh range of the Gaussian beam for the fundamental field [52] with  $n$  the refractive index. If the intensity across the section of the cylinder is uniform, then the effective area is given by  $A = \pi w^2$ . Therefore, according to equation (2.74), the efficiency can be estimated as,

$$\eta_{\text{SHG}} = \frac{4}{\pi^3 c} \left( \frac{\mu}{\epsilon_0} \right)^{3/2} \frac{\omega^3 d^2 l^2}{n^2} \frac{1}{Z_R (1 + (Z/2Z_R)^2)}. \quad (2.88)$$

The estimation of the power using this approximation is drawn in figure 2.13 as curve (A). Since this approximation doesn't focus the beam, the estimation tends to be underestimated.

### B. Gaussian Beam without Depletion

Next we let the beam shape more realistic. In order to take the beam shape into account, the basic equation (2.68) and (2.69) need to be modified so as to include the spatial distribution of the electric field across the  $x$ - $y$  plane. A more general version of these two equations can be written as

$$\frac{\partial E^{(\omega)}}{\partial z} = \frac{i}{2k^{(\omega)}} \nabla_r^2 E^{(\omega)} - i \frac{\omega^2 d}{k^{(\omega)} c^2} E^{(2\omega)} E^{(\omega)*} e^{-i\Delta k z}, \quad (2.89)$$

$$\frac{\partial E^{(2\omega)}}{\partial z} = \frac{i}{2k^{(2\omega)}} \nabla_r^2 E^{(2\omega)} - 2i \frac{\omega^2 d}{k^{(2\omega)} c^2} (E^{(\omega)})^2 e^{-i\Delta k z}. \quad (2.90)$$

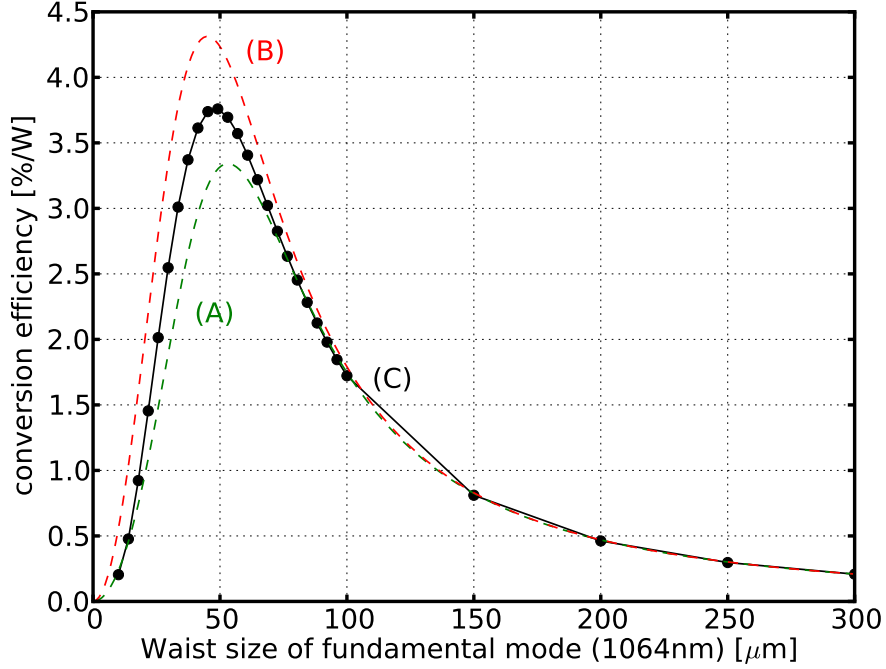


Figure 2.13: Conversion efficiency of a PPKTP crystal as a function of the beam waist size. All of them are calculated under the condition that the beam waist is located at the center of the crystal length.  $\lambda = 1064$  nm,  $n = 1.8$ ,  $l = 30$  mm and  $d = 13.8$  pm/V are assumed. (A) Cylindrical beam. (B) Gaussian beam without depletion. (C) Numerical simulation.

where we neglected the absorption for simplicity and  $\nabla_r^2 = (1/r)(\partial/\partial r)(r\partial/\partial r)$  is the transverse Laplacian. Note that the transverse Laplacian is independent of the angle  $\varphi$  because the Gaussian beam is axi-symmetric.

For a collinear Gaussian beam, the last equations can be reduced into 1D equations by integrating them along  $r$  in advance [53, 54]. In this case the second-harmonic field evolves with the following equation,

$$\frac{\partial A^{(2\omega)}}{\partial z} = -\frac{i}{2\sqrt{2Z_R}(1 - iz/Z_R)} K_1 f(z) (A^{(\omega)})^2 \exp(i\Delta kz), \quad (2.91)$$

where  $f(z)$  denotes the grating function and  $A(z)$  is related to the Gaussian

---

## 2.6. SECOND-HARMONIC GENERATION

---

field  $E(r, z)$  via,

$$E(z, r) = A(z) \sqrt{\frac{\omega_j}{\pi n w_0 (1 - iz/Z_R)}} \frac{\sqrt{j}}{\exp\left[-\frac{jr^2}{w_0^2 (1 - iz/Z_R)}\right]}, \quad (2.92)$$

where  $j$  denotes the order of harmonics, so that  $j = 1$  for the fundamental and  $j = 2$  for the second-harmonic fields.  $K_1$  is defined by

$$K_1 = d \sqrt{\frac{\omega^5}{\pi c^3 n^2}}. \quad (2.93)$$

Assuming that the medium is periodically poled and quasi phase-matched, we can set the interference term according to equation (2.84) as,

$$f(x) \exp(i\Delta kz) = \frac{2}{\pi}. \quad (2.94)$$

Setting the waist at the center of the crystal length and integrating equation (2.91) along  $z$  from  $-l/2$  to  $l/2$ , we find

$$\eta_{\text{SHG}} = 8 \left(\frac{\mu}{\epsilon_0}\right)^{3/2} \frac{\omega^2 d^2 Z_R}{n^2 \lambda} \arctan^2\left(-\frac{l}{2Z_R}\right). \quad (2.95)$$

The estimation of the power using this approximation is also drawn in figure 2.13 as curve (B). Since this approximation doesn't take the depletion into account, the result tends to be overestimated.

### C. Gaussian Beam with Depletion

The analytical solutions shown above are derived under the assumption that there are no depletion. This is valid as long as  $\eta \ll 1$ . However as shown in figure 2.13,  $\eta$  of a PPKTP crystal of 30 mm has an order of  $10^{-2}$  when the waist is properly chosen. Hence the depletion could be effective under such a circumstance. In order to more accurately estimate the conversion efficiency a numerical calculation should be performed.

The efficiency can be obtained by directly solving the coupled equation (2.89) and (2.90). The result of a numerical simulation is shown in figure 2.13 as curve (C).

The simulation was performed with a 2-dimension Gaussian beam with a computationally meshed PPKTP crystal in a number of grids. The calculation followed the descriptions in reference [54] with the third-harmonic field

## CHAPTER 2. BASICS IN LASER INTERFEROMETRY

---

neglected. In the simulation a  $1 \times 30$  mm crystal is prepared with the focal point at the middle of the crystal and  $400 \times 100000$  grids are arranged in the 2D crystal plane.

As shown in the figure the efficiency of the numerical solution agrees with that of the analytical estimations when the waist size is large. At around the optimum point of about  $50 \mu\text{m}$ , the non-depletion Gaussian model (B) gives slightly higher efficiencies than that of the numerical solution (C) as expected. On the other hand the cylindrical model (A) gives smaller efficiencies as expected.

### 2.7 Summary of the Chapter

---

- The fundamentals of the Michelson interferometer and Fabry-Pérot optical cavity are presented.
- Two dynamical responses of the Fabry-Pérot cavity are introduced. The cavity acts as a filter with respect to variations in the laser frequency and baseline length.
- The mathematical treatment and two practical applications of the frontal modulation scheme are presented. The sideband picture gives a comprehensive view of how the phase-modulated field couples with the interferometer.
- The basics of second-harmonic generation is introduced. In order to exploit the second-harmonic power efficiently, the temperature of the nonlinear crystal needs to be stabilised and also the applied Gaussian field needs to be appropriately focused on the crystal.

# 3

## Multi-Color Interferometry for Lock Acquisition

Lock acquisition is a necessary process to engage the active control acting on the length of the optical cavities. Therefore lock acquisition is a critical process in the operation of the gravitational-wave (GW) interferometer.

However there are several issues which hinder the lock acquisition process and hence the process is not straightforward. The difficulties associated with lock acquisition come mainly from two facts — (1) the response of an optical cavity is highly nonlinear and (2) the optical cavities forming the GW interferometer are optically coupled to each other.

In order to address the issues a multi-color interferometric technique, which utilizes a frequency-doubled auxiliary laser, has been proposed. This technique can provide a wide linear range with respect to the arm Fabry-Pérot (FP) cavity, such that the nonlinear issue can be mitigated. Moreover the technique allows us to always control the interferometric state of the arm FP cavities such that the arms will not couple with the other part of the interferometer. Therefore it reduces the degrees of the complexity in the multiply-coupled optical cavities system.

This chapter describes the difficulties in lock acquisition and the multi-color technique. Section 3.1 gives an introduction of lock acquisition. In section 3.2, several difficulties in a single FP cavity are discussed. Section 3.3, the difficulties of the multiply-coupled optical cavities are discussed. Section 3.4 describes the multi-color interferometric technique, which can mitigate the nonlinearity and the complexity of the multiple-cavities. Section 3.5 gives an overview of the planned full-lock-acquisition process with the aid of the multi-color interferometry.

## CHAPTER 3. MULTI-COLOR INTERFEROMETRY FOR LOCK ACQUISITION

---

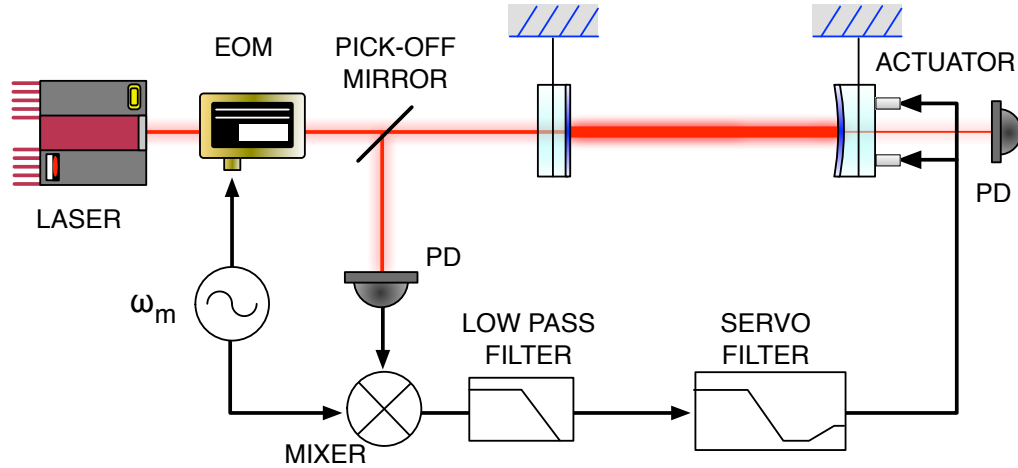


Figure 3.1: Setup for locking a single suspended Fabry-Pérot cavity.

### 3.1 Introduction

---

#### 3.1.1 Lock Acquisition

The process bringing an interferometer from its initial uncontrolled state (where the suspended mirrors are swinging freely) to the final operating state (where all cavity lengths are interferometrically controlled) is referred to as *lock acquisition*.

With a complicated configuration utilizing multiply-coupled cavities such as the GW interferometer, there are no reliable optical signals providing cavity length information until all cavities are simultaneously on the operating point. As a consequence lock acquisition is not so straightforward. In fact it is getting more difficult in the GW interferometer. The difficulties are discussed in detail in sections 3.2 and 3.3.

#### 3.1.2 Example : Single Fabry-Pérot Cavity

To get a very definite picture of lock acquisition, we argue a simple example, where a single suspended FP cavity is considered. Although the actual 2nd generation (2G) interferometer has not only an FP cavity but also three more optical cavities and a Michelson interferometer, the picture, introduced here,

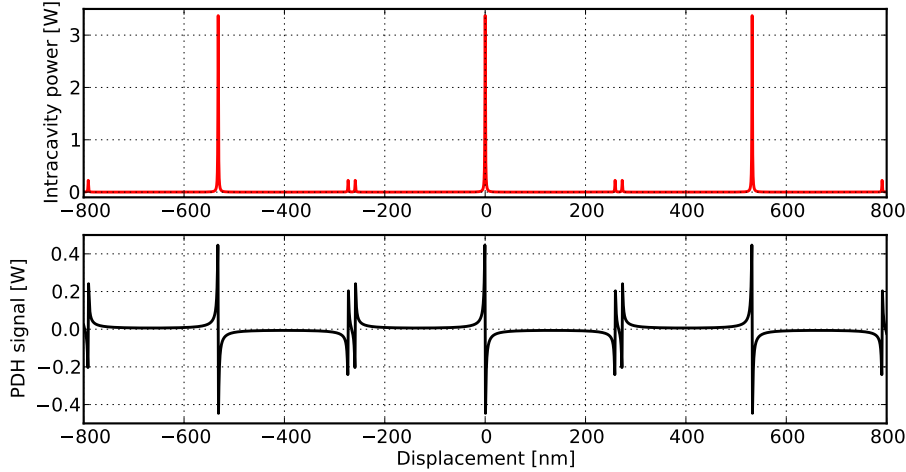


Figure 3.2: (Upper plot) intra-cavity power as a function of the displacement from the resonance point, calculated. (Lower plot) PDH signal as a function of the displacement from the resonance point, calculated. In the calculations  $L = 3994.5$  m,  $\Gamma = 0.5$ ,  $\omega_m/2\pi = 9099471$  MHz,  $t_1^1 = 0.014$  and  $t_2^2 = 50$  ppm are assumed.

essentially holds true.

The setup is shown in figure 3.1 where two mirrors of an FP cavity are suspended by wires. The standard Pound-Drever-Hall (PDH) scheme is used for extraction of the length signal of the cavity (see section 2.4.1). The PDH signal is passed to a servo filter and then to the coil magnet actuator in order to correct the length. As an auxiliary monitor, a photo detector (PD) is placed at the transmission side of the cavity. To make the discussion clearer, the FP cavity is assumed to be well aligned and to move only along the input beam axis.

The objective here is to bring the cavity length to a resonance point by the active control and then keep it there. As explained in section 2.2 the FP cavity exhibits resonances with a period of its free spectral range (FSR). Linear signals can be obtained only when it is in the vicinity of a resonance.

Typically lock acquisition can be achieved as follows. Initially the cavity swings freely with a displacement of a few 100 nm or  $1 \mu\text{m}$  due to seismic noise. Since the resonances appear with a period of  $\lambda/2 \approx 500$  nm with  $\lambda$

## CHAPTER 3. MULTI-COLOR INTERFEROMETRY FOR LOCK ACQUISITION

---

the laser wavelength, the seismic excitation provides a spontaneous length scan. Therefore the cavity occasionally passes through a resonance. Once the cavity starts crossing a resonance the active control starts feeding the signals back to the length and then keep it on the resonance.

In the case of the actual GW interferometer, the same process is applied to each optical cavity as well as the Michelson interferometer until all of them are locked. Once all the cavities and Michelson interferometer are locked, the control servos are switched to the ones dedicated to low noise control in order to start the observation.

### 3.1.3 Toward the 2nd Generation Interferometer and Beyond

Lock acquisition of the 2G interferometer will be more difficult because of the following two reasons.

One of the reasons is the addition of one more optical cavity. The first generation (1G) interferometers used to have four length degrees of freedom (DOFs), but in the 2G interferometer it becomes five DOFs because the signal recycling cavity (SRC) will be newly added. Generally increasing the number of the DOFs makes the length sensing and control more difficult. This is because that the degree of the complexity of the signal extraction gets higher due to the fact that the optical cavities are coupled to each other in a more complex way. Therefore lock acquisition also becomes more complex in the sense the length signals are more entangled.

The other reason is more serious and comes from the fact that the 2G interferometer aims to be more sensitive than the 1G interferometers. Consequently the length actuator of the arm cavity mirrors are designed to be weaker than it used to be in order to reduce electronics noises, which are associated with the actuators. Therefore it leads to the risky situation where the active length control can not stop the motion of the optical cavities. This issue is discussed in section 3.2.

Although it is not impossible to stop the motion of the cavities with the weak actuators in the 2G interferometer, it is going to be extremely difficult in the future interferometers. In the future detectors the sensitivity can be designed to be significantly higher and hence the actuators need to be very weak. In this case lock acquisition can not be achieved with the conventional strategy any more.

---

## 3.2. DIFFICULTIES IN A SINGLE FABRY-PÉROT CAVITY

---

Therefore it is time to review the lock acquisition strategy and also develop a new scheme which can robustly work in the 2G interferometer and even in the future interferometers. As will be discussed in detail in the subsequent sections, the multi-color interferometry presented in this thesis is a possible solution.

### 3.2 Difficulties in a Single Fabry-Pérot Cavity

---

In this section we discuss the difficulties in lock acquisition of a single FP cavity. A single FP cavity is simple but is enough to describe a number of particular difficulties associated with lock acquisition of the GW interferometer. Additionally several mitigation techniques are listed for completeness in section 3.2.4, although unfortunately these mitigations don't meet the requirement for the 2G interferometers.

#### 3.2.1 Kinematic Limit

There is a limit in lock acquisition of a single FP cavity due to the nonlinearity. If the speed of the cavity motion exceeds a certain value, the active control cannot capture it [55]. Since the proper length signal can be available only in the limited range around a resonance, the active control must be able to stop the motion within the range.

According to the conservation law of the kinetic energy, the following condition must be satisfied [56, 57, 58] in order to stop the motion,

$$\frac{1}{2}mv^2 \leq FL_{\text{FWHM}}, \quad (3.1)$$

where  $m$  is the mass of the mirrors,  $v$  is the velocity of the cavity length,  $L_{\text{FWHM}}$  is the full linewidth defined in (2.18) and  $F$  is the maximum available actuator force. This indicates that the kinetic energy of the cavity motion must be less than the work done by the actuator in a range of  $L_{\text{FWHM}}$ .

Therefore for a system with  $F$  and  $L_{\text{FWHM}}$  given, the velocity of the cavity motion must satisfy,

$$v \leq \sqrt{\frac{F\lambda}{m\mathcal{F}}}, \quad (3.2)$$

where we used expressions (2.18) and (3.1). If this condition is not satisfied, the active control can not lock the single FP cavity.

## CHAPTER 3. MULTI-COLOR INTERFEROMETRY FOR LOCK ACQUISITION

---

In the case of the arm FP cavity in advanced LIGO (aLIGO), the threshold velocity is estimated to be 200 nm/s with  $F = 200 \mu\text{N}$ ,  $m = 40 \text{ kg}$  and  $\mathcal{F} = 450$  assumed. Lock acquisition of the arm FP cavity can not be so easy because the velocity of the cavity motion will be at the same order.

### 3.2.2 Distortion in Signals

When the cavity passes through a resonance with a velocity of higher than a certain value, the length signal starts being distorted. This phenomenon is known as the *Doppler ringing* effect [59]. This effect can be potentially problematic because it flips the sign of the length signal.

The threshold velocity is related to its storage time  $\tau_s$  and finesse  $\mathcal{F}$  [60]. It is expressed by

$$v_{\text{th}} = \frac{L_{\text{FWHM}}}{\tau_s} \approx \frac{\pi c \lambda}{4L \mathcal{F}^2}, \quad (3.3)$$

where  $L$  is the baseline length of the FP cavity. Therefore the Doppler ringing occurs more frequently if  $L$  and  $\mathcal{F}$  are large. This is likely the case for the km-scale GW interferometers. For example, in the case of the arm FP cavity in aLIGO, the storage time is about  $\tau_s = 3.8 \text{ msec}$  for  $L = 4 \text{ km}$  and  $\mathcal{F} = 450$ . This results in a threshold velocity of  $v_{\text{th}} = 320 \text{ nm/s}$ . Since the speed of the cavity motion will be at the same order, this effect can be frequently observed in aLIGO and hence the active control will be disturbed.

### 3.2.3 Acquisition Failure

When the active control fails to lock the cavity, it can potentially accelerate the cavity motion unnecessarily. This can be also a potential issue because the mirrors will be well isolated from seismic noise through several isolation stages in the 2G interferometer, and such failure can spoil the quietness. Consequently the failure makes the locking more difficult as the mirror velocity becomes larger. Moreover it is not preferable to try locking the cavity with failure, particularly multiple times, because it leads to a direct excitation of the well isolated mirrors.

### 3.2.4 Mitigations

On the basis of the kinematic requirement (3.1), the mitigations can be categorized to three types, each of which corresponds to an improvement in

---

### 3.2. DIFFICULTIES IN A SINGLE FABRY-PÉROT CAVITY

---

$v$ ,  $L_{\text{FWHM}}$  and  $F$  respectively as described below.

#### Slowing Down the Velocity

A straightforward way to mitigate the difficulties is to lower the mirror velocity  $v$  by some means. Perhaps employing a better vibration isolation system is an intuitive solution. However such a system can suppress only the mirror motion locally — each of the mirrors is quiet, but the distance between them is still uncontrolled.

Besides it, the Suspension Point or Platform Interferometry (SPI) [61, 62] provides us with a slowed cavity. The SPI, originally proposed in 1987 [63], suppresses the motion between suspension platforms or suspensions points by interferometrically controlling the length. Therefore the SPI enables us to slow down the motion of the cavity instead of the local mirror motions.

#### Expansion of the Linear Range

If the velocity  $v$  and force  $F$  are given, another approach is to expand the linear range of the length signal  $L_{\text{FWHM}}$ . There have been several studies for the expansion. This type of mitigations can be further categorized to three types — (1) manipulations in the available optical signals, (2) modification of the modulation and demodulation processes, and (3) extrapolation of the cavity motion.

As for the first category, there is a method which utilizes the transmitted power leaking through the end mirror as a normalization factor with respect to the demodulated signals [64, 65]. There is another method which also utilizes the transmitted power, but manipulates it as

$$\text{Length signal} = \frac{1}{\sqrt{P_{\text{tr}}}} + \text{offset}, \quad (3.4)$$

where  $P_{\text{tr}}$  is the power of the transmitted light [66, 67]. This gives a linear signal in a wider range and is useful when one desires to lock the cavity at a point slightly off from a resonance although the signal vanishes when the cavity is exactly on the resonance.

In the second category, there is a novel technique which uses a broadband phase modulation instead of the standard monochromatic phase modulation (i.e. frontal modulation scheme). This technique is called the digital interferometry [68, 69]. Besides, a careful choice of the demodulation phase with

## CHAPTER 3. MULTI-COLOR INTERFEROMETRY FOR LOCK ACQUISITION

---

the standard frontal modulation scheme can also provide a wider linear range [70].

In the third category, there is an advanced technique which extrapolates the motion of the cavity from the available optical signals and hence virtually expands the linear range [55].

### More Powerful Actuator

The last possibility to alleviate the difficulties is to increase the available maximum force applied on the mirrors. However increasing  $F$  is not practical because the coupling factor for the electronics noise generally increases as  $F$  increases. Therefore it leads to a larger noise injection to the cavity length and hence spoils the ultimate sensitivity of the GW interferometer. Moreover the electronics noise associated with the actuator is known as one of the well identified noise sources [71]. Therefore this option is useful only for lock acquisition but is not preferable for the precision measurements and low-noise control required for the GW observation.

## 3.3 Difficulties in Multiply-Coupled Optical Cavities

---

### 3.3.1 Overview

As discussed in the previous sections, the difficulties associated with a single FP cavity can be mitigated in various ways. However a system with multiply-coupled optical cavities is more difficult to lock because the signal is generally a mixture of all the optical cavities. Moreover each length signal is nonlinear.

Generally such a system doesn't show reliable length signals until all the DOFs are simultaneously on the operating point. In such a complicated system, lock acquisition typically proceeds in multiple steps as a progression. In each step of the progression one or more DOF is locked to the operating point, and a certain interferometric state is established step by step along the sequence until all the DOFs are fully engaged. However there is an issue which hinders the progression due to the multiply-coupled cavities.

In this section the length DOFs are explained in section 3.3.2 and then the typical acquisition progression is explained in section 3.3.3. Section 3.3.4 describes the main difficulty, which is obstruction from the arm FP cavity to

### 3.3. DIFFICULTIES IN MULTIPLY-COUPLED OPTICAL CAVITIES

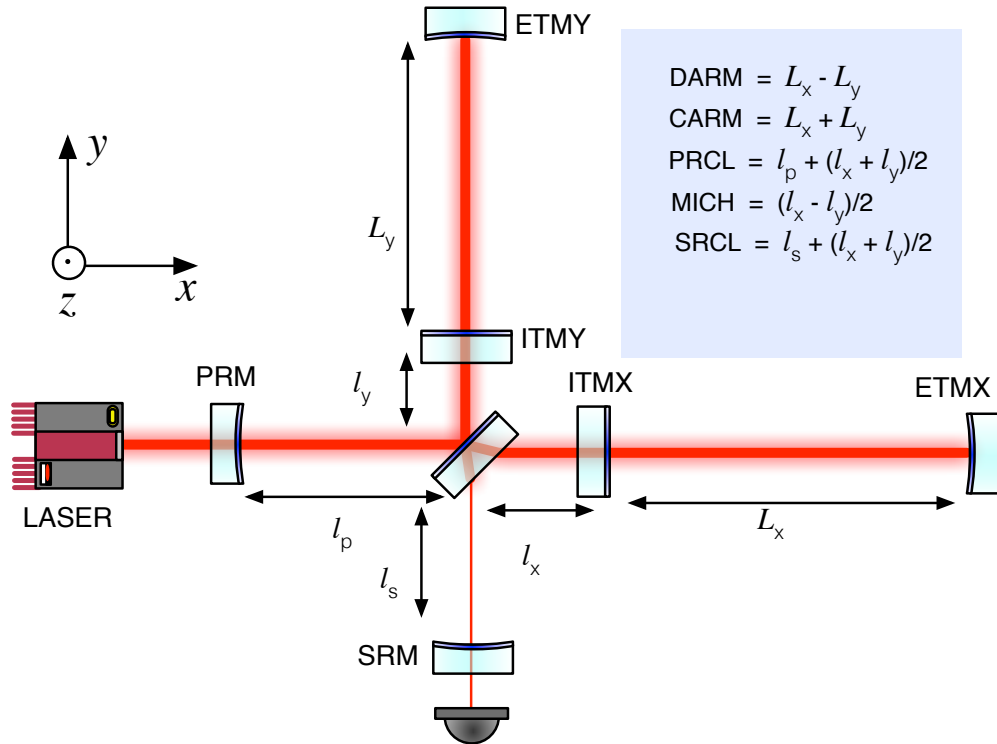


Figure 3.3: Definition of the canonical length degrees of freedom in the 2nd generation interferometer.

the control of the rest of the interferometer. Finally section 3.3.5 discusses a possible solution, which leads to the use of the multi-color interferometry.

#### 3.3.2 Length Degrees of Freedom

In the 2G interferometer there are five length DOFs that must be controlled to achieve the desired interferometric condition. Figure 3.3 illustrates the optical configuration of the 2G interferometer as well as the length notations and definitions. The definitions are summarized below.

## CHAPTER 3. MULTI-COLOR INTERFEROMETRY FOR LOCK ACQUISITION

---

### DARM and CARM

DARM (Differential ARM motion) is the differential motion between the length of two arms. This is the most important DOF among five, as DARM contains GW signals. It is conventionally defined as

$$L_{\text{DARM}} = L_x - L_y. \quad (3.5)$$

CARM (Common motion in ARMs) denotes the common motion in two arm cavities, defined by

$$L_{\text{CARM}} = L_x + L_y. \quad (3.6)$$

### XARM and YARM

Although DARM and CARM are convenient DOFs for the control the final steady state, alternatively these can be dealt as individual arms (i.e.  $L_x$  and  $L_y$ ). In this case each arm length  $L$  must satisfy the following condition,

$$\frac{4\pi\nu}{c}L = 2\pi n \quad (n: \text{integer}). \quad (3.7)$$

These DOFs can be chosen particularly during the lock acquisition because DARM and CARM are inaccessible unless both the arms are brought to the vicinity of the resonance with active control.

### PRCL, MICH and SRCL

PRCL (Power Recycling Cavity Length) represents the effective optical length of Power Recycling Cavity (PRC). It is defined as a sum of the optical distance from the power recycling mirror (PRM) to the beam splitter (BS) and the mean arm lengths of the Michelson interferometer as follows,

$$L_{\text{PRCL}} = l_p + \frac{l_x + l_y}{2}. \quad (3.8)$$

Therefore it is formed by PRM, BS and input test masses (ITMs). PRCL must be controlled such that the following resonant condition is satisfied,

$$\frac{4\pi\nu}{c}L_{\text{PRCL}} = 2\pi n \quad (n: \text{integer}). \quad (3.9)$$

### 3.3. DIFFICULTIES IN MULTIPLY-COUPLED OPTICAL CAVITIES

This condition enables to reflect the light, that would leave from the arm cavities toward the laser source, and hence the light is recycled.

MICH (MICHelson) represents the short Michelson part, consisting of two ITMs and BS. It is defined by

$$L_{\text{MICH}} = l_x - l_y. \quad (3.10)$$

MICH must be kept at the dark fringe such that it satisfies,

$$\frac{2\pi\nu}{c} L_{\text{MICH}} = 2\pi n \quad (n: \text{integer}). \quad (3.11)$$

This condition ensures a small amount of the light leaking to the anti-symmetric (AS) port and hence decreases the shot noise due to the bulk light.

SRCL (Signal Recycling Cavity Length ) is the effective optical length of Signal Recycling Cavity (SRC). It is formed by the sum of the distance from the signal recycling mirror (SRM) to BS and the mean arm lengths of the Michelson interferometer. It is defined by

$$L_{\text{SRCL}} = l_s + \frac{l_x + l_y}{2}. \quad (3.12)$$

For the signal recycling scheme, it must satisfy

$$\frac{4\pi\nu}{c} L_{\text{SRCL}} = 2\pi n \quad (n: \text{integer}). \quad (3.13)$$

#### 3.3.3 The Lock Acquisition Progression

Typically lock acquisition of the GW interferometer proceeds in multiple steps. There have been a scheme to fully lock the 2G interferometer by using a combination of the frontal modulation signals and a number of intra-cavity power signals [66, 67].

In the scheme the dual-recycled Michelson interferometer (DRMI) is firstly captured with the frontal modulation signals in order to stabilise the field that enters the arm cavities. Then each arm cavity is locked one by one.

Figure 3.4 illustrates a simplified diagram of the 2G interferometer and its associated frontal modulation readout system. The incident field is phase-modulated at two different frequencies and hence two sideband fields are

## CHAPTER 3. MULTI-COLOR INTERFEROMETRY FOR LOCK ACQUISITION

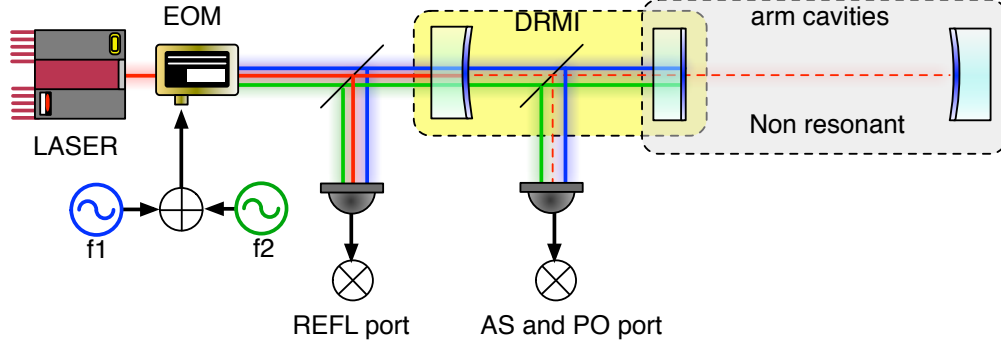


Figure 3.4: Simplified diagram of the DRFPMI locking. For simplicity one of the arm cavities are not shown and also the DRMI is approximated by a two-mirror cavity. This illustrates the situation in which the DRMI is engaged but the arms are not. The DRMI and the arm cavities are optically coupled to each other. The red, blue and green beam represent that of the carrier, pair of the  $f_1$  sidebands and pair of the  $f_2$  sidebands. REFL and PO stand for “reflection” and “pick off” respectively.

imposed by an electro-optic modulator (EOM). When the DRMI is locked alone, the sideband fields are resonant in the DRMI while the carrier is *anti-resonant*. At this point the arm cavities are away from a resonance.

Then keeping the lock of the DRMI, one has to wait for the arms to pass through a resonance for the carrier. Once both the arm cavities are locked on the resonance for the carrier, the sign of the reflectivity of the arm cavity flips only for the carrier. As a result the PRC becomes resonant for the carrier while the sidebands continue to be resonant. This drastic change forces the carrier to enter the interferometer (i.e. power recycling).

### 3.3.4 Obstruction from the Arm Cavities

The issue is that lock acquisition of the arm cavities is rather difficult because the arm cavities occasionally satisfy an undesired interferometric state. When the undesired state is satisfied it destroys the control of the rest of the interferometer by introducing obstruction in their length signals. As it will be explained in the following paragraphs, this phenomena is *inevitable* as

### **3.3. DIFFICULTIES IN MULTIPLY-COUPLED OPTICAL CAVITIES**

long as the frontal modulation scheme are used as a sensor.

#### **Obstruction due to the Sideband Resonance**

If one of the arms happen to pass through a resonance for the sidebands, it flips the sign of the reflectivity of the arm for the sideband. It indicates that the arm motion rotates the phase of the sidebands, and therefore the DRMI signals are contaminated.

Suppose that the DRMI is locked by the frontal modulation signals, and an arm cavity is in the region between the resonances for the carrier and sidebands as depicted in figure 3.5. To make the argument clearer, we assume that ITMs are at rest and leave the end test masses (ETMs) freely swing.

In one of the arms, if the ETM is moving toward a resonance for the carrier, it will be successful because the carrier's resonance is the desired operating point. However, on the other hand, if the ETM is moving toward the other side, where a resonance for the sidebands exists, it will lead to obstruction in the DRMI signals.

When an arm passes through a resonance for the sidebands, the arm will drastically rotate the phase of the sideband fields reflected off from the cavities, and hence changes the standard readout condition (described in section 2.4.1) of the DRMI. This is a rather serious issue because once the arm cavity disturbs the lock of the DRMI, it can destruct the lock and hence one has to start over the progression again. This is true even in the use of the third-harmonic demodulation (THD) technique.

#### **The Probabilistic Lock Acquisition**

According to the argument illustrated in figure 3.5, for one of the arm cavities, the probability of such obstruction happening is 50% under the assumption that the active control doesn't fail to capture the arm. Since the GW interferometer has one more arm cavity, the same argument is applied to the other arm, resulting in a total success probability of 25%.

Therefore lock acquisition of the 2G interferometer has been said to be *probabilistic*. Once the DRMI is locked it will be destructed by the arm cavities with an optimistic probability of 75%. This situation is, of course, not preferable since such a process doesn't allow us to systematically diagnose the process and also can not be reliable. Moreover if micro-seismic noise, which typically arises at about 100 mHz, can bring the cavity velocity higher, easily

## CHAPTER 3. MULTI-COLOR INTERFEROMETRY FOR LOCK ACQUISITION

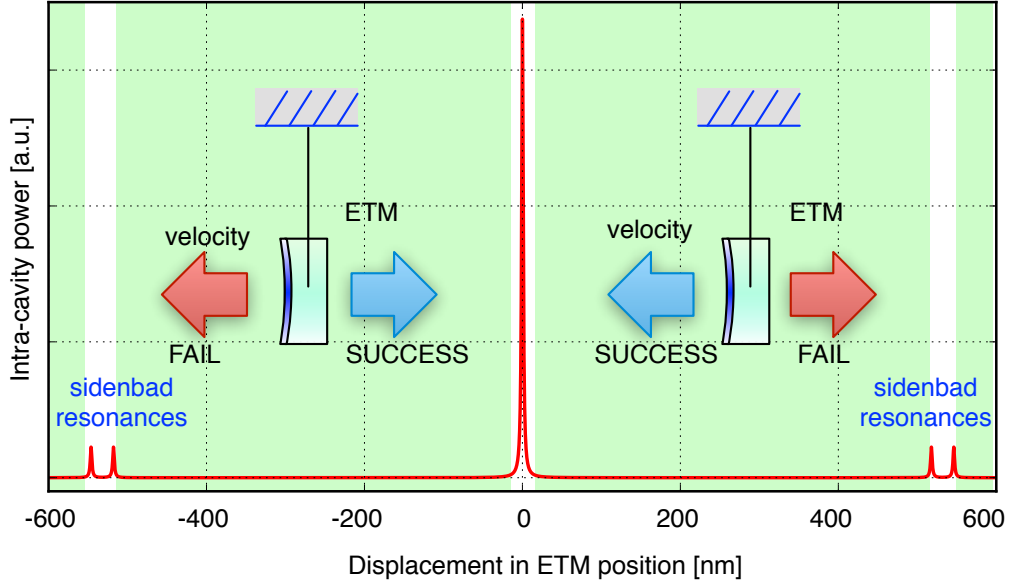


Figure 3.5: Intra-cavity power against displacement in the ETM position. The ETM position is initially in the green-shaded regions. Lock acquisition is probabilistic depending which direction the ETM moves. If the ETM moves toward the sideband resonance, it will destroy the control of the rest of the interferometer.

resulting in a lesser success probability for full lock acquisition due to the kinematic limit (see section 3.2.1).

### 3.3.5 Arm Length Stabilisation as a Mitigation

The difficulties, described in the previous sections, originate from the fact that the arm lengths are uncontrolled until they are probabilistically locked. If the arm lengths are stabilised in advance to the lock progression, the obstruction can be fully mitigated. In this case the progression will be *deterministic*, except that the DRMI locking is still sensitive to the velocity

### 3.4. MULTI-COLOR INTERFEROMETRY FOR ARM LENGTH STABILISATION

---

of their cavity motions. However lock acquisition of the DRMI should be relatively easy because the length actuators are typically stronger and also their linewidths are wider than those of the arm cavities.

In order to stabilise the arm lengths, a possible approach is to employ an additional sensor which is sensitive to only the arm cavities such that the arm lengths can be stabilised at a certain value. So for the reason the following requirements can be set on the new sensor:

- The sensor must be able to readout only the displacement in the arm lengths in order to control only them.
- The linear range of the sensor must be much greater than the linewidth in order to mitigate the nonlinearity and also to bring the arm length at a desired value.

To satisfy the requirements, a multi-color interferometric technique has been proposed. The details are described in the next section.

## 3.4 Multi-Color Interferometry for Arm Length Stabilisation

---

### 3.4.1 Overview

In order to address the issues in lock acquisition of the 2G interferometer, a new multi-color interferometric technique, called *Arm Length Stabilisation* (ALS) has been proposed. The technique enables one to stabilise and bring the arm length to an arbitrary value independently of the state of the rest of the interferometer. The technique utilizes frequency-doubled auxiliary (AUX) lasers whose wavelength is the half of the ordinary 1064 nm wavelength in order to sense only the motion of the arm lengths.

Figure 3.6 depicts a simplified setup for ALS, that has been designed for aLIGO. Each AUX laser is placed at each end of the arm cavities and the frequency-doubled laser field is injected to the arm through the back of ETM. The mirrors in the arm cavity are coated as dichroic mirrors such that the AUX laser couples only with the arm cavity. The AUX laser propagates to the interferometer vertex through the cavity and then combined with a frequency-doubled sample of the main laser at a PD. Finally the signal produced from the photo detector is fed back to the length.

## CHAPTER 3. MULTI-COLOR INTERFEROMETRY FOR LOCK ACQUISITION

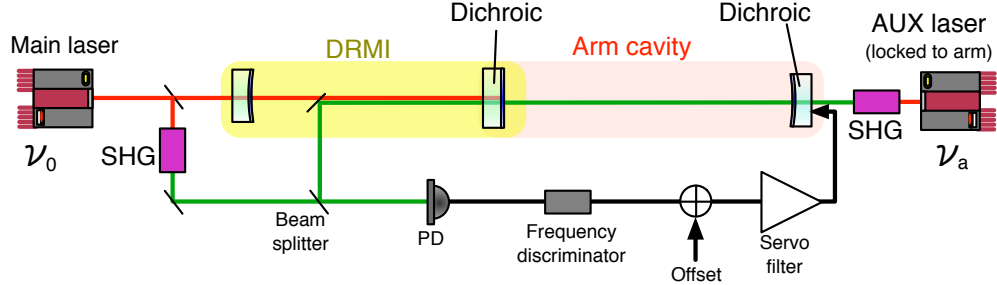


Figure 3.6: Schematic view of the multi-color interferometry setup for arm length stabilisation.

An advantage in the use of this multi-color technique is that it provides signals with a substantially wide linear range with respect to the arm length. Thus the active control can be immediately engaged without fail. Moreover it can control the arm lengths such that the arm cavities are optically decoupled from the rest of the interferometer because of the wide linear range. As a consequent it avoids obstructions in the DRMI signals. On the other hand, one drawback is that this technique requires a large number of additional hardwares such as electronics, mirrors and lasers.

Recently the technique has been chosen to be a standard technique for lock acquisition in aLIGO and KAGRA. Although the working principle of the ALS technique has been demonstrated by Mullavey et. al [12] in a short-baseline cavity, the ALS technique needed further tests in a more realistic configuration, which are summarized in chapter 5. Moreover the most important verification is the feasibility check — the noise performance must satisfy the requirement for aLIGO. This is summarized in chapter 6.

This section describes the working principle of the ALS technique. The system can be divided into three subsystems and each of them is explained in sections 3.4.2, 3.4.3 and 3.4.4 respectively. Then the requirements are discussed in section 3.4.5.

### 3.4.2 Auxiliary Lasers for Sensing the Arm Length

To provide another sensor for the arm lengths, frequency-doubled Nd:YAG (Nd-doped  $\text{Y}_3\text{Al}_5\text{O}_{12}$ ) lasers are introduced via second-harmonic generation

### 3.4. MULTI-COLOR INTERFEROMETRY FOR ARM LENGTH STABILISATION

---

(SHG). The fundamental wavelength of the Nd:YAG laser is at  $\lambda = 1064$  nm, and therefore the frequency-doubled laser is at 532 nm, which is visible and appears in green while the 1064 nm laser is invisible.

Each AUX laser is locked to the length of each arm cavity with the standard PDH technique (see section 2.4.1). In this case, according to equations (2.12) and (2.13), the round trip phase satisfies,

$$\phi_{\text{rtp}} = \frac{8\pi\nu_a(t)}{c}L(t) = 2\pi n, \quad (3.14)$$

where  $\nu_a$  is the fundamental frequency of the AUX laser and we assumed that the servo has the infinite gain and there are no noises for simplicity. To make the subsequent discussions clearer, we redefine the length and AUX frequency as

$$L(t) = \bar{L} + \delta L(t), \quad (3.15)$$

$$\nu_a(t) = \bar{\nu}_a + \delta\nu_a(t), \quad (3.16)$$

where  $\bar{L}$  and  $\bar{\nu}_a$  denote the constant nominal value of the arm length and AUX frequency respectively, and  $\delta L(t)$  and  $\delta\nu_a(t)$  denote deviation from the nominal value of the length and AUX frequency respectively. Plugging last two equations to equation 3.14, one can obtain

$$\frac{\delta\nu_a(t)}{\bar{\nu}_a} = -\frac{\delta L(t)}{\bar{L}}. \quad (3.17)$$

Therefore the frequency of the AUX laser is forced to follow a variation in the length  $\delta L$  by correcting its frequency. The amount of correction  $\delta\nu_a$  is proportional to the displacement  $\delta L$  from  $\bar{L}$ . It means that the length information is encoded in the frequency of the AUX laser field. Therefore, in principle, the length information can be extracted by observing the frequency of the AUX laser.

#### 3.4.3 The Main Laser as a Reference

When controlling the arm length, one needs a reference with respect to the arm length. In the case of the GW interferometer the reference can be the frequency of the main laser because the main laser needs to satisfy the desired interferometric state for the arm cavities. This can be done by employing a heterodyne beat-note measurement.

## CHAPTER 3. MULTI-COLOR INTERFEROMETRY FOR LOCK ACQUISITION

---

The transmitted frequency-doubled AUX laser through the arm is extracted through one of the mirrors in the DRMI as shown in figure 3.6. Then the AUX light is optically combined with a frequency-doubled sample of the main laser field at a beam splitter. The combined field at this point can be expressed by,

$$E = E_0 \exp(i4\pi\nu_0 t) + E_a \exp(i4\pi\nu_a t), \quad (3.18)$$

where  $E_0$  and  $E_a$  denote the amplitude of the electric field for the frequency-doubled main laser and the AUX laser respectively, and  $\nu_0$  is the fundamental frequency of the main laser. Detecting the power of this field, one can obtain a photo current of,

$$i_{\text{PD}} \propto |E|^2, \quad (3.19)$$

$$= P_0 + P_a + 2\sqrt{P_0 P_a} \cos(4\pi(\nu_0 - \nu_a)t), \quad (3.20)$$

where  $P_0 = |E_0|^2$  is the power of the main laser,  $P_a = |E_a|^2$  is that of the AUX laser and we neglected a high frequency term oscillating at  $2(\nu_0 + \nu_a)$  because it is too fast for a PD to observe.

As explained in the previous subsection, the length information is encoded in the frequency. Therefore we look into the frequency of the beat-note. According to the last expression, the beat-note term oscillates at a frequency of

$$f_{\text{beat}}(t) = 2(\nu_0 - \nu_a(t)). \quad (3.21)$$

Using equations (3.17) and (3.16) one can obtain,

$$f_{\text{beat}}(t) = 2(\nu_0 - \bar{\nu}_a) + 2\frac{\bar{\nu}_a}{L}\delta L(t). \quad (3.22)$$

Since  $\bar{\nu}_a$  is a constant, the last equation indicates that fluctuation in the beat-note frequency is essentially determined by the frequency of the main laser  $\nu_0$  and the length fluctuation  $\delta L$ . In fact this is exactly what we desire i.e. a measure of the length fluctuation with respect to the main laser frequency.

Since the DRMI is not involved in this scheme, the beat-note is essentially insensitive to the interferometric condition of the DRMI. Therefore it satisfies the first requirement listed in section 3.3.5.

### 3.4.4 Arm Length Stabilisation

As discussed in the previous subsection, the length information can be extracted from the beat frequency. Thus employing a frequency sensor for the

### 3.4. MULTI-COLOR INTERFEROMETRY FOR ARM LENGTH STABILISATION

---

beat-note, one can obtain the length signal and hence control the arm length. With an active control acting on the arm length, the beat frequency  $f_{\text{beat}}$  can be set at a desired value while the length fluctuation  $\delta L$  is suppressed. This is the principle of the arm length stabilisation.

In order for the main 1064 nm laser to be resonant in the arm cavity, it must satisfy the round trip condition (2.13). Therefore,

$$\nu_0 = m f_{\text{FSR}}, \quad (3.23)$$

where  $m$  is an integer and  $f_{\text{FSR}}$  is the free spectral range (FSR). On the other hand, according to equation (3.14), the AUX frequency satisfies,

$$\bar{\nu}_a = \frac{n}{2} f_{\text{FSR}}. \quad (3.24)$$

Therefore, from equation (3.22) the beat frequency must satisfy,

$$f_{\text{beat}} = 2m f_{\text{FSR}} - n f_{\text{FSR}}, \quad (3.25)$$

$$= \begin{cases} 2N f_{\text{FSR}} & (\text{for } n = \text{even number}) \\ (2N + 1) f_{\text{FSR}} & (\text{for } n = \text{odd number}) \end{cases} \quad (3.26)$$

where  $N$  is an integer and we assumed that  $\delta L$  is suppressed to zero. Therefore in order for the main laser to be resonant in the arm, the beat-note frequency must be either an odd number or even number multiple of the FSR, depending on  $n$ . This ambiguity is due to the fact that the frequency-doubled AUX laser is locked to the arm cavity. In both cases the resonances for the main 1064 nm laser appears with a period of  $2f_{\text{FSR}}$  in terms of the beat frequency.

Besides the stabilisation, another key function of the multi-color technique is that it allows us to bring the length to an arbitrary value as long as the beat-note signal is detected. This length tuning is done by introducing an offset in the observed beat frequency. In this case the beat frequency can be shifted to  $f_{\text{beat}} + f_{\text{offset}}$ , where  $f_{\text{offset}}$  is the artificial offset. Since the arm length servo tries to suppress the beat frequency to zero, the beat frequency is forced to be at

$$f_{\text{beat}} = -f_{\text{offset}}. \quad (3.27)$$

According to equation (3.17) the amount of the length offset due to the artificial frequency offset is given by,

$$L_{\text{offset}} = -\frac{\bar{L}}{2\bar{\nu}_a} f_{\text{offset}}. \quad (3.28)$$

## CHAPTER 3. MULTI-COLOR INTERFEROMETRY FOR LOCK ACQUISITION

---

Thus the addition of the offset allows one to scan the arm length arbitrarily.

An advantage of this technique is that one can keep obtaining the linear signal as long as  $f_{\text{beat}}$  is small enough for the PD and frequency sensor to process, . Therefore the multi-color technique can meet the second requirement listed in section 3.3.5 with a proper choice of the PD and frequency sensor.

### 3.4.5 Requirements

#### Residual Arm Displacement

In order to achieve full lock acquisition, the arm cavity must not accidentally pop into or out of the linewidth. According to equation (2.18), the residual displacement of the arm cavity in root mean square (RMS) must satisfy the following requirement,

$$\delta L_{\text{rms}} < 1.2 \text{ nm} \times \left( \frac{450}{\mathcal{F}} \right). \quad (3.29)$$

In the case of aLIGO, where  $\mathcal{F} = 450$ , the residual displacement in RMS must be less than 1.2 nm.

#### Separation of Two Green Lasers

In the use of the ALS technique there are two green (532 nm) lasers; one for each arm. They would make undesired interference, which can be readout through a PD and can be a noise source.

In order for two green lasers to be independent they are designed to have different polarizations. Moreover they are designed to have different frequency offsets with respect to the main laser. For instance, in the aLIGO ALS design, the frequency of one of them will be intentionally shifted by +80 MHz while the other will be shifted by -80 MHz.

#### Bandwidth of Frequency Measurement

A requirement on the bandwidth of the PD and frequency discriminator can be set from the FSR since it is required to sense at least an FSR to enable us to bring the length at an arbitrary value. According to equation (2.15),

$$f_{\text{FSR}} = 3.7 \text{ MHz} \left( \frac{40 \text{ m}}{L} \right). \quad (3.30)$$

### 3.5. FULL LOCK ACQUISITION WITH THE MULTI-COLOR INTERFEROMETRY

---

In the case where the baseline length is 40 m, the bandwidth for the beat-note measurement must be larger than or as large as  $2f_{\text{FSR}} = 7.6$  MHz.

Another requirement can be set from the fact that the beat-note fluctuates due to the displacement of the arm length, driven by seismic noise. Typically the displacement of a suspended cavity is about  $1 \mu\text{m}$  or lesser in RMS. In this case, the beat frequency fluctuates by

$$\delta f_{\text{beat}} \sim 7.0 \text{ MHz} \left( \frac{40 \text{ m}}{L} \right) \left( \frac{\delta L}{1 \mu\text{m}} \right). \quad (3.31)$$

Therefore the PD and frequency sensor must be able to detect such amount of the frequency range.

#### Modeling of Control Loops

The ALS system consists of a number of the active control loops and therefore, as will be discussed in section 6.1, the system needs to be analyzed with care. The modeling of the control loop is essential for one to design and refine the system. Moreover once the model is prepared one can perform a noise analysis based on the model, which is important for such a precise control scheme. We will return to this topic in chapter 6 because the model depends on the actual implementation and devices.

### 3.5 Full Lock Acquisition with the Multi-Color Interferometry

---

The planned full lock acquisition process in aLIGO with the aid of the multi-color interferometry is briefly described in this section.

#### 3.5.1 The Planned Lock Acquisition Process

Figure 3.7 illustrates the planned multi-step lock acquisition as a function of time. With the ALS the progression proceeds in the following steps [72].

##### 1. Engagement of the AUX Lasers

First of all each AUX laser must be locked to each arm cavity such that the transmitted light provides us with the arm displacement. Lock acquisition

## CHAPTER 3. MULTI-COLOR INTERFEROMETRY FOR LOCK ACQUISITION

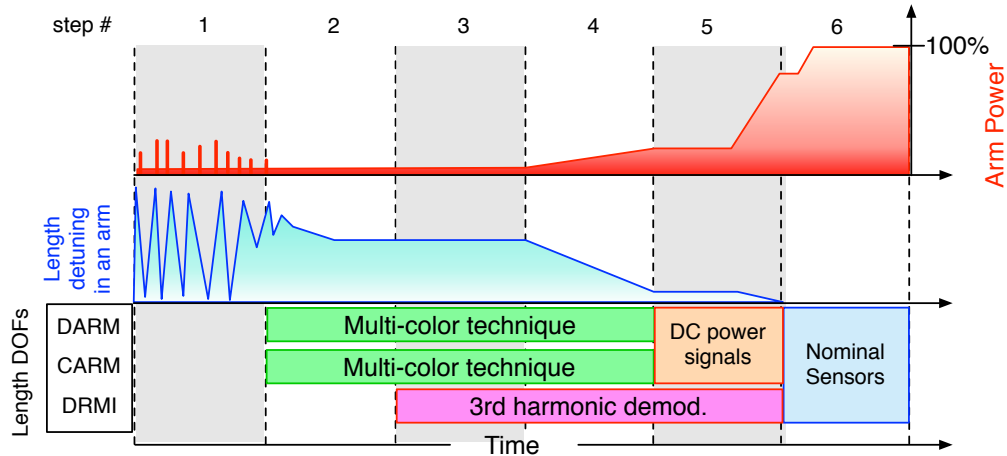


Figure 3.7: The planned full lock acquisition steps.

of the AUX laser loop should be relatively easy because the loop can be typically designed sufficiently fast such that the loop can capture a fringe without fail.

### 2. Arm Length Stabilisation

In this phase the arm cavities are stabilised by feeding the signal back to the ETMs. The controlled DOFs at this point can be either the combination of DARM and CARM [73] or the combination of XARM and YARM. After engaging the feedback loops, the arm cavities are brought to be a temporary operating point, which is apart from the resonance by about 10 nm, so that the arm cavities will not couple with the DRMI.

### 3. Locking the DRMI

After the engagement of the arm cavities the DRMI can be locked with the standard frontal modulation scheme. From the beginning or at some point of this phase, the sensors must be switched to the ones derived by the third harmonic demodulation (THD) technique (see section 2.5), so that the control of the DRMI becomes less sensitive to the resonant condition of the carrier.

---

## 3.6. SUMMARY OF THE CHAPTER

---

### 4. Reduction of the CARM Offset

Once the DRMI is engaged by the THD, one can bring the arm cavities closer to their resonance points. This process corresponds to a reduction of the CARM offset. In the current design the CARM offset will be reduced down to a point where the transmitted light from the arms are obtained with a sufficient signal-to-noise ratio. At this point a small fraction of the carrier light starts entering the arm cavities.

### 5. Handing Off of DARM and CARM

In this phase the sensors for the arm cavities are passed to the ones with higher sensitivities. CARM can be controlled by the signal derived from the DC reflection of the interferometer as well as the transmitted power of the arm cavities [72]. The DARM sensor can be switched to the signals derived from the transmitted arm powers [72, 67]. Note that this step can be skipped if the stability of the ALS control is far better than 30 pm, which is the linewidth of the CARM cavity formed by the arms and the power recycling cavity.

### 6. Switching to Nominal Sensors

After all the arm cavities are locked with the sensors that are derived from the 1064 nm main laser, the remaining offset in CARM will be progressively reduced. Then the sensors will be switched to the nominal sensors which are more sensitive. All the DOFs are at the operating point. At this point the AUX laser can be shut off because the lock acquisition sequence is completed.

## 3.6 Summary of the Chapter

---

- Lock acquisition is a necessary process to engage the active length control. The process brings the interferometer from the uncontrolled state to the interferometrically controlled state step by step.
- The kinematic limit comes from the fact that the actuator has a finite efficiency and the cavity has a finite velocity. Since the length actuator is getting weaker as the sensitivity of the interferometer increases, the kinematic limit is getting severer.

### CHAPTER 3. MULTI-COLOR INTERFEROMETRY FOR LOCK ACQUISITION

---

- In addition, a system with the multiply-coupled optical cavities leads to a serious issue. When the sideband resonates in the arm Fabry-Pérot cavity unnecessarily, it destroys the control of the dual-recycled Michelson interferometer as long as the frontal modulation scheme is used as a sensor.
- The multi-color technique provides a wider linear range with respect to the arm length and hence mitigates the issues related to the nonlinearity e.g. the kinematic limit.
- Moreover the technique allows to bring the arm lengths to an arbitrary value, such that the arm cavity doesn't obstruct the dual-recycled Michelson interferometer during lock acquisition.

# 4

## The 40-meter Prototype Interferometer

All the experimental tests described in this thesis were performed at the Caltech 40-meter prototype interferometer. The 40-meter interferometer, which is located on the campus of California Institute of Technology, is a testbed of advanced interferometric gravitational-wave (GW) detectors [55, 66, 74, 75, 76]. The interferometer had been upgraded since the late 2009 [77] in order to conduct several tests for the length sensing and control schemes that will be used in advanced LIGO.

In this chapter the experimental setups of the 40-meter prototype is explained in detail. Section 4.1 describes an overview of the interferometer and its associated facilities. Section 4.2 describes the vacuum system. Sections 4.3 and 4.4 describe the input optics and core optics respectively. Section 4.5 explains the photo detection system, including photo detectors and associated demodulation circuits. In section 4.6, the digital system is explained. In section 4.7, the suspension system is explained. Sections 4.8 and 4.9 explain respectively the second-harmonic generation system and the auxiliary laser setups which are necessary for the multi-color interferometry.

### 4.1 Overview

---

The 40-meter prototype interferometer is the only one full prototype interferometer of advanced LIGO (aLIGO) and is located on the campus of California Institute of Technology. The optical configuration is arranged to be the same as that of aLIGO, that is the dual-recycled Fabry-Pérot Michelson interferometer (DRFPMI).

This interferometer is used to prototype the length sensing and control schemes which will be used in aLIGO. One of the main goal is to demonstrate

## CHAPTER 4. THE 40-METER PROTOTYPE INTERFEROMETER

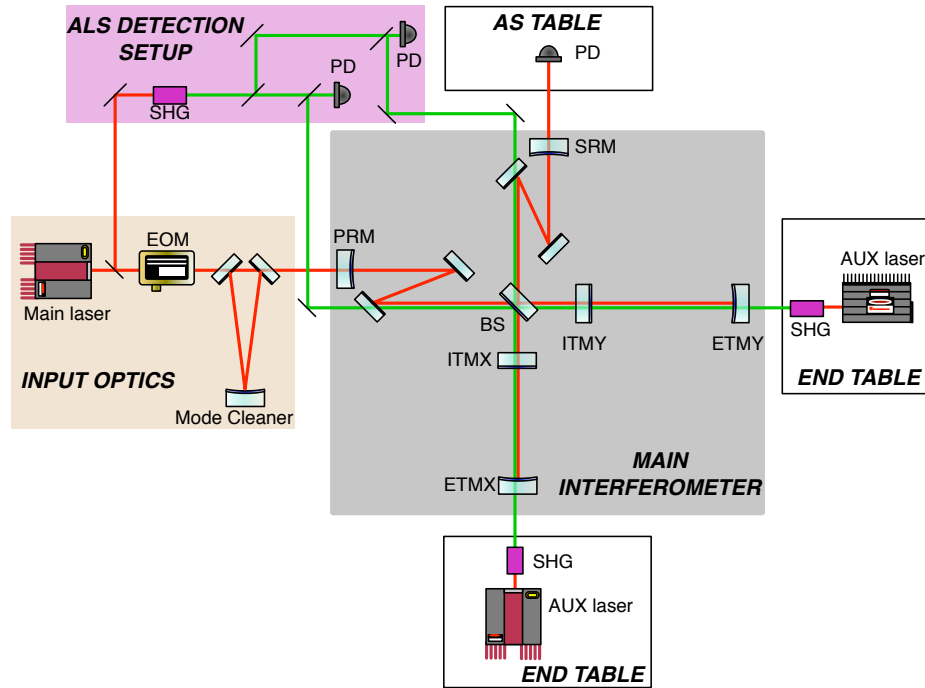


Figure 4.1: Schematic of the optical layout of the 40 meter prototype interferometer.

and verify the planned lock acquisition scheme, including the multi-color interferometric technique.

A schematic view of the optical layout is shown in figure 4.1. All the main optics are suspended as single-stage pendula to provide a vibration isolation. The entire interferometer is housed in an ultra-high vacuum envelope. The power recycling cavity (PRC) and signal recycling cavity (SRC) are folded by introducing two additional mirrors in each cavity.

After the course of the upgrade works starting from 2009, all the necessary optics has been installed in 2010 and the interferometer began working.

## 4.2 Vacuum System

The main interferometer as well as the 13-meter mode cleaner (MC) are housed in an ultra-high vacuum envelope. The vacuum envelope covers all the

## 4.2. VACUUM SYSTEM



Figure 4.2: Panorama picture of the 40-meter prototype facility. The picture was taken from the corner of the Michelson interferometer. It shows the  $x$ -arm vacuum tube on the left,  $y$ -arm vacuum tube in the middle, and the main laser booth (the one with blue doors) on the right of the picture.

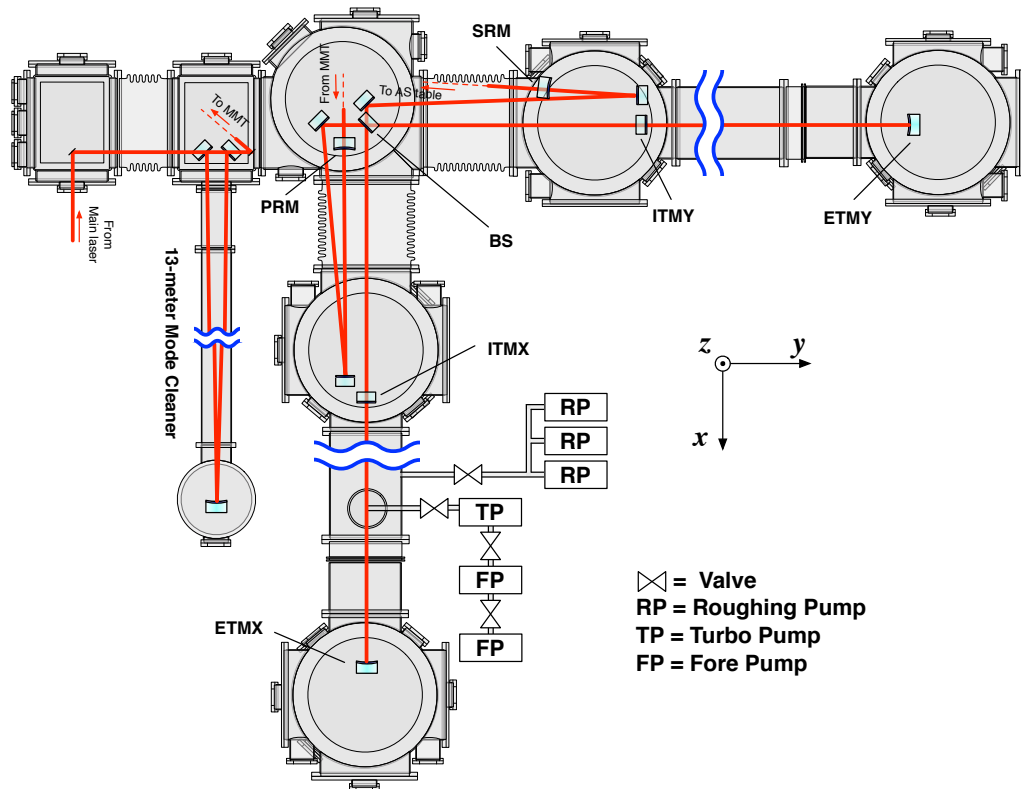


Figure 4.3: Schematic of the vacuum envelope. Red lines indicate the main laser path ( $\lambda = 1064$  nm). MMT stands for mode matching telescope.

## CHAPTER 4. THE 40-METER PROTOTYPE INTERFEROMETER

---

suspended core optics in order to reduce unwanted effects such as fluctuations of the refractive index in the laser path due to the residual gas, and also contaminations on the surface of the mirrors.

As illustrated in figure 4.3, the envelope consists of eight chambers and they are connected via vacuum tubes and flanges. There are no gate valves or a similar function to disconnect the volumes. Therefore the pumping system takes care of the entire volume at once.

The pumping system is connected near the end chamber of the  $y$  arm via valves as shown in figure 4.3. When the pressure is too high for the turbo pump to stably operate, instead two dry fore pumps are used to pump the pressure down to approximately 720 mTorr. Once it reaches this pressure, the pumps are switched to the turbo pump and it brings the pressure further down to the nominal value. This is particularly the case for the initial phase of the pumping from the atmospheric pressure.

In the nominal operation the mean pressure in the inside of the vacuum system is maintained at  $\sim 1 \times 10^{-4}$  Torr to allow for the precision laser interferometry. A turbo pump is always activated to keep the pressure low enough without injecting significant vibration to the envelope as well as optics.

### 4.3 Input Optics

---

The function of the input optics is to deliver a stable and clean laser source in terms of the spatial laser profile, intensity and frequency. The input optics include a number of the important subsystems, such as the main laser source, pre-mode cleaner (PMC), electro-optic modulator (EOM), and MC. Figure 4.4 shows a schematic of the optical layout of the input optics that are installed on an optical bench.

#### 4.3.1 Main Laser Source

The 1064 nm light source is a 2 W Innolight Nd:YAG laser [78] and is a non planar ring oscillator (NPRO) [79] type laser. This main laser is conventionally called pre-stabilised laser (PSL) among the LIGO laboratory. As explained in section 4.3.4 the PSL frequency is stabilised with an active feedback control. The main laser is optically isolated from its back stream by introducing a Faraday rotator and a set of the polarizing beam splitters (PBSs) as shown in figure 4.4.

### 4.3. INPUT OPTICS

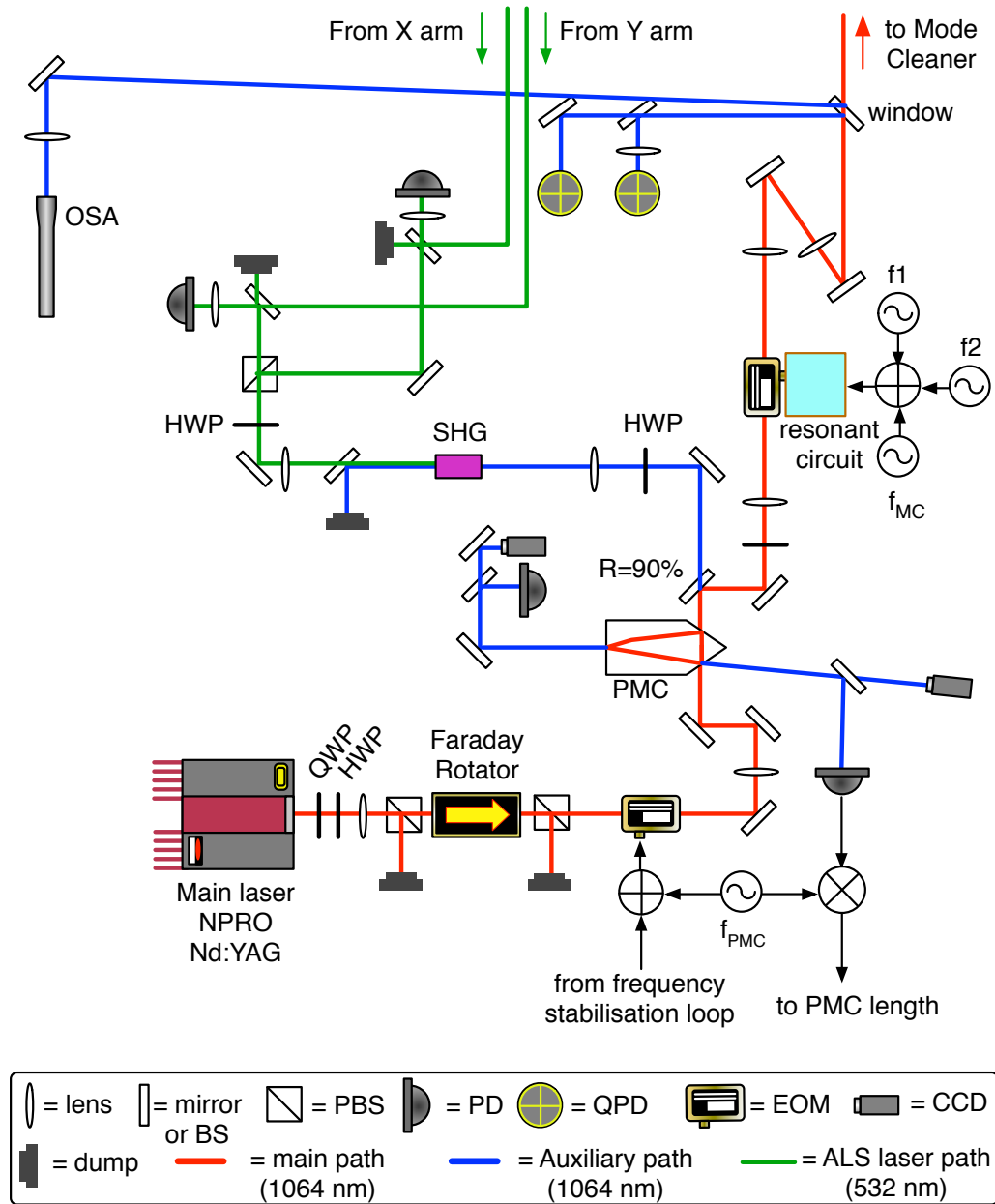


Figure 4.4: Schematic of the optical layout for the input optics.

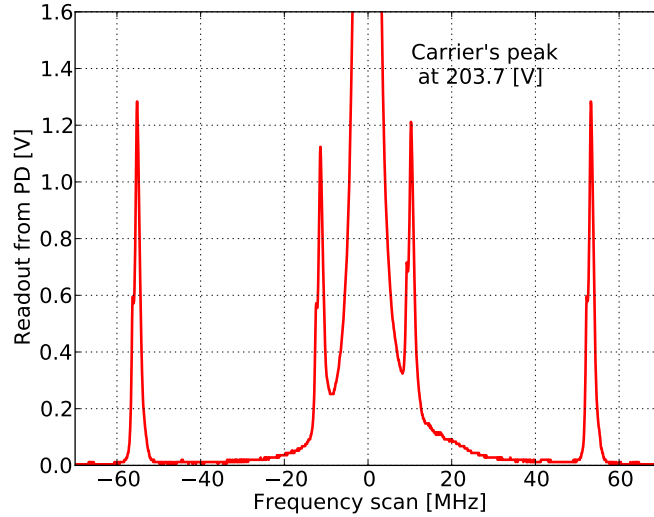


Figure 4.5: Spectrum of the incident field, measured by an optical spectrum analyzer. The highest peak at the center represents the carrier field. The peaks at  $\pm 11$  MHz is the upper and lower sidebands of  $f_1$ . The peaks at  $\pm 55$  MHz is the upper and lower sidebands of  $f_2$ .

### 4.3.2 Pre-Mode Cleaner

The main laser light is spatially filtered by a  $\sim 20$  cm ring cavity, called pre-mode cleaner (PMC), with a  $\sim 2$  MHz bandwidth that provides passive filtering of the laser noise at radio frequencies (RFs).

The PMC is a triangular optical cavity in which the mirrors are rigidly supported by a monolithic structure. The triangular configuration is chosen so that the reflected light doesn't overwrap the same optical trace as that for the incident beam. Hence it avoids installing an additional optical isolator.

To make the PMC fully functional, the PMC length needs to be locked to the PSL frequency. So for the reason, an RF photo detector (RFPD) and additional EOM are placed to enable the standard Pound-Drever-Hall (PDH) sensing. The reflected light is delivered to the RFPD. Then the signal from the RFPD is demodulated and feedback to the length. One of the mirrors, attached on the end of the cavity, has an piezoelectric actuator attached on its back surface such that is can control the length.

### 4.3.3 Electro-Optic Phase Modulator

In order to control the DRFPMI, phase modulations at two different frequencies are introduced to the main laser field. Additionally one more phase modulation is added in order to extract the signals associated with the MC. The modulation frequencies are summarized in table 4.1.

The two modulation frequencies for sensing the main interferometer were chosen to be integer multiple of MC's free spectral range (FSR), such that the sidebands are maximally transmitted through the MC. On the other hand the modulation frequency for the MC sensing was chosen in such a way that the sideband doesn't go through the MC.

The three phase modulation sidebands are efficiently imposed by using a resonant circuit which is attached to the electro-optic modulator (EOM). The circuit is explained in detail in appendix B.

The modulation depths are monitored with an optical spectrum analyzer (OSA). Figure 4.5 shows the measured frequency scan of the incident field which propagates toward the MC. The modulation depth can be estimated from the peak heights obtained by the scan measurement. The depth can be estimated from the following equation,

$$\Gamma \approx \sqrt{\frac{4V_c/V_s}{1 + 2V_c/V_s}}, \quad (4.1)$$

where  $V_c$  and  $V_s$  are respectively the peak height of the carrier and sidebands, measured by the OSA. The measured depths are also summarized in table 4.1.

symbol	description	value
$f_1$	Modulation frequency for the 1st sideband	11065910 Hz
$f_2$	Modulation frequency for the 2nd sideband	55329950 Hz
$f_{MC}$	Modulation frequency for MC sensing	22131820 Hz
$\Gamma_1$	Modulation depth at $f_1$	0.136 rad
$\Gamma_2$	Modulation depth at $f_2$	0.157 rad

Table 4.1: Quantities for the phase modulations.

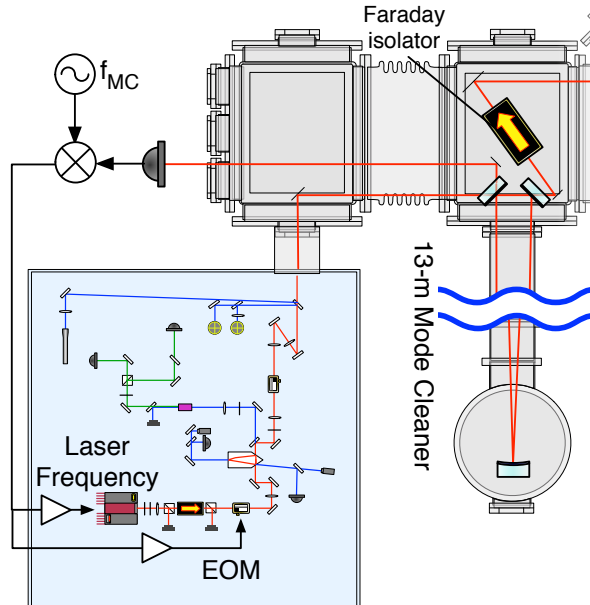


Figure 4.6: Setup for frequency stabilisation of the main laser. The laser frequency is locked to the length of the mode cleaner.

#### 4.3.4 13-meter Mode Cleaner

The PSL frequency is locked to an in-vacuum, suspended, critically-coupled, triangular mode cleaner (MC) cavity, which conditions the beam by suppressing excess frequency noise and rejecting higher-order spatial modes. The baseline length of the MC cavity is 13 m.

The PSL frequency is locked to the MC length and stabilised with the standard PDH technique as shown in figure 4.6. The PDH signal is fed back to a compound actuator consisting of three stages — temperature of the laser crystal, the laser cavity and the EOM (which is the one close to the PSL), to achieve a high-bandwidth control. Figure 4.7 shows the actual open loop transfer function of the stabilisation loop. The control bandwidth of about 130 kHz is achieved.

#### 4.3.5 Monitors

It is always useful to have a number of monitors to continuously check and diagnose the system. There are two quadrant photo detectors (QPDs) to

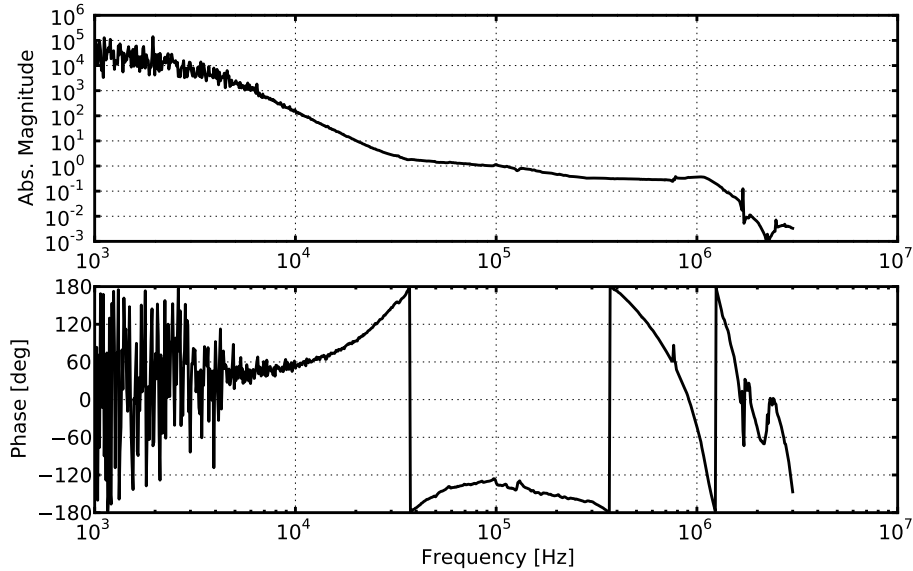


Figure 4.7: Bode plot of the open loop transfer function of the PSL frequency stabilisation loop, measured. The unity gain frequency is 130 kHz.

monitor the spatial beam jitter in the main laser. A small fraction of the main laser is picked off by a window just before it goes into the vacuum chamber as shown in figure 4.4. Additionally there is an OSA to monitor the depth of the modulation sidebands.

## 4.4 Core Optics

All of the core optics, including the MC mirrors, beam splitter (BS), power recycling mirror (PRM), signal recycling mirror (SRM), input test masses (ITMs) and end test masses (ETMs), has a diameter of 3 inch. Each of them are wedged by about 2 degree to prevent from an etalon effect caused by a multiple-reflection between the two surfaces. To perform the ALS experiment, the mirrors in the arm cavities are coated as dichroic mirrors. The high-reflective coatings for the rest of them are designed only for a wavelength of 1064 nm, providing a low reflectivity at 532 nm. As an example, a picture of SRM is shown in figure 4.8. One can see that it seems transparent

## CHAPTER 4. THE 40-METER PROTOTYPE INTERFEROMETER

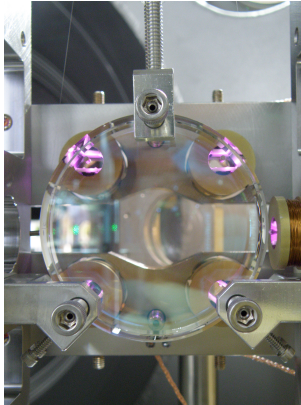


Figure 4.8: Picture of one of the core optics (SRM). The picture is taken from the front surface (high-reflective surface) of the mirror. The thin wire can be barely seen in the upper left side of the picture. The purple color corresponds to infrared light — it indicates that the OSEMs shine at infrared.

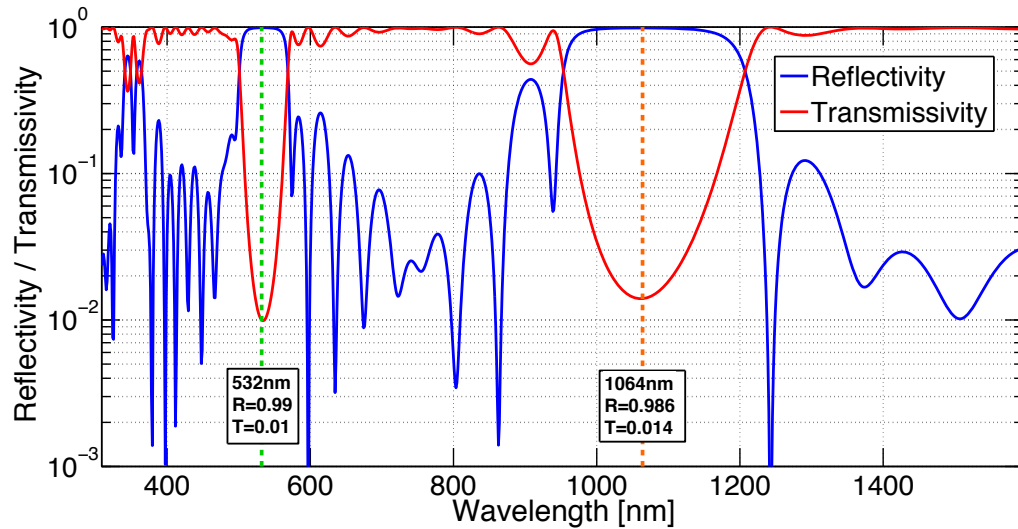


Figure 4.9: Spectral reflectivity and transmissivity of one of the dichroic cavity mirrors.

## 4.5. PHOTO DETECTION SYSTEM

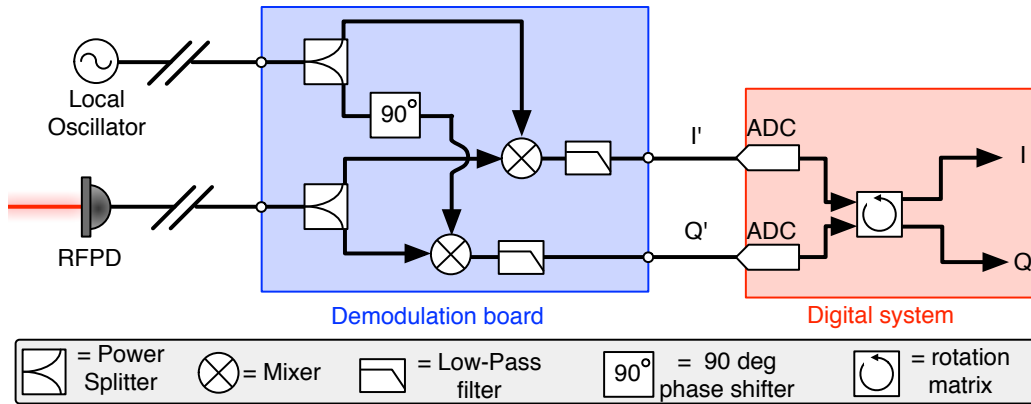


Figure 4.10: Block diagram of the demodulation system.

at the visible wavelengths.

### 4.4.1 Dichroic Mirror Coatings

The mirrors forming the arm FP cavities have custom coatings to provide reflectivity at both 1064 and 532 nm. Figure 4.9 shows the calculated coating reflectivity as a function of wavelength for the ITM (the ETM shows a similar profile). The layer structure is a particular aperiodic design chosen to minimize the influence of various types of thermal noise on the reflected phase of the laser field [36].

## 4.5 Photo Detection System

The photo detection system is a key for controlling the interferometer. The system can be broken into two subsystems — the PDs and demodulation system.

### 4.5.1 Photo Detectors

#### Radio Frequency Photo Detectors

Radio Frequency Photo Detectors (RFPDs) are the ones sensitive to light at RFs. A major use is detection of the RF sidebands in order to sense

## CHAPTER 4. THE 40-METER PROTOTYPE INTERFEROMETER

---

the lengths of the interferometer. Generally a laser field which exists from the interferometer contains a number of sidebands, and therefore observing the power produces a signal oscillating at some particular frequencies as explained in section 2.3.4. There are also a few broadband RFPDs, which are used for detecting the fields, such as the beat-note of two green light (see section 5.1).

Those, made for detection of the RF sidebands, are typically designed such that they outputs signal at a selected frequency. Usually the photo diode of the RFPDs is equipped with an additional resonant circuit, so that it can get rid of unnecessary frequencies before the current goes to a pre-amplifier, which would be saturated if all the frequency components come in. The location of all the installed RFPDs are described in appendix A.

### DC Photo Detectors

DC photo detectors (DCPDs) are the ones sensitive to the audio frequency signals, typically up to 100 kHz. The purpose of them is to monitor the intra-cavity power, the reflected power and so forth. They are useful in the sense that they can give information of the interferometric state rather than the nonlinear length signals. Moreover they can be a part of the length sensor (see section 3.2.4).

### 4.5.2 Demodulation System

The demodulation system consists of two main parts as shown in figure 4.10. One is the demodulation board and the other is the digital phase rotator.

#### Demodulation Boards

The demodulation board is an analog circuit which demodulates the RF signals delivered from an RFPD. There are two inputs on the board. One of them takes the monochromatic RF signal from a local oscillator and the other is for the signals from an RFPD. The local oscillator signal is split in two branches and the phase of one of them is rotated by 90 degree for the quadrature-phase (Q-phase) demodulation (see section 2.3). Similarly to the local oscillator signal, the RFPD signal is also split to two branches and each of them is demodulated as shown in figure 4.10. Then two demodulated signals are produced and then low-passed in order to remove the higher

harmonics that are generated at the mixers.

### Digital Phase Rotator

The digital phase rotator enables us to reconstruct the desired in-phase (I-phase) and Q-phase signals by rotating the demodulation phase by an arbitrary amount.

Generally the phase relation between the signal of a local oscillator and that of an RFPD can be off from the desired value. This phase mis-match can be corrected in the analog domain by adjusting the cable lengths but it needs to be done carefully. An alternative and straightforward approach is to employ a digital signal processor. As shown in figure 4.10, a digital system can provide a numerical phase rotator, which correct the demodulation phase.

Raw I and Q signals with a certain demodulation phase (i.e. a phase difference from the true I and Q demodulation) can be, according to equation (2.44), expressed by,

$$V_{\text{raw}}^{(I)} = \eta \text{Re} [x_{\text{ifo},k} E_k (x_{\text{ifo},k+1} E_{k+1})^* e^{i\phi_{\text{dem}}}], \quad (4.2)$$

$$V_{\text{raw}}^{(Q)} = \eta \text{Im} [x_{\text{ifo},k} E_k (x_{\text{ifo},k+1} E_{k+1})^* e^{i\phi_{\text{dem}}}], \quad (4.3)$$

where  $V_{\text{raw}}$  denotes the direct outputs from the demodulation board, and  $\phi_{\text{dem}}$  is the demodulation phase. In order to reproduce the ideal I and Q phase signals, one can simply apply a rotation matrix,

$$\begin{pmatrix} V^{(I)} \\ V^{(Q)} \end{pmatrix} = \begin{pmatrix} \cos \phi_{\text{dem}} & -\sin \phi_{\text{dem}} \\ \sin \phi_{\text{dem}} & \cos \phi_{\text{dem}} \end{pmatrix} \begin{pmatrix} V_{\text{raw}}^{(I)} \\ V_{\text{raw}}^{(Q)} \end{pmatrix}. \quad (4.4)$$

This operation is realized by the digital realtime processor.

## 4.6 Digital Control System

---

The number of active control loops is usually numerous in the modern GW interferometer (more than 100 loops). To control such a large number of loops, a digital control system is necessary. Moreover automation of some particular procedures, which must be performed routinely and frequently, should be done with the digital system in order to maintain the repeatability of the experimental conditions as well as the reliability in a systematic manner.

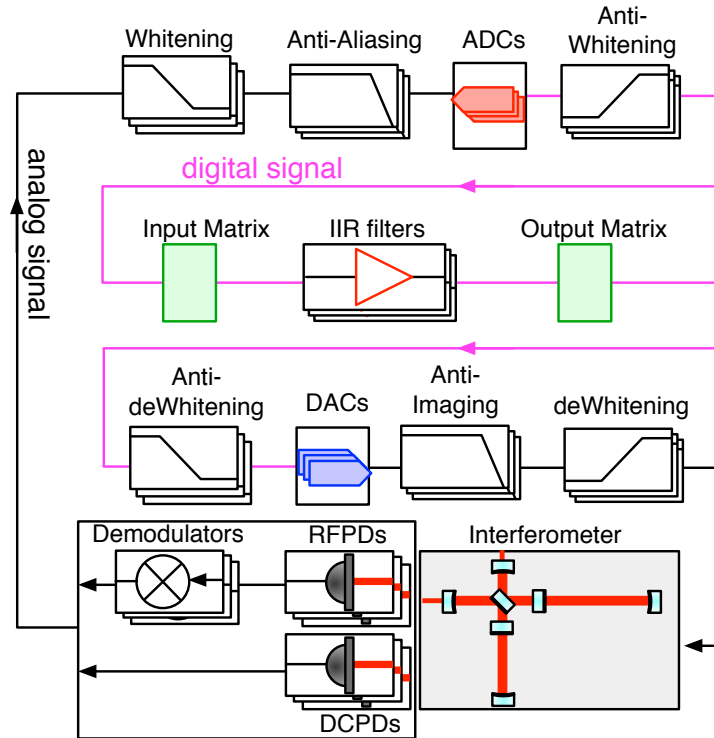


Figure 4.11: Block diagram of the digital realtime control, which controls the interferometer.

### 4.6.1 Realtime Signal Processing

Realtime signal processing is performed by a number of realtime OS machines. The realtime OS is an customized OS, which is specialized for high-speed signal processing and data communication. They control the interferometric states by taking digitized signals through Analog-to-Digital converters (ADCs), passing them to the signal processors and outputting the signals through Digital-to-Analog converters (DACs) to correct the interferometric state. In the prototype facility, five Gentoo Linux machines, customized for real time processing, are installed.

One realtime module consists of a Gentoo Linux machine and a PCIe extension board, in which a timing system, ADC and DAC cards are mounted. To achieve the global control of the interferometer, these machines are connected through the optical fiber links which provide a fast communication

over shared network memories.

### 4.6.2 Digital Control of the Interferometer

With the aid of the realtime OSs, the interferometer can be globally controlled. Figure 4.11 shows a typical flow of the signals processed by a realtime signal processor for the global control of the interferometer.

A typical signal flow is as follows. Signals, derived from a number of PDs, are sent to the ADCs and then digitized. Generally the raw signal doesn't uniquely represent a certain DOF. Therefore a desired DOF is reconstructed by a matrix, called input matrix. Then the signals are passed to the processor in which a number of Infinite Impulse Response (IIR) filters are applied and also offsets or some conditionings can be applied. After being processed, the signals are sent to the output matrix to convert the basis from the physical DOFs to the actual actuation points. The DACs produce the analog signals and they are feedback to the actuation points of the interferometer (e.g. coil magnet actuators).

A great flexibility is that the internal variables, such as the coefficients of the IIR filters and amount of the offsets, are controllable in a quasi-realtime way. The EPICS (Experimental Physics and Industrial Control System) system is introduced and communicates with the real time system at 64 Hz for this purpose. Therefore a user can change the variables from an interface computer by simply rewriting the EPICS variables. Consequently this function enables us to program various control sequences with a scripting language.

Although the digital system is a powerful tool, one always needs to introduce some signal conditioning filters, such as whitening, dewhitening, anti-aliasing and anti-imaging filters, in order to make the system less sensitive to noises from the ADCs and DACs. A drawback is that the bandwidth of the digital control can not be higher than the Nyquist frequency, which is at 8 kHz in the case of the 40-meter prototype. In fact the fastest bandwidth is practically lower than the Nyquist frequency due to a relatively large delay in the whole process chain.

## CHAPTER 4. THE 40-METER PROTOTYPE INTERFEROMETER

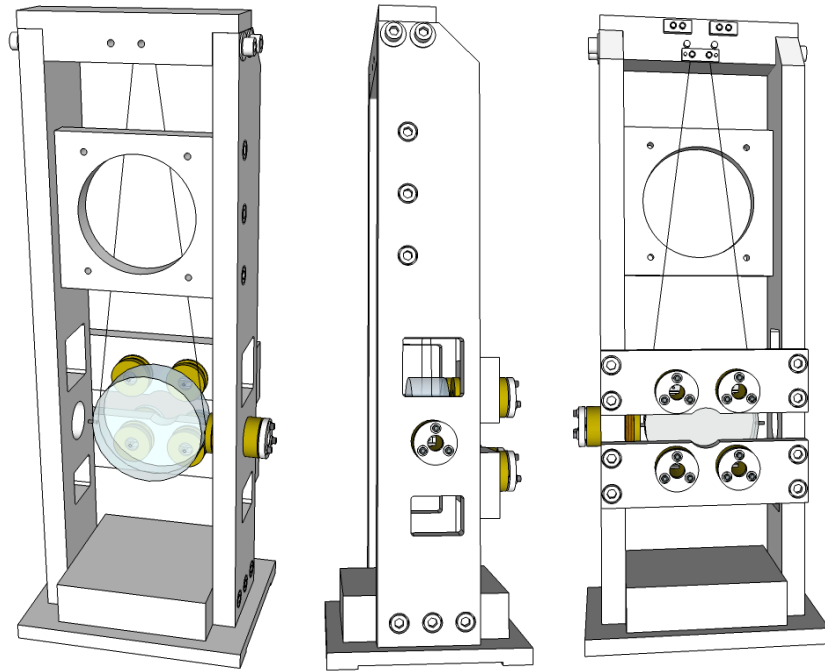


Figure 4.12: Schematic view of the small optic suspension. (Left) Front view. (Middle) Side view. (Right) Rear view.

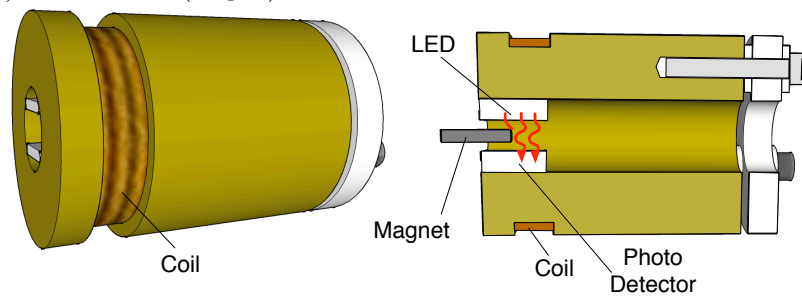


Figure 4.13: Schematic view of the OSEM. (Left) side view (Right) section view. The magnet is attached to the back surface of a suspended mirror, which is not shown in this schematic.

### 4.7 Suspensions and Their Controls

---

#### 4.7.1 The Small Optic Suspension

All of the mirrors in the vacuum are suspended from a rigid stainless steel structure, via a single-loop wire as depicted in figure 4.12. Both ends of the wire are clumped at the top of the structure. The height of the suspension cage is about 40 cm and its base size is about  $13 \times 16$  cm.

This suspension design is a standard known as small optic suspension among the LIGO laboratory. The effective length of the wire is about 25 cm and this gives a resonant frequency of about 1 Hz for the pendulum mode, which is a oscillation mode of the mirror along the longitudinal direction with respect to the beam axis.

Usually the suspensions are designed to have a high quality value (Q-value). This means that the mirror would keep oscillating unless a damping system is applied. In fact the motion of the mirrors are locally damped with the aid of the digital control system.

#### 4.7.2 Local Controls

##### OSEMs

The OSEM is a module which acts as both a sensor and actuator. A schematic view of the OSEM is shown in figure 4.13. It is made of a cylindrical structure with a coil wounded around it. A pair of an LED and its receiver is installed in the hole. Therefore an OSEM can readout the longitudinal motion of a magnet which is attached to the suspended mirror. In addition, it can actuate the mirror by introducing currents through the coil. In a single suspension five OSEMs are installed — four of them are at the back side of the mirror and one at the side as shown in figure 4.12.

The idea of the active damping with the OSEMs is to suppress the motion only at around the mechanical resonances (typically  $f \sim 1$  Hz for the SOS) such that the local damping doesn't inject control noises in the observational frequency band. By linearly combining the five signals from the OSEMs, one can reconstruct the DOF signals that are the angular motions and longitudinal motion through the input matrix [80]. Then the signals are filtered, passed to the output matrix , and then drive the current through the coil of the OSEMs. This signal processing is done by the digital control system in

## CHAPTER 4. THE 40-METER PROTOTYPE INTERFEROMETER

---

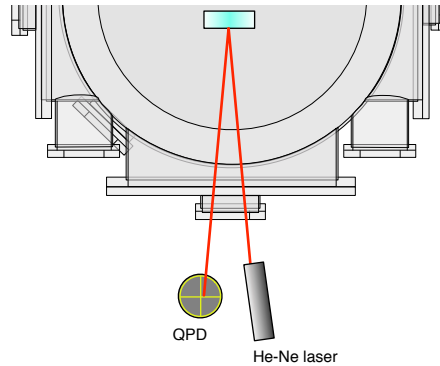


Figure 4.14: Optical lever setup.

the same fashion as that of the global control described in section 4.6.2.

### Optical Levers

There is another type of sensor called optical lever. The optical lever also senses the angular wobbling of the suspended mirrors as the OSEMs do. Figure 4.14 shows a typical setup for the optical lever. The optical lever is formed by a He-Ne laser, the suspended mirror and a QPD. The idea is that as the mirror wobbles in its angle, the reflected He-Ne laser also spatially wobbles, and hence a QPD can readout the angular motion. The feedback signals generated from the optical lever is digitally added to the OSEM damping signals and it damps the mechanical resonances.

## 4.8 Second-Harmonic Generation

---

In order to perform the multi-color interferometry, second-harmonic generation (SHG) is necessary as explained in section 3.4. In total, three SHG crystals made of periodically poled  $\text{KTiOPO}_4$  (PPKTP) with a length of 30 mm were installed. Two of them are placed at the end tables to frequency-double the AUX lasers and the last one is placed at the PSL optical table to frequency-double a sample of the PSL light.

---

## 4.8. SECOND-HARMONIC GENERATION

---

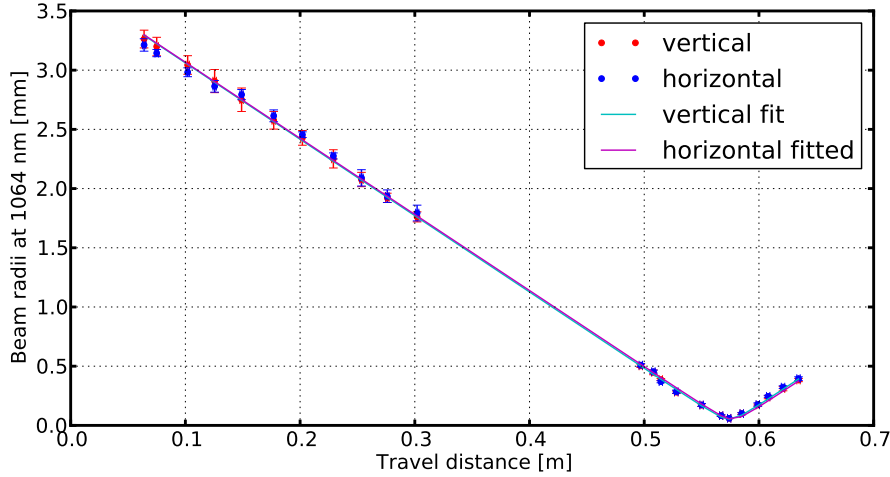


Figure 4.15: The beam radii of the incident beam ( $\lambda = 1064$  nm) on one of the SHG crystals.

### 4.8.1 The Setup

A PPKTP crystal ( $1 \times 1 \times 30$  mm PPKTP from Raicol Crystals Ltd.) is housed by an oven (Covesion Ltd. PV40) which is equipped with a resistive heater and temperature sensor to enable temperature stabilisation for an efficient and stable SHG. The heater is driven by a dedicated controller (Thorlabs Inc. TC200), which has an interface for the oven. With the controller the temperature of the crystal is controlled based on the PID control.

### 4.8.2 Adjustments

#### Waist Size of the Fundamental Field

To exploit the second-harmonic power efficiently, the fundamental laser beam should be appropriately focused on to the crystal. According to section 2.6.5, a PPKTP crystal of 30 mm length requires a beam with a waist radius of  $\sim 50$   $\mu\text{m}$ . Figure 4.15 shows a measured beam size of the fundamental beam for the crystal on the PSL table as a function of the travel distance of the light. The measurement was done without installing the crystal.

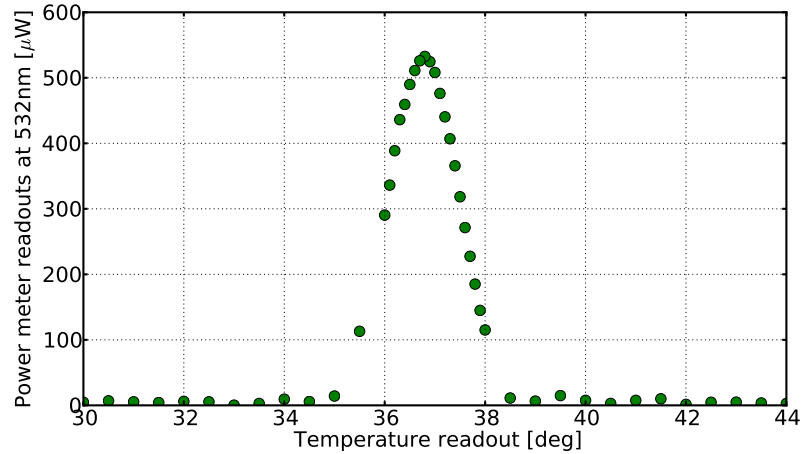


Figure 4.16: Second harmonic power as a function of temperature, measured.

By shifting the position of the associated lenses, the waist size was adjusted to be  $52 \mu\text{m}$  for both the vertical and horizontal beam profiles. This reasonably satisfies the required beam size. Once the waist size is appropriately adjusted, the crystal can be installed with its center placed at the focal point. The same adjustment was performed for the ones installed at the end tables.

### Temperature Optimization

The temperature of each SHG crystal is adjusted to the value where the maximum efficiency is observed. Figure 4.16 shows a temperature scan of the second-harmonic power for the SHG crystal installed on the PSL table. The linewidth was found to be about 1 degree with a center temperature of  $\sim 37 \text{ }^\circ\text{C}$ . Once the optimum temperature was found, the PID control was applied to keep the same temperature.

## 4.9 Auxiliary Laser Setup

---

An auxiliary (AUX) laser and its associated optics were installed at each end table of the arm cavities. The function of this setup is to deliver a frequency-doubled Nd:YAG laser toward the interferometer vertex by stably locking

## 4.9. AUXILIARY LASER SETUP

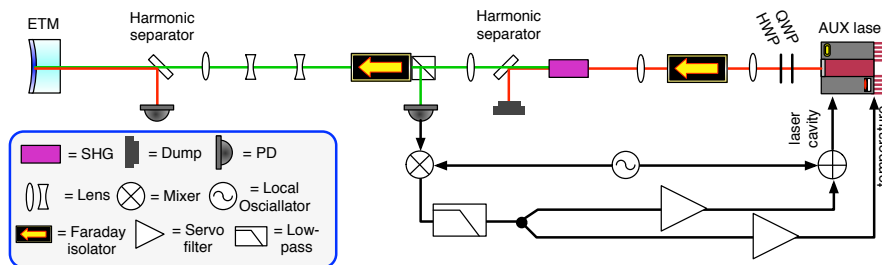


Figure 4.17: Schematic of the auxiliary laser setup.

the frequency of the laser to the arm length.

### 4.9.1 Optical Layout

Since the setup is essentially identical for both  $x$  and  $y$  setups, only the setup for the  $y$  arm is explained here. Figure 4.17 shows a schematic view of the optical layout and associated electronics. The AUX laser propagates through an Faraday isolator (OFR/Thorlabs Inc. IO-5-1064-HP) to prevent from the back stream of the laser. Then a lens focuses the beam on to the SHG crystal, such that the beam is appropriately focused to the crystal. After the crystal a harmonic separator is placed to separate the second-harmonic field from the residual fundamental field. Then another Faraday isolator (OFR/Thorlabs Inc. IO-5-532-MP) is placed again for enabling to pick off the reflected light from the cavity. Finally the beam propagates through a set of lenses which are for mode-matching the beam to the spatial eigen mode of the arm cavity.

### 4.9.2 Phase Modulation

The phase modulation sideband is imposed on the AUX laser field by directly modulating the laser cavity by the local oscillator (Stanford Research DS345). In this case the fundamental field of the AUX laser can be expressed by

$$E^{(\omega)} = A_0 \exp(i\omega_{\text{AUX}}t + i\Gamma \sin \omega_m t), \quad (4.5)$$

where  $\omega_{\text{AUX}}$  is the angular frequency of the AUX laser,  $\omega_m$  is the modulation frequency and  $\Gamma$  denotes the modulation depth.

Then this field propagates through the SHG crystal. According to equation (2.67), the second-harmonic field is generated by squaring the funda-

## CHAPTER 4. THE 40-METER PROTOTYPE INTERFEROMETER

---

mental field. Therefore the frequency-doubled field can be expressed by,

$$E^{(2\omega)} \propto (E^{(\omega)})^2 \quad (4.6)$$

$$= A_0^2 \exp(2i\omega_{\text{AUX}}t + 2i\Gamma \sin \omega_m t). \quad (4.7)$$

Therefore the resultant second-harmonic field is phase-modulated at the same frequency of  $\omega_m$  with twice deeper depth of  $2\Gamma$ . This ensures that the standard PDH scheme can be still applied by demodulating the reflected power at  $\omega_m$ . For the PD, a silicone photo detector (Thorlabs Inc. PDA36A) is used and the demodulation is done by a mixer (Mini Circuit ZAD-8).

The modulation frequency was carefully chosen such that the residual amplitude modulation (RAM) depth is small enough compared with that for the phase modulation. The effect of the RAM is that it changes the operating point of the demodulated signal by adding an extra amount of the offset.

For the  $y$  arm AUX laser, the modulation frequency is chosen to be at 217820 Hz where the phase-modulation-to-amplitude-modulation ratio of  $\Gamma_m/\Gamma_a \sim 10^5$  is achieved. The modulation frequency of the  $x$  arm AUX laser is chosen to be at 216075 Hz for the same reason.

### 4.9.3 The Frequency Locking

The frequency of the AUX laser is locked to the cavity length with the PDH scheme. The feedback signals is applied on the laser cavity as well as the temperature of the laser crystal. The control bandwidth of this frequency locking loop is 30 kHz for the  $y$  arm.

The idea of the compound actuator is as follows. The laser cavity actuation has a relatively small range — the  $y$  arm AUX laser has an actuator response of approximately 5 MHz/V. The arm cavity usually swings by approximately 1  $\mu\text{m}$ , corresponding to a frequency shift of 7 MHz for the AUX laser to follow it in a time scale of 1 sec. However in a longer time scale, it can fluctuate more than that. Therefore only feeding the signal back to the laser cavity may not be sufficient to stably track the displacement without saturation in the feedback signal which is limited by approximately  $\pm 10$  V. So for the reason the temperature feedback is added so that the offset in the laser cavity feedback path is offloaded to the temperature actuator, which has a much larger response of about 1 GHz/V. The temperature feedback takes care of the signals below approximately 0.1 Hz.

### 4.10 Summary of the Chapter

---

- The 40-meter prototype interferometer is the only one prototype for advanced LIGO. The goal is to demonstrate the length sensing and control and lock acquisition schemes that will be used in advanced LIGO.
- The optical configuration of the prototype interferometer is the same as that of advanced LIGO i.e. dual-recycled Fabry-Pérot Michelson interferometer.
- The interferometer can be globally controlled by the realtime digital control system. The suspensions are also controlled by the digital system and their control loops were tuned.
- The dichroic mirrors in the arms, second-harmonic generation systems and auxiliary laser setups were implemented in order to perform the multi-color interferometry.
- After the upgrade the interferometer became capable for tests of the multi-color interferometry.



# 5

## Demonstration of Arm Length Stabilisation

The primary motivation of the experiment described in this chapter is to demonstrate that the arm cavity length can be independently controlled by the multi-color technique to within a small fraction of the linewidth of the arm cavity at the primary laser frequency.

In section 5.1 the experimental arrangement is described. Section 5.2 explains the control sequence to achieve a smooth and repeatable control process. Section 5.3 shows a demonstration of a smooth length scan, which is one of the main function of the arm length stabilisation (ALS) scheme.

### 5.1 Experimental Arrangement

---

#### 5.1.1 Single Arm Fabry-Pérot Cavity

For this experiment just a single, suspended, 40-meter-long arm Fabry-Pérot (FP) cavity of the full interferometer is used. The rest of the interferometer optics are intentionally misaligned so as to not affect the measurements. The power of the main laser, called pre-stabilised laser (PSL) is adjusted to allow approximately 25 mW of 1064 nm laser light to be incident on the cavity under test.

Figure 5.1 shows a schematic diagram of the experimental setup. A 1064 nm beam (red in diagram) from the PSL is injected into the arm cavity through the input mirror (ITM) from the interferometer vertex. A second, 532 nm beam (green in diagram) from an auxiliary (AUX) laser is injected through the cavity end mirror (ETM). Whereas the PSL beam circulates

## CHAPTER 5. DEMONSTRATION OF ARM LENGTH STABILISATION

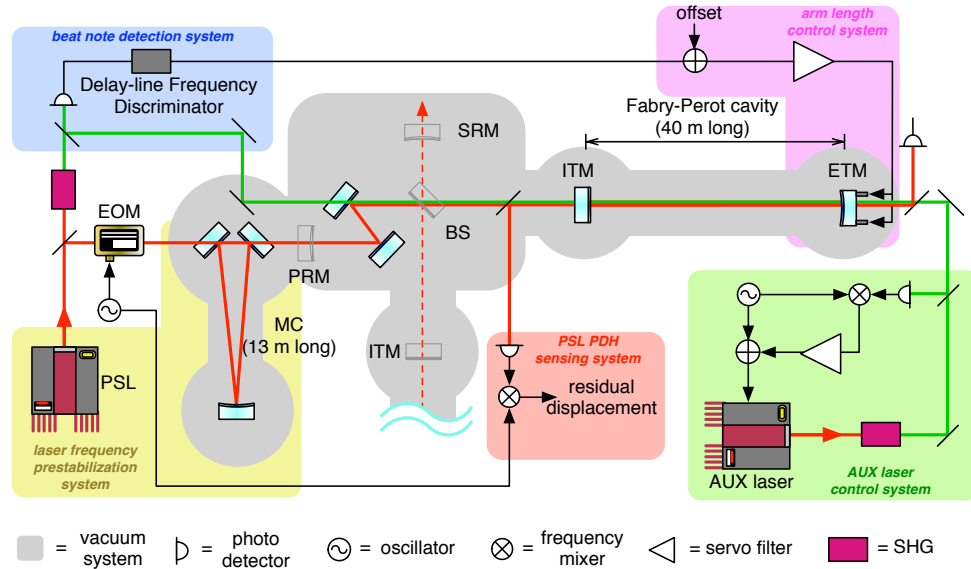


Figure 5.1: Experimental setup. Red lines indicate the path of the 1064 nm PSL beam, and green lines indicate the path of the 532 nm AUX beam. The colored regions correspond to logical sections of the control and readout, described in more detail in Section 6.1. Optics in shadow are part of the larger interferometer not used in this experiment.

through the full interferometer under normal operating conditions, the AUX laser beam resonates only in the single arm cavity and is extracted through one of the folding mirrors in the recycling cavity. The motion of each cavity mirror is locally damped by five OSEMs and optical lever (see section 4.7).

The cavity mirrors are dichroic and highly reflective at both wavelengths as explained in section 4.4.1. For the 1064 nm PSL beam, the cavity is overcoupled and reflects most of the light back towards the interferometer vertex. For the 532 nm beam the cavity has a much higher transmissivity and some of the light is transmitted through the cavity at the ITM, through the interferometer vertex and extracted from the vacuum. The mirror and cavity properties for both wavelengths are shown in table 5.1.

The AUX beam transmits through the ITM and is extracted from the vacuum system. The extracted AUX beam is used in a heterodyne mea-

## 5.1. EXPERIMENTAL ARRANGEMENT

cavity property	symbol	1064 nm	532 nm
ITM power transmissivity	$T_i$	0.0138	0.0458
ETM power transmissivity	$T_e$	$1.37 \times 10^{-5}$	0.0109
power trans. (resonance)	$T_c$	$3.92 \times 10^{-3}$	0.616
power trans. (anti-resonance)	$T_c^\dagger$	$4.77 \times 10^{-8}$	$1.29 \times 10^{-4}$
finesse	$\mathcal{F}$	450	109
cavity pole frequency	$f_c$	4.40 kHz	18.3 kHz
cavity length	$L$	37.8 m	
free spectral range	$f_{\text{FSR}}$	3.97 MHz	

Table 5.1: Cavity properties of the arm cavity, at 1064 nm as seen from the vertex, and 532 nm as seen from the cavity end.

surement with a frequency-doubled sample of the PSL beam. The frequency of the beat-note between the AUX laser and the frequency-doubled PSL is measured by the delay-line frequency discriminator (DFD) (see section 5.1.3). The outputs from DFD are the primary error signal for the cavity control. They are digitized and a control signal is generated with a digital control system.

The final steady-state control used during the measurement is described in detail in section 6.1. A Pound-Drever-Hall (PDH) error signal derived from the PSL beam reflected off of the ITM provides an out-of-loop measure of the residual cavity displacement. Note that this sensor employs a modulation frequency of 11 MHz (see section 4.3.3).

### 5.1.2 AUX Light Source and Frequency Doubling

The AUX beam comes from a frequency-doubled 700 mW JDSU NPRO-126N. The frequency doubling is achieved via second-harmonic generation in a periodically poled KTP (PPKTP) crystal. The conversion efficiency is  $\sim 1\%/W$ , and with other input losses we end up with 1.2 mW of 532 nm light incident on the ETM. A more detailed optical layout can be found in section 4.9.

## CHAPTER 5. DEMONSTRATION OF ARM LENGTH STABILISATION

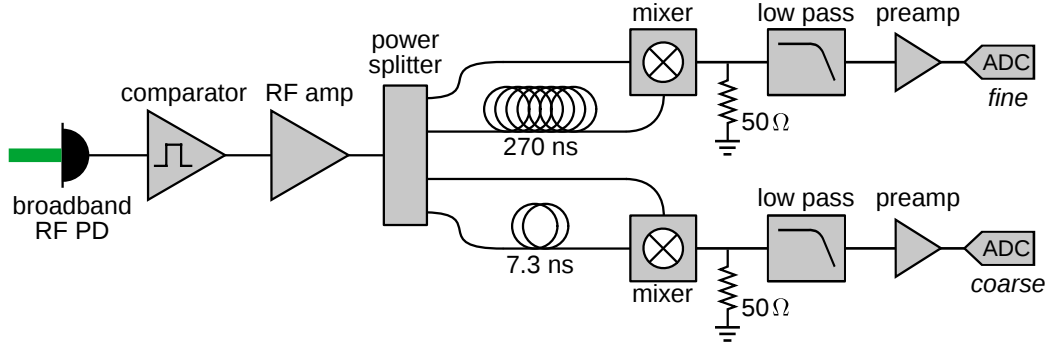


Figure 5.2: Delay-line frequency discriminator. Components used: comparator: Analog Devices AD9696; RF amplifier: Mini-Circuits ZHL-1A; power-splitter: Mini-Circuits ZBSC-413+; delay line cables: RG-58 C/U; mixer: Mini-Circuits ZP-3+; low-pass filters: Mini-Circuits BLP-1.9; pre-amplifier: Stanford Research SR560.

### 5.1.3 Delay-line Frequency Discriminator

The delay-line frequency discriminator (DFD), which is used to measure the frequency of the beat-note between the PSL and AUX beams, works by mixing an input radio-frequency (RF) signal with a delayed version of itself. Figure 5.2 shows a schematic of the DFD circuit. For a given delay in the delay line  $\tau$ , the mixer output voltage is a periodic function of the input frequency  $f$ . The signal can be expressed by

$$V = \zeta \cos(2\pi f_{\text{beat}}\tau), \quad (5.1)$$

where  $\zeta$  is the amplitude of the resultant signal and we neglected a high frequency term oscillating at a frequency of  $2f_{\text{beat}}$  because this signal is filtered out by a low-pass filter.

When the beat frequency is in the linear range where  $f_{\text{beat}} \sim 1/4\tau$ , the output is directly proportional to the input frequency,

$$V \approx 2\pi\zeta f_{\text{beat}}\tau. \quad (5.2)$$

The signal from a broadband RF photodetector first passes through a comparator that turns the signal into a square wave. This helps reduce noise associated with small amplitude fluctuations of the input signal. Thus it

---

## 5.2. AUTOMATION OF THE CONTROL SEQUENCE

---

forces the amplitude  $\zeta$  to be a constant in equations (5.1) and (5.2). This signal is amplified and split into two discriminator paths: a *coarse* path with a delay of 7.3 ns and frequency range of 34 MHz, and a *fine* path with a delay of 270 ns and a range of 3.6 MHz. The mixer outputs are filtered, resulting in signals given in equation (5.2), then digitized and used as error signals for the cavity length control servo. The coarse path, which has a larger bandwidth, is used during lock acquisition (see section 3.4.5), whereas the lower-noise fine path is used to achieve best performance in the steady state.

In order to confine the cavity length to within the linewidth of the PSL a residual fluctuation level of 10 pm in root mean square (RMS) must be achieved. This means that the frequency noise of the fine path needs to be less than  $7.4 \text{ Hz}/\sqrt{\text{Hz}}$  in the control bandwidth. The noise of the two paths are currently limited by the active readout electronics at an estimated level of  $2.0 \text{ Hz}/\sqrt{\text{Hz}}$  and  $0.1 \text{ Hz}/\sqrt{\text{Hz}}$  for the coarse and fine paths respectively. They therefore reasonably meet the required frequency stability.

A delay-line design was used, rather than a phase-locked loop (PLL) design [81] because the frequency range of DFDs are relatively easy to tune and can be adjusted to give a large frequency range (e.g. the coarse channel). DFDs also don't require any active feedback loops, which complicate PLLs. Alternatively, a combination of a large range DFD and a smaller range PLL could be a possible solution depending on the required frequency range and noise.

## 5.2 Automation of the Control Sequence

---

### 5.2.1 Digital Control

The ALS is performed with the aid of the digital control system. The use of the digital system enables us to program a sequence to stabilise the arm cavity.

Figure 5.3 shows a schematic diagram of the active control with the digital system. The beat-note signals from the coarse and fine sensors are digitized and then blended by a pair of two variable gain stages. Then an offset is introduced and it allows one to shift the operating point for scanning the arm length. The signals are passed to a servo Infinite Impulse Response (IIR) filter, which is designed to achieve a stable control. The signals passes

## CHAPTER 5. DEMONSTRATION OF ARM LENGTH STABILISATION

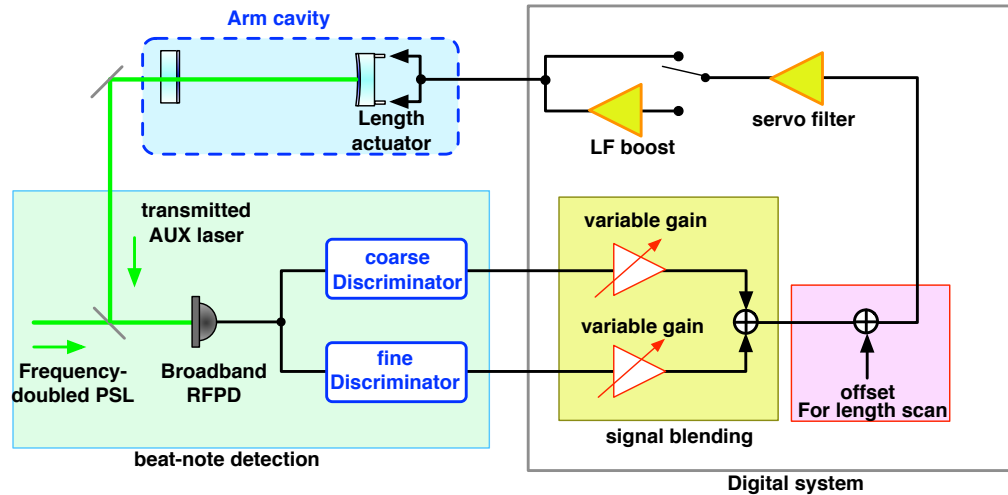


Figure 5.3: Schematic of the arm length stabilisation loop with the realtime digital control system.

through the low-frequency boost stage to further stabilise the length. The low-frequency boost is initially bypassed, so that acquisition can be smooth. Finally the signals are fed back to the coil magnet actuators, which are formed by the combination of the OSEMs (see section 4.7.2) and the magnets attached on the ETM to correct the length.

### 5.2.2 The Control Sequence

Since the ALS scheme will be a part of the full lock progression, it must be automated so that anyone can perform the same progression in a systematic way. Moreover the ALS scheme requires a sequence because the stabilisation of the arm length doesn't mean the PSL laser is fully resonant. In fact the arm length needs to be sequentially brought to a desired point every time after the arm is stabilised.

Figure 5.4 shows the sequence, which was implemented, as a function of time. The desired operating point in this experiment is the resonance point for the main PSL. Thus the sequence ends when the cavity is fully on resonance, starting from the state where the cavity is uncontrolled with a displacement of about  $1 \mu\text{m}$  in RMS.

## 5.2. AUTOMATION OF THE CONTROL SEQUENCE

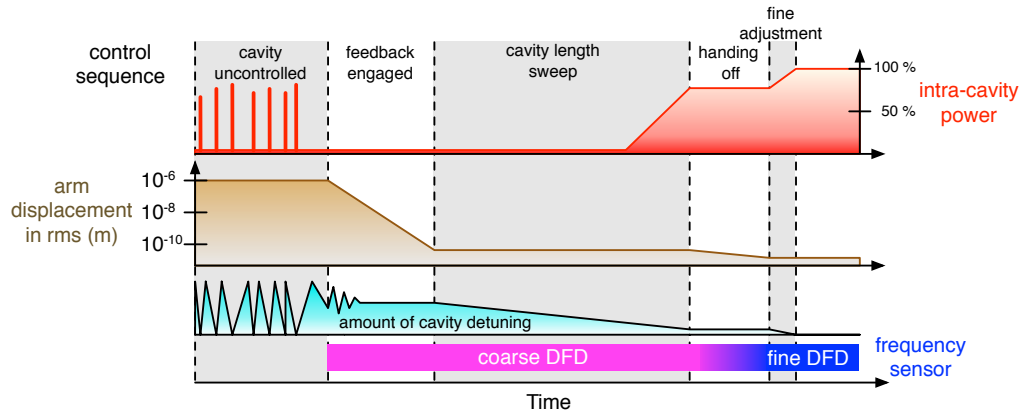


Figure 5.4: Sequence of the arm length control as a function of time. The intra-cavity power and detuning are for the 1064 nm PSL beam.

### 5.2.3 Automation

The control sequence shown in figure 5.4 was implemented with the aid of Python. The Python code edits some of the EPICS variables depending on the stage of the sequence and finally brings the cavity length to a resonance point. Figure 5.5 illustrates the flow chart of the automated sequence that is used for this experiment. The following paragraphs explain each step of the sequence in detail.

#### Initialization

At the very beginning of the sequence, the ground state is checked to confirm whether if the interferometer is in a healthy state or not. At this point the amount of the mirror motions and the amount of the transmitted PSL laser through the MC are checked. If any of them shows unusual values, the sequence quits to enable one to manually check the interferometer.

Additionally the beat-note needs to be also checked as a part of the ground check. The lasers could drift more than 100 MHz depending on the temperature of the laboratory. So for the reason if the beat-note is not found, one needs to change the temperature of the AUX laser to bring the beat-note within the observable frequency range. Changing the temperature unlocks the AUX loop, however, it quickly reverts because the control bandwidth is

## CHAPTER 5. DEMONSTRATION OF ARM LENGTH STABILISATION

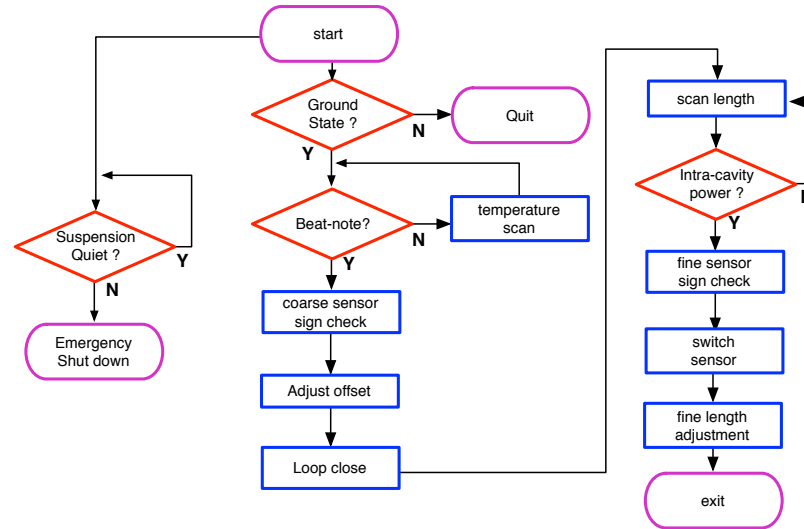


Figure 5.5: Flow chart of the control sequence.

fast. This procedure is still a manual operation at this time.

### Engagement of the Control and Length Scan

Once the beat-note becomes observable the sign of the coarse DFD signal is checked. This is because that the sign of the DFD signals can be different depending on whether the AUX laser has a higher frequency than the PSL frequency or vice versa. This process is done by exciting the arm length at 11 Hz, where seismic noise is moderately small and the mirror can be easily displaced by the coil magnet actuators, and by synchronously demodulating the DFD signal.

After the sign is adjusted properly, the offset is adjusted such that an impact on the arm length is lesser when the signals are being applied to the length. Then it starts feeding the signals back to the length with the gain gradually increasing. Once the gain reaches the nominal value, where the desired control bandwidth is achieved, a low-frequency boost is engaged to further suppress the displacement. Figure 5.6 shows a time series of the intra-cavity power and beat-note frequency. It is shown that the beat frequency becomes quiet as the ALS control is engaged.

Next, a scan of the arm length starts by introducing an offset on the DFD

## 5.2. AUTOMATION OF THE CONTROL SEQUENCE

---

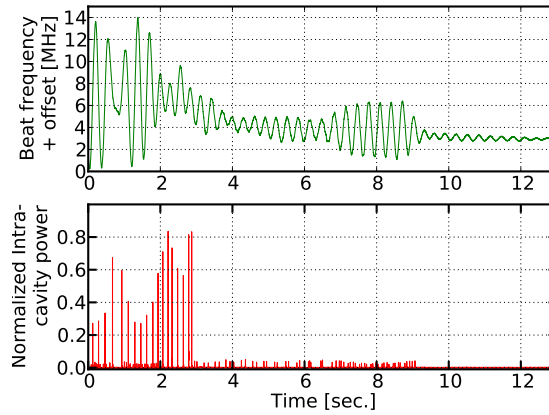


Figure 5.6: Acquisition of the arm length stabilisation servo in time series. The gain starts increasing at  $t = 2$  sec and the low-frequency boost is engaged at  $t = 9$  sec.

signal. It continues until the intra-cavity power exceeds a certain threshold value.

### Switching the Frequency Sensor

Once the intra-cavity reaches the threshold then the programmed code switches the frequency sensor from the coarse DFD to the fine one. At first it checks the sign of the fine DFD by exciting the length motion at 283 Hz, which is above the control bandwidth of the arm length stabilisation loop. Then the gains for the fine signal begins increasing while that for the coarse one decreases at the same time.

After the fine sensor is engaged, one can further tune the length more precisely so that the main laser fully resonates in the arm. This process can be done by intentionally modulating the cavity length at a certain frequency and demodulating the intra-cavity power at the same frequency. However the fine tuning is not yet fully implemented at this time.

### 5.3 Demonstration of the Length Tunability

---

The primary usefulness of the multi-color readout is that it enables us to precisely adjust the arm length and hold it at a desired value independently of the interferometric state of the rest of the interferometer as discussed in section 3.4.

Figure 5.7 shows a sweep of the cavity length feedback offset through the cavity resonance of the 1064 nm PSL beam. The figure demonstrates that the length detuning can be cleanly and smoothly brought to zero, at which point the 1064 nm beam is fully resonant in the cavity. The top plot is the amount of the detuning in terms of the beat frequency observed at the fine DFD output. The middle plot shows the 1064 nm intra-cavity power as it passes through resonance with the cavity. The bottom plot shows the PSL PDH error signal. The resultant residual displacement, measured by the PSL PDH signal when it is in the linear range, was found to be 23.5 pm. The residual displacement is further analyzed in the next chapter.

### 5.4 Discussions and Summary of the Chapter

---

#### 5.4.1 Discussions

In the automated sequence there was a step which needed a human approval. The step is the one which switches the frequency sensor from the coarse DFD to the fine one. The reason is that the fine DFD has a narrower linear range and the response becomes periodically quadratic due to the cosine response (5.1). Therefore depending on the beat frequency the fine sensor is occasionally in a quadratic regime when the arm cavity is brought to a resonance with the coarse sensor. This issue leads to the addition of the human approval process so that one can further bring the arm length to the neighboring resonance which can avoid being in the quadratic region.

To avoid the narrow range issue of the fine sensor, one possible solution is modification of the fine DFD circuits. In this solution we add some more electronics components to it such that it gives not only the ordinary I-phase demodulation signal but also the Q-phase demodulation signal. This can be done by inserting a 90 deg phase-shifter, power splitter and another mixer. In this case the I-signal will be a function of  $\cos(2\pi f_{\text{beat}}\tau)$ , while the Q-signal is  $\sin(2\pi f_{\text{beat}}\tau)$ . Once these two signals are digitized through the ADC,

## 5.4. DISCUSSIONS AND SUMMARY OF THE CHAPTER

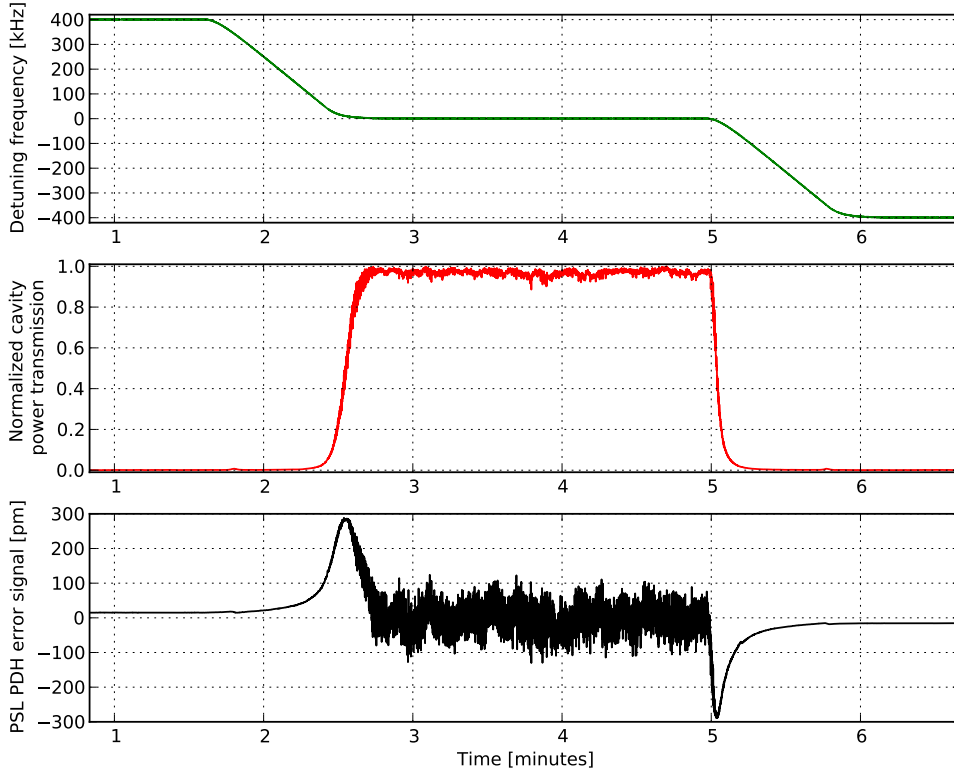


Figure 5.7: Sweep of cavity length control offset through the 1064 nm (PSL) resonance of the cavity. A detuning of 100 kHz corresponds to a cavity displacement of 6.7 nm.

one should be able to reconstruct the beat frequency  $f_{\text{beat}}$ , for example by applying  $\tan^{-1}(S_Q/S_I)$  where  $S_I$  and  $S_Q$  are the I- and Q-signals respectively. Therefore this modification will allow us to extract the beat frequency in a wider range without losing the sensitivity. In fact this circuit is currently being implemented in the 40-meter prototype.

### 5.4.2 Summary

- A demonstration of the multi-color interferometric technique has been performed in the Caltech 40-meter prototype.
- In the test one of the arm Fabry-Pérot cavities is used and its length

## CHAPTER 5. DEMONSTRATION OF ARM LENGTH STABILISATION

---

is controlled by feeding the signals back to the position of the end test mass.

- In order to cover a wide range of the beat frequency with a sufficiently high dynamic range, two delay-line frequency discriminators are installed, resulting in an effective dynamic range of  $34 \text{ MHz}/0.1 \text{ Hz} \sim 3 \times 10^8$ .
- The control process is automated as a sequence with a Python script. It automatically brings the cavity length to a point where the main  $1064 \text{ nm}$  beam fully resonates in the cavity.
- The cavity can be smoothly brought to a resonance point with a stability of  $23.5 \text{ pm}$  in root mean square.

# 6

## Modeling and Noise Analysis

In order to examine the test described in the previous chapter, a noise analysis is performed. In the analysis a linear control model is built. The model allows us to estimate the transfer function which determines the degree of the contribution of each noise source to the resultant displacement. Moreover once the model is built, it can be used to estimate the residual displacement of the 4 km baseline cavity, which is for advanced LIGO.

This chapter describes the control model and the noise analysis in detail. Section 6.1 introduces the linear control model. In section 6.2 the noise analysis for the 40-meter prototype experiment is discussed. In section 6.3 the noise estimation for advanced LIGO based on the result of the 40-meter prototype is discussed.

### 6.1 Control Model

---

In this section a model of the control system used in the steady state is presented. The control system, shown in figure 6.1, can be broken into five parts, each described in the sections below. The model includes injection points for various noise sources that might affect overall performance, discussed in detail in section 6.2.

#### 6.1.1 AUX-Cavity Loop

The first logical control loop is the Pound-Drever-Hall (PDH) lock of the frequency-doubled auxiliary (AUX) laser to the arm cavity (green block in figures 5.1 and 6.1). This loop suppresses the frequency noise of the AUX laser and allows its frequency to follow the motion of the cavity length.

## CHAPTER 6. MODELING AND NOISE ANALYSIS

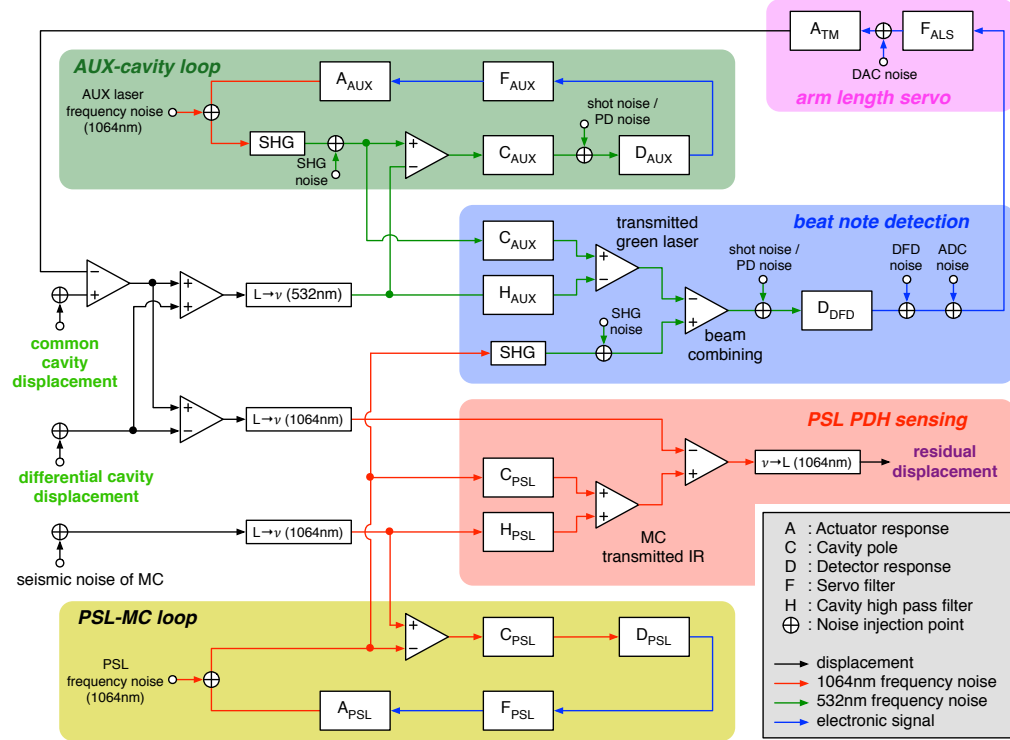


Figure 6.1: Block diagram of the model of control scheme and noise sources for the experiment. The colored blocks correspond to the colored blocks in the setup diagram in figure 5.1. The various individual control elements are described in the text and in section 6.4.

The control bandwidth of this loop is 30 kHz, limited by the laser cavity piezoelectric frequency actuator.

According to the argument in section 2.2.4 the cavity frequency response can be approximated as a single-pole low pass filter,

$$C_{AUX}(f) = \frac{1}{1 + i(f/f_c)}, \quad (6.1)$$

where  $f$  is the frequency of the signal and  $f_c$  is the cavity pole frequency, which is 18 kHz for the 532 nm AUX beam.

The photo detection and mixing process that produces the Pound-Drever-Hall (PDH) error signal has an overall flat V/Hz conversion factor given by

---

## 6.1. CONTROL MODEL

$D_{\text{AUX}}$ . The servo filter, which is tuned to provide stable and robust locking, has a frequency response of  $F_{\text{AUX}}$ . Finally, the laser frequency actuator has a response of  $A_{\text{AUX}}$ .

The noise sources associated with this loop are the AUX laser frequency noise, second-harmonic generation (SHG) noise, shot noise at the detector, and electronics noise of the readout electronics. These noise sources will be discussed in detail in section 6.2.

### 6.1.2 PSL-MC Loop

The PSL-MC (pre-stabilised laser locked to the mode cleaner) loop (yellow in figures 5.1 and 6.1) describes the lock of the PSL frequency to the MC length. The control bandwidth of this loop is 130 kHz. As with the AUX laser cavity loop, the MC cavity has a single-pole frequency response given by  $C_{\text{PSL}}$ .  $D_{\text{PSL}}$  is the response of the PDH sensing,  $F_{\text{PSL}}$  is the response of the servo filter, and  $A_{\text{PSL}}$  is the response of the PSL compound frequency actuator, which includes the laser crystal temperature actuator, laser cavity piezoelectric actuator, and electro-optic modulator (EOM) as described in section 4.3.4.

The PSL light transmitted through the MC and incident on the arm cavity under test is the reference for the performance of the cavity stabilization system. However, finite gain in the PSL-MC loop can potentially lead to PSL frequency noise coupling into the arm stabilization loop. Despite this, the model shows that the suppression ratio from PSL frequency noise to the residual displacement is more than  $10^6$  at 100 Hz, so we can safely neglect the PSL frequency noise.

### 6.1.3 Beat-note Detection

The beat-note detection block (blue in figures 5.1 and 6.1) measures the frequency difference between the AUX and frequency-doubled PSL beams.

The transmitted AUX light is a combination of the suppressed AUX laser frequency noise and any external displacement noises in the cavity that modulate the optical phase of the laser resonating in the cavity. According to the argument in section 2.2.4, the external disturbance is filtered by the cavity with a transfer function of

$$H_{\text{AUX}}(f) = \frac{i(f/f_c)}{1 + i(f/f_c)}, \quad (2.34)$$

## CHAPTER 6. MODELING AND NOISE ANALYSIS

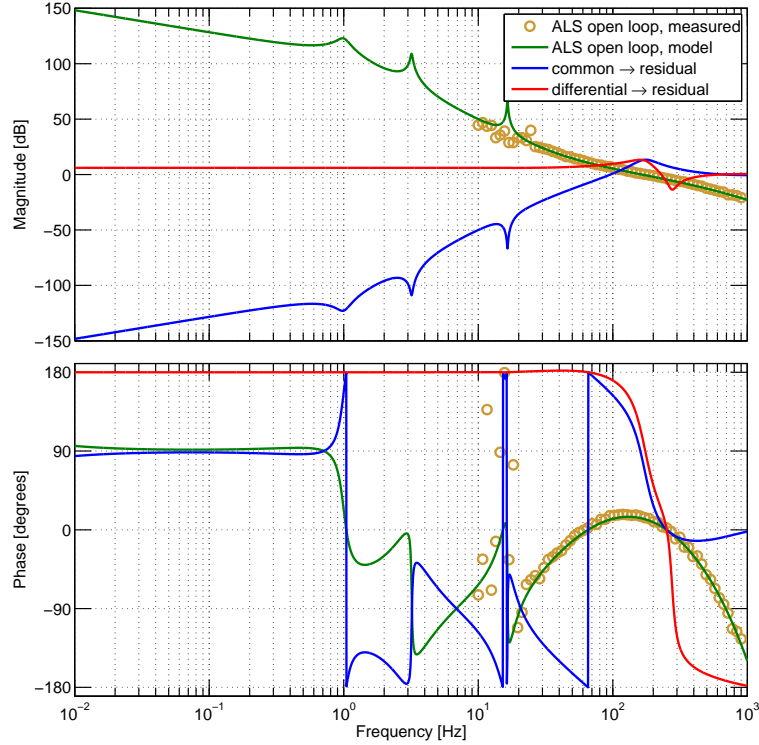


Figure 6.2: Bode plot of control model transfer functions. The green trace is the full open-loop transfer function of the arm length servo control loop. The blue and red traces are the transfer functions from external disturbances to residual displacement, for AUX/PSL common and differential sensing.

where again  $f_c = 18$  kHz.  $D_{\text{DFD}}$  represents the flat Hz $\rightarrow$ V conversion of the full beat detection process, including the gain of the radio frequency photo detector (RFPD) and the delay-line frequency discriminator (DFD).

Noise in the frequency doubling process of the PSL should be at a similar level to that in the AUX-cavity loop. Laser shot and photo-detection noises are also similar to those in AUX-cavity loop. The electronics noise in this case is from the DFD. Finally, there is also additional noise from the ADC process.

### 6.1.4 Arm Length Servo

The output of the beat-note detection process is the error signal for the arm cavity length control servo loop (pink in figures 5.1 and 6.1). The digital error signal is sent through the servo filter,  $F_{\text{ALS}}$ , which includes a 470  $\mu\text{s}$  processing delay. The resultant digital control signal is converted back to an analog voltage via a DAC, and the output analog control signal is used to actuate on the end test mass (ETM) via coil magnetic actuators ( $A_{\text{TM}}$ ). The overall open loop gain of this loop is roughly

$$G_{\text{ALS}} \simeq D_{\text{DFD}} F_{\text{ALS}} A_{\text{TM}}, \quad (6.2)$$

since the effect of the AUX-cavity loop and  $H_{\text{AUX}}$  in parallel is an overall flat frequency response that does not affect the overall open-loop gain.

When the loop is closed, fluctuations in the frequency of the beat-note are suppressed by acting on the cavity length. Any external disturbances that produce frequency shifts common to both the AUX and PSL beams will then be suppressed by the closed loop suppression factor,  $1/(1 + G_{\text{ALS}})$ , while that for the differential noise remains unsuppressed. The transfer functions between disturbances common to both wavelengths and residual displacement can be seen in figure 6.2.

### 6.1.5 PSL PDH Sensing

This block represents the direct out-of-loop measurement of the residual displacement noise of the cavity relative to the length of the MC. As opposed to the external disturbances common to the AUX and PSL beams that are suppressed by the arm length servo, any external disturbances sensed *differentially* between the AUX and PSL beams will transmit directly to this sensor and contribute to any residual displacement noise. The transfer function between differential external disturbances and residual displacement can be seen in figure 6.2.

There are noise sources here related to readout, such as ADC noise, and shot noise and dark noise in the MC transmitted photo detection process, but they are found to be insignificant relative to other noise sources and are therefore omitted.

## 6.2 Stability and Noise Analysis

---

The residual arm displacement measured in the out-of-loop PSL PDH error signal has a root mean square (RMS) of 23.5 pm, integrated from 1 kHz to 10 mHz. The amplitude spectral density and RMS of this residual displacement are shown as the solid and dashed red curves respectively in figure 6.3. The measured RMS falls below aLIGO requirement of 1.2 nm RMS [82], which corresponds to the the linewidth of the arm cavity for the 1064 nm wavelength (see section 3.4.5).

Figure 6.3 also shows the overall noise budget of the experiment, i.e. an accounting of all noise sources that are thought to affect the performance of the experiment. To determine the contribution from a particular source we first calculate, estimate, or measure the power spectrum of the noise,  $S(f)$ , at its source (designated by a  $\oplus$  in Figure 6.1), and propagate the amplitude spectrum through the control model to produce an amplitude spectrum in the “residual displacement” output. The result is

$$n(f) = X(f)\sqrt{S(f)}, \quad (6.3)$$

where  $X(f)$  is the transfer function from the noise source to the out-of-loop-measured residual displacement. In the rest of this section we will describe the contribution from each of the sources shown in Figure 6.3.

The total noise spectrum accountable from the budget is shown as the solid blue trace in figure 6.3. The fact that the blue trace lies below the red trace over much of the band indicates a discrepancy in the noise accounting. The measured displacement spectrum is limited by a  $1/f$ -shaped noise at low frequencies, and a white noise above 100 Hz. It is unknown at this time where these limiting factors originate.

Table 6.2 in section 6.4 describes all of the fundamental constants, experimental values, and material properties used in this section.

### 6.2.1 Fundamental Cavity Noise Sources

This section describes various fundamental noise sources in the cavity being measured. While most of these noises can’t be measured directly, their levels can be estimated based on analytical models of the underlying physics.

## 6.2. STABILITY AND NOISE ANALYSIS

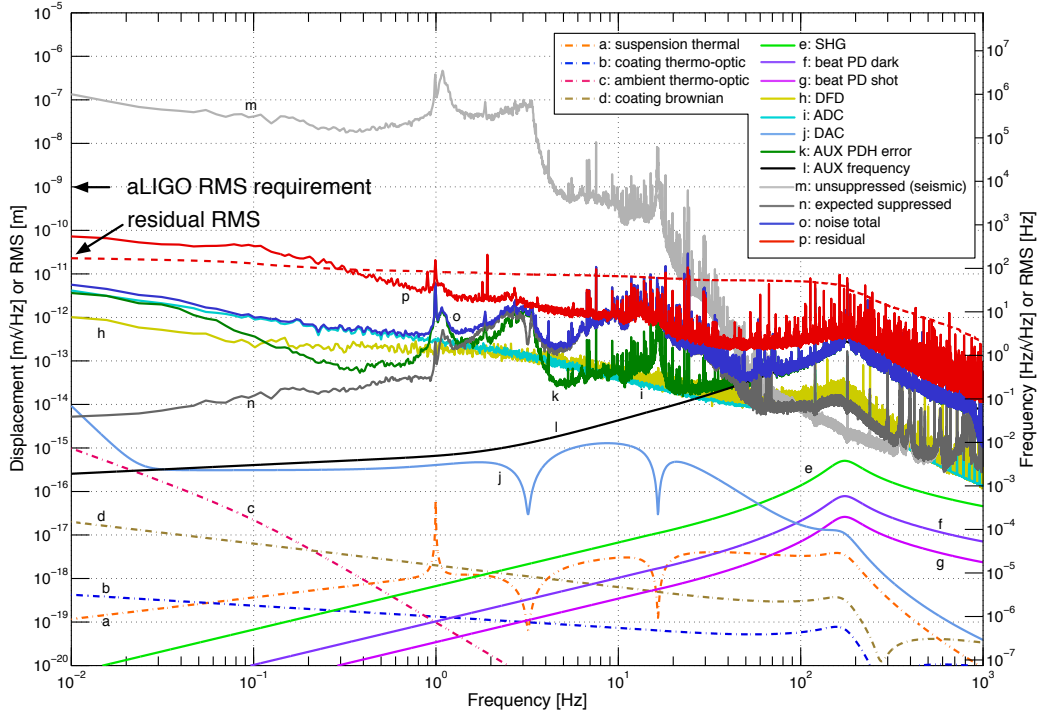


Figure 6.3: Residual displacement noise at 1064 nm, and noise budget of the locked cavity. The right vertical axis indicates the corresponding frequency noise at 1064 nm. The solid red curve is the overall residual cavity displacement measured by the out-of-loop PSL PDH detector, while the red dashed curve is the residual displacement RMS integrated from high frequency. The colored dash-dot curves represent the estimated noise contributions from various fundamental noise sources, while the solid colored curves are the measured or estimated levels of the various technical noise sources.

### Seismic Noise

Seismic noise, while dominant across much of the band of interest, is suppressed by the cavity length control loop. The light gray “unsuppressed” spectrum in figure 6.3 is an estimate of the free-swinging cavity motion,  $\sqrt{S_{\text{seis}}}$ , based on the in-loop error signal when the cavity is locked to the PSL via the PDH scheme. This spectrum is expected to be entirely dominated by seismic noise at frequencies below 100 Hz, and reaches a level of roughly  $10^{-7}$  m/ $\sqrt{\text{Hz}}$  below 1 Hz. The peak at 1 Hz is due to the pendulum resonance of the optic’s suspension system, while the peak at 3 Hz is due to the resonance of the vibration isolation stack which supports the optical table in the vacuum chamber.

The dark gray “expected suppressed” trace is the “unsuppressed” convolved with the closed-loop transfer function from the common cavity displacement input to the residual displacement. This represents the expected contribution of seismic noise to the residual displacement once the arm length servo loop is closed. Since this motion is common to both laser frequencies its contribution is suppressed by the servo to an expected level of  $\sim 10^{-12}$  m/ $\sqrt{\text{Hz}}$  across most of the band. However, it is nonetheless found to be one of the main contributors to the resultant arm displacement around 10 Hz.

### Suspension Thermal Noise

As explained in section 4.7 the cylindrical cavity mirrors are suspended from a single wire loop clamped at the top of a suspension cage. Suspension thermal noise originates from thermal fluctuation of these suspension wires and thereby displaces the position of the mirror. The noise is well modeled [34] and its power spectrum is expressed as

$$S_{\text{sus}}(f) = \frac{4k_B T}{(2\pi f)^2} \text{Re}[Y(f)], \quad (6.4)$$

where  $k_B$  is the Boltzmann constant,  $T$  is the mean temperature, and  $f$  is the frequency.  $Y$  is the admittance of the suspended mirror due to an external force and is described by the transfer function

$$Y(f) = \frac{1}{M} \frac{if/(2\pi f_p^2)}{1 + i\phi_p - (f/f_p)^2}, \quad (6.5)$$

---

## 6.2. STABILITY AND NOISE ANALYSIS

---

where  $M$  is the pendulum mass,  $f_p$  is the pendulum frequency, and  $\phi_p$  is the pendulum loss angle. As with seismic noise, this noise is common to both AUX and PSL beams because it actually displaces the position of the mirrors. Therefore its contribution is suppressed by the arm length servo.

The expected suspension thermal noise level in our experiment is shown as the dot-dashed orange curve in figure 6.3. The peak at 1 Hz is excess noise due to the pendulum resonance. The dip at 3.2 Hz is due to a resonant gain in the arm length servo used to suppress the contribution from the primary mode of the vibration isolation stack, while the dip at 16.5 Hz is resonant gain used to suppress the contribution from the bounce mode of the optic suspension.

### Coating Thermal Noise

Noises associated with thermal fluctuations in the mirror's high-reflectivity coatings are an important limiting noise source in LIGO. While they are not expected to be a notable contribution to the result, we touch on them for completeness.

There are two important coating thermal noise sources — *Brownian* noise comes from thermal vibrations associated with mechanical losses in the mirror coating. The combined *Thermo-refractive* and *thermo-elastic* noises, jointly referred to as *thermo-optic* (TO) noise, affects the laser field as it interacts with the high-reflective coating.

Unfortunately, calculating the effect of these noises in the presence multiple light wavelengths is not trivial. As mentioned in section 6.1.5, only the noises sensed differentially between the AUX and PSL beams, and therefore not suppressed by the arm length servo, will show up as residual displacement noise in our experiment. Calculating the differential effect accurately would therefore require a fully coherent analysis at both wavelengths, which is beyond the scope of this thesis. Instead we make the very naive assumption that the difference between what is sensed by the AUX and PSL beams is entirely attributable to the difference in their spot sizes on the mirror surfaces. We then calculate the differential thermal noise contributions based on this differential spot area.

The Brownian thermal noise spectrum is given by [35]:

$$S_{\text{BR}}(f) = \frac{4k_B T}{2\pi f} \frac{\phi_{\text{eff}}(1 - P^2)}{E\sqrt{a}}, \quad (6.6)$$

## CHAPTER 6. MODELING AND NOISE ANALYSIS

---

where  $P$  is the Poisson ratio of the substrate,  $\phi_{\text{eff}}$  is the effective loss angle of the coating,  $E$  is the Young's modulus of the substrate, and  $a$  is the area probed. The resultant residual displacement spectrum from coating Brownian noise in our experiment is shown as the dot-dashed brown curve in figure 6.3.

For the thermo-optic (TO) noise contribution, we follow the coherent treatment proposed in [36]. A Gaussian beam illuminating a mirror senses thermal fluctuations in the coating resulting in the noise power spectrum:

$$S_{\text{TO}}^{\Delta T}(f) = 2\sqrt{2} \frac{k_B T^2}{a\sqrt{2\pi f \kappa s}}, \quad (6.7)$$

where  $\kappa$  is the thermal conductivity, and  $s$  is the heat capacity per volume. The overall thermo-optic noise spectrum is then

$$S_{\text{TO}}(f) = S_{\text{TO}}^{\Delta T}(f) \Gamma_{\text{tc}} (\chi_{\text{fsm}} \Delta \bar{\alpha} d - \bar{\beta} \lambda)^2, \quad (6.8)$$

where  $\Gamma_{\text{tc}}$  is a correction due to the finite thickness of the coating layers,  $\Delta \bar{\alpha}$  is the difference in effective thermal expansion coefficient between the coating and substrate,  $\chi_{\text{fsm}}$  is a correction due to the finite mirror size,  $d$  is the thickness of the layers,  $\bar{\beta}$  is the effective thermo refractive coefficient, and  $\lambda$  is the beam wavelength. The residual displacement from thermo-optic noise is shown as the lower dot-dashed blue trace in figure 6.3.

### Couplings with Ambient Temperature Fluctuations

Potentially more significant than the inherent thermo optic noise contribution at low frequencies is the thermo optic contribution from low frequency ambient temperature fluctuations coupling directly to the mirror coating. Thermal fluctuations in the mirror coating due to ambient temperature fluctuations in the lab can be significantly higher than those from thermo optic excitations. These fluctuations dominate the thermo optic noise spectrum at low frequencies.

To estimate the thermo optic noise contribution from ambient temperature we start with the same thermo optic noise description in equation (6.8). But instead of using the thermo optic fluctuations from equation (6.7),  $S_{\text{TO}}^{\Delta T}$ , we instead use an estimated thermal spectrum given by:

$$S_{\delta T}^{\Delta T}(f) = [\delta T(f) C(f) j(f)]^2, \quad (6.9)$$

---

## 6.2. STABILITY AND NOISE ANALYSIS

where  $\delta T(f)$  is the amplitude spectrum of the ambient temperature fluctuations in the lab environment,

$$\delta T(f) = 3 \times 10^{-3} \left( \frac{0.01 \text{ Hz}}{f} \right) \frac{\text{K}}{\sqrt{\text{Hz}}}, \quad (6.10)$$

$C(f)$  is the transfer function through the vacuum envelope, described by a single 0.1 Hz pole, and  $j(f)$  is the radiative transfer to the optic surface,

$$j(f) = \frac{4\epsilon\sigma T^3}{2\pi\sqrt{f\kappa\rho c}}, \quad (6.11)$$

where  $\epsilon$  is the emissivity of the coating,  $\sigma$  is the Stefan-Boltzmann constant,  $T$  is the mean temperature,  $\kappa$  is the thermal conductivity of the substrate,  $\rho$  is the density of the substrate, and  $c$  is the specific heat capacity. The contribution from this effect is shown as the pink dot-dashed curve in figure 6.3.

### 6.2.2 Technical Noise Sources

This section describes the contribution from various technical noise sources that can be measured directly in the experiment.

#### Laser Frequency Noise

Frequency noise associated with the AUX and PSL lasers is generally suppressed by the control loops that keep the lasers locked to the main arm and mode cleaner cavities. However, since all control loops are coupled together at some level, there is a possibility of laser frequency noise contributing to the measured residual displacement noise.

As discussed in section 6.1.2 frequency noise from the PSL is significantly suppressed and can therefore be ignored. However, coupling from the AUX laser is at a much higher level. We estimate its contribution by observing the residual noise in the AUX PDH error signal while the AUX-cavity loop is locked. We then assume that this noise is due almost entirely to unsuppressed laser frequency noise fluctuations. The resultant contribution from this noise is the dark green “AUX PDH error” trace in figure 6.3.

In fact the “AUX PDH error” is a sum of the cavity displacement and the AUX frequency noise. Since the AUX PDH error signal observes the relative difference between the laser frequency and the arm length, the resultant spectrum can be a sum of them.

## CHAPTER 6. MODELING AND NOISE ANALYSIS

---

At the low frequencies below 20 Hz, the PDH error is dominated by the cavity displacement and therefore the features at the low frequencies is caused by the cavity displacement. On the other hand the noise is dominated by the AUX frequency noise above 20 Hz. According to the shape of the spectrum, the AUX frequency noise can be modeled by a power law as,

$$\delta f = 5 \times 10^3 \left( \frac{1 \text{ Hz}}{f} \right)^{0.8} \frac{\text{Hz}}{\sqrt{\text{Hz}}}. \quad (6.12)$$

The contribution from this noise is also shown in the black solid “AUX frequency” trace in figure 6.3. Due to the AUX-Cavity loop the noise is suppressed at low frequencies and the contribution becomes more significant as the loop gain gets smaller at high frequencies. A bump at 160 Hz corresponds to the unity gain frequency of the ALS servo above of which the servo quits injecting the AUX frequency noise.

### Second-Harmonic Generation Noise

Noise due to the second-harmonic generation process is assumed to be added to the frequency noise of the frequency-doubled laser beam. The upper limit of the noise level is assumed to be  $1 \times 10^{-5} f \text{ Hz}/\sqrt{\text{Hz}}$  [83]. Laser frequency doubling happens in two places in our experiment: in the AUX laser output and on the PSL beam for the beat-note detection. The contribution from the PSL doubling in the beat-note detection is much more significant, so it is this level that is shown as the light green curve in figure 6.3. The second-harmonic noise introduced in the AUX laser loop is suppressed by the loop gain because it can be considered as a part of the AUX laser frequency noises.

### Shot Noise and Detector Dark Noise

Both shot noise and dark noise appear as white noise (in the detection band) in the broadband radio frequency (RF) photodetectors used in the experiment. When measuring the frequency of a signal, the measured voltage noise can be converted to frequency noise on the detected signal by [84]:

$$S_{\text{PD}}(f) = \frac{2S_{\text{V}}(f)}{V_{\text{RF}}^2} f^2, \quad (6.13)$$

where  $S_{\text{V}}$  is the input-referred voltage noise, and  $V_{\text{RF}}$  is the voltage amplitude of the main RF signal.

---

## 6.2. STABILITY AND NOISE ANALYSIS

---

The most dominant contribution from these noises comes from the beat-note detection photo detector (PD). The dark current noise level of the PD used is  $12 \text{ pA}/\sqrt{\text{Hz}}$  between 10 MHz and 80 MHz. The incident power on the PD is  $200 \text{ }\mu\text{W}$  which produces  $60 \text{ }\mu\text{A}$  of DC photocurrent, corresponding to a shot noise level of  $4 \text{ pA}/\sqrt{\text{Hz}}$ . The resultant frequency noise spectra at the detector input for these noise sources are shown as the purple (dark) and magenta (shot) traces in figure 6.3.

### Frequency Discriminator Noise

The comparator in the delay-line frequency discriminator adds white noise during the process of reshaping RF signals into square waves. The noise level is measured from the output of the DFD while being driven by a pure RF sine wave. The level, referred to the input of the DFD, was found to have a total contribution of  $10^{-14} - 10^{-13} \text{ m}/\sqrt{\text{Hz}}$  after applying the loop correction factor (olive curve in figure 6.3).

### ADC Noise

ADC noise is easily measured directly by terminating the inputs to the analog filters that whiten the signal before digitization, and then measuring the spectrum digitally. The effect of the ADC whitening is compensated for within the digital system. The resultant contribution, referred to the input of the DFD, sees the same loop correction factor as the DFD (cyan trace in figure 6.3).

### DAC Noise

DAC noise is directly measured by digitally generating a 3 Hz signal, representing the peak frequency of the error signal while locked, and then measuring the output noise spectrum. The resultant noise contribution is mostly flat at a level of about  $1 \text{ }\mu\text{V}/\sqrt{\text{Hz}}$  and is shown as the pale blue curve in figure 6.3). The dips at 3.2 Hz and 16.5 Hz are due to the effect of the resonant gains stages discussed in section 6.2.1.

## **6.3 Scaling Noise Sources for aLIGO**

---

In this section we look at how various noise sources in our experiment can be scaled to aLIGO. We find that certain noise contributions will be more prominent in aLIGO due to the difference in the arm length, but they are addressed in the aLIGO design such that they should not pose a significant problem.

### **6.3.1 Residual Displacement in aLIGO**

Figure 6.4 shows the expected residual displacement and noise budget of the aLIGO arm cavity, under the following assumptions. (1) The transfer function of the control loops are the same as that used in the 40-meter prototype. (2) The level of the seismic noise is the same as that observed in the 40-meter prototype although this assumption leads to overestimation because seismic noise in aLIGO will be much quieter. (3) The level of the AUX laser frequency noise and the frequency discriminator noise are the same as that measured in the 40-meter prototype. (4) The rest of the noise sources are negligible.

As shown in figure 6.4, the contribution from the AUX frequency noise (shown as the black curve), second-harmonic generation (SHG) noise (shown as the light green curve) and frequency discriminator (DFD) noise (shown as the olive curve) become 100 times significant than that of the 40-meter prototype experiment. These noises result in a residual displacement of about 200 pm in RMS, which is close to the requirement of 1.2 nm.

#### **Frequency Noise**

From the relation between frequency noise and length fluctuations expressed in equation (3.17) we can see that the 100-times longer arm cavities of aLIGO means that aLIGO will be 100 times more sensitive to laser frequency fluctuations. For a displacement noise requirement of 1 nm RMS, the beat-note frequency stability requirement goes from 8.8 kHz in this 40-meter experiment to 83 Hz in aLIGO. This puts a much stricter requirement on the frequency noise of the AUX laser and SHG noises.

aLIGO will mitigate this issue in a couple of different ways. First, aLIGO will phase lock the AUX laser to the PSL frequency through the use of a fiber-based phase-locked loop (PLL). This will improve noise below 50 Hz, while

### 6.3. SCALING NOISE SOURCES FOR ALIGO

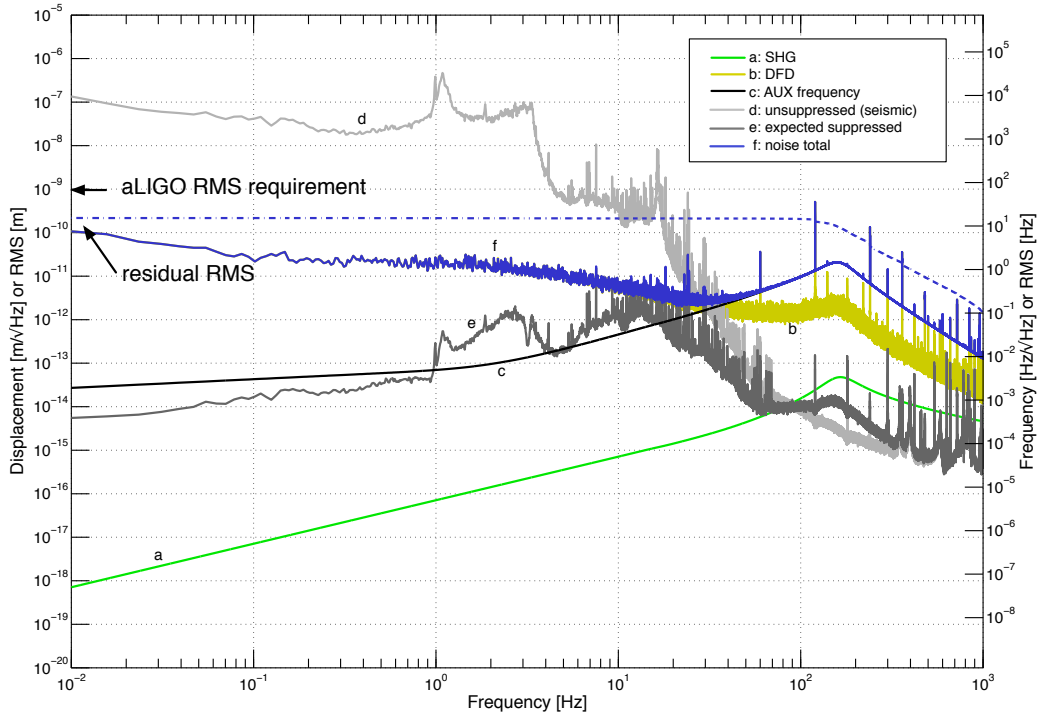


Figure 6.4: Expected residual displacement noise of the aLIGO arm, and noise budget of the locked cavity. The right vertical axis indicates the corresponding frequency noise at 1064 nm. The solid blue curve is the overall residual cavity displacement expected from the model, while the blue dashed curve is the residual displacement RMS integrated from high frequency. The residual RMS is found to be at 200 pm which is close to the requirement of 1.2 nm.

## CHAPTER 6. MODELING AND NOISE ANALYSIS

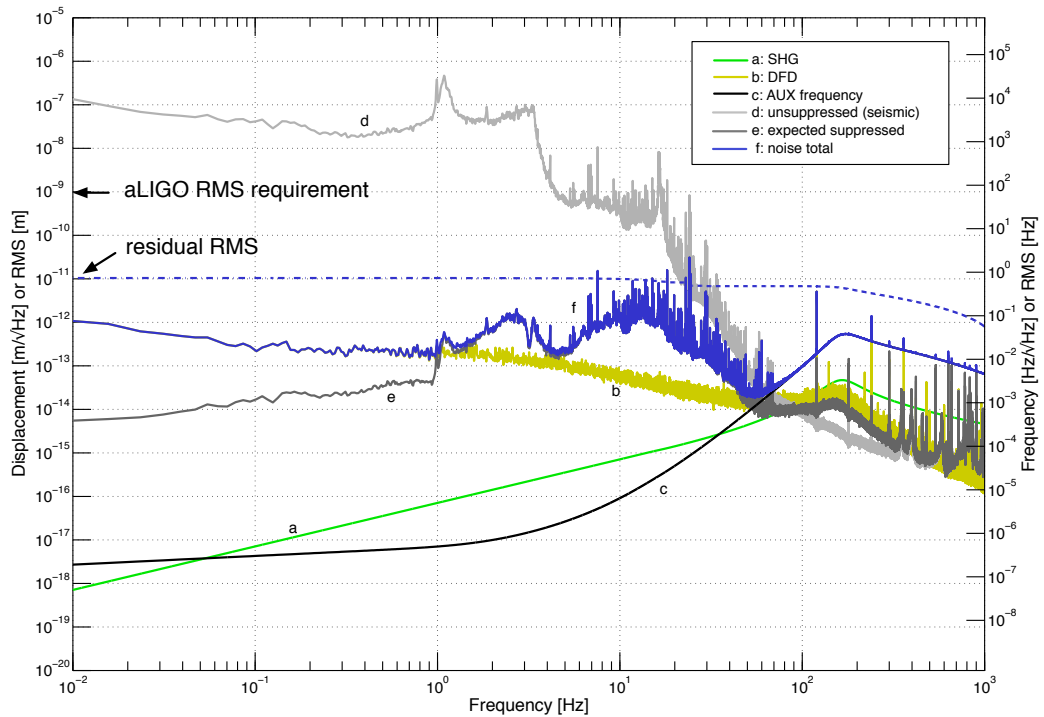


Figure 6.5: Expected residual displacement noise of the aLIGO arm, and noise budget of the locked cavity with the AUX-cavity loop improved and the DFD noise lowered by a factor of 100. The residual RMS is found to be at 10 pm, which reasonably surpasses the requirement of 1.2 nm.

---

### 6.3. SCALING NOISE SOURCES FOR ALIGO

---

it could make the noise worse at around 50 Hz. The high frequency noise can then be addressed through optimization of the servo controls. The gain of the AUX-cavity loop can be increased to suppress the excess noise from the AUX laser, and the bandwidth of the arm length stabilization loop can be decreased so that any residual noise will not be injected into the cavity motion.

#### Readout and frequency discriminator noise

Readout and electronics noise sources should become less severe in aLIGO. The interferometer response will generally grow in proportion to length, resulting in a higher signal-to-noise ratio against these noise sources.

The frequency discriminator, on the other hand, generally does not scale with the baseline length since it reads out the frequency of the beat-note rather than the optical phase. For this reason the readout noise of the discriminator will make a 100 times larger contribution to the noise budget than it does in our experiment. This can be the limiting noise source with a frequency noise level of  $1 \text{ Hz}/\sqrt{\text{Hz}}$  at 10 Hz. The situation can be improved by using a small-range discriminator such as a VCO-based PLL or a longer cable in the DFD.

Figure 6.5 shows the noise budget of aLIGO with the AUX-cavity loop improved and the frequency discriminator (DFD) noise lowered by a factor of 100. In the estimation two poles and two zeros are newly added in the AUX loop at 1 kHz and 10 Hz respectively. As a result the AUX frequency noise are further suppressed and the residual displacement is now at 10 pm. Since the unity gain frequency of the arm length loop in aLIGO can be lowered because of lesser seismic noise, the kink point of 160 Hz can be also lowered and hence it will result in a lesser contribution of the AUX frequency and SHG noise to the residual motion. Although fiber noise is not incorporated in the estimation, this result promises the feasibility of the multi-color technique in aLIGO — the arm length can be stabilised to within the linewidth.

#### Seismic length fluctuations

Length fluctuations due to seismic noise should become somewhat easier to handle in aLIGO since the test masses will be further isolated from ground vibration due to sophisticated aLIGO seismic isolation systems. Depending on how large the residual seismic fluctuations are the unity gain frequency

## CHAPTER 6. MODELING AND NOISE ANALYSIS

---

of the arm length servo loop should be able to be lowered. This is generally good since it avoids injection of undesired noises at high frequencies, such as the AUX frequency, SHG and control noises.

### 6.4 Control Model Transfer Functions

---

Table 6.1 lists all of the zeros, poles, and gains for the various control elements in the control model described in section 6.1 and figure 6.1. For a system with  $p_m$  poles and  $z_n$  zeros (both specified in Hz) and gain  $k$ , the transfer function would be given by

$$X(f) = k \frac{\prod_n (1 + if/z_n)}{\prod_m (1 + if/p_m)}. \quad (6.14)$$

In addition to the blocks represented in table 6.1, the blocks labeled “ $L \rightarrow \nu$ ” in figure 6.1 represent the conversion from displacement ( $dL$ ) to frequency ( $d\nu$ ) described in equation (3.17),

$$L \rightarrow \nu = \frac{\nu}{L}, \quad (6.15)$$

where  $\nu = c/\lambda$ .

### 6.5 Discussions and Summary of the Chapter

---

#### 6.5.1 Discussions

Although the residual displacement spectrum of the prototype test is explainable in a frequency range from 10 Hz to 30 Hz by seismic noise, noise sources which cover the residual displacement below 10 Hz and above 30 Hz are not yet identified. One clue, which was found during the test, is that the unidentified noises were still seen when the arm length control was passed to the PSL PDH sensor. In this situation the arm length is stabilised with the signal derived from the PSL PDH sensor, while the beat-note serves as an out-of-loop sensor as opposed to the standard arm length stabilisation test. According to measurements, the unidentified noise has a  $1/f$ -shape at low frequencies and becomes white noise above 30 Hz. Since the PDH sensor has a higher signal-to-noise ratio, this indicates that the noise sources can likely

## 6.5. DISCUSSIONS AND SUMMARY OF THE CHAPTER

element	zeros (Hz)	poles (Hz)	gain
$C_{\text{AUX}}$	-	18.5k	1
$D_{\text{AUX}}$	-	-	5.0e-6
$F_{\text{AUX}}$	1.0, 100, 10k	0.1m, 1.2, 2.0	2.1e8
$A_{\text{AUX}}$	-	100k	5.0e6
$D_{\text{DFD}}$	-	-	2.16e-7
$F_{\text{ALS}}$	40, 40, 1.655 ± 2.739i, 3.320 ± 16.163i	1.0m, 500, 0.052 ± 3.200i, 0.105 ± 16.500i	1.0e6
$A_{\text{TM}}$	-	0.1 ± 0.995i	8.0e7
$C_{\text{PSL}}$	-	3.8k	1
$D_{\text{PSL}}$	-	-	2.5e-5
$F_{\text{PSL}}$	4k, 20k, 20k	40, 1k, 1k	2.3e4
$A_{\text{PSL}}$	-	100k	5.0e6
SHG	-	-	2

Table 6.1: Zeros, poles and gain of the control model blocks.

be associated with the 532 nm system. We have taken various possible noise sources into account, but some practical noise sources, such as scattering noises and alignment noises, are not included. Depending on where the noise comes from, it can impacts on the arm length stability in aLIGO. Therefore this issue needs further inspections.

### 6.5.2 Summary

- A noise analysis has been conducted for the result of the 40-meter prototype test. The linear control model was built on the basis of the measurement of the actual control servos.
- The model allows to estimate the transfer function from various noise sources to the residual displacement. According to the analysis the noise contributions are well understood.
- The residual displacement was found to be 23.5 pm in root mean square, integrated from 1 kHz to 10 mHz. This reasonably surpasses the aLIGO requirement of 1.2 nm.

## CHAPTER 6. MODELING AND NOISE ANALYSIS

---

- On the basis of the prototype test, estimation of the residual displacement in aLIGO has been performed. Frequency noises become 100 times severer and they will be mitigated in aLIGO.
- The feasibility of the multi-color interferometric technique has been confirmed with the realistic control and noise model.

## 6.5. DISCUSSIONS AND SUMMARY OF THE CHAPTER

symbol	name	value	SI unit
$k_B$	Boltzmann's constant	1.38e-23	J K <sup>-1</sup>
$\sigma$	Stefan-Boltzmann constant	5.67e-8	W m <sup>-2</sup> K <sup>-4</sup>
$T$	mean temperature	290	K
$\lambda$	beam wavelength	1.064e-6	m
$M$	cavity mirror pendulum mass	0.243	kg
$f_p$	pendulum frequency	1.0	Hz
$\phi_p$	pendulum loss angle	1.7e-4	–
$P$	Poisson ratio of (substrate)	0.167	–
$E$	Young's modulus (substrate)	7.27e10	N m <sup>-1</sup>
$\kappa$	thermal conductivity	1.38	W m <sup>-1</sup> K <sup>-1</sup>
$s$	heat capacity per volume	1.62e6	m <sup>-3</sup> K <sup>-1</sup>
$c$	specific heat capacity	740	J kg <sup>-1</sup> K <sup>-1</sup>
$\epsilon$	emissivity	0.9	–
$\rho$	density	2202	kg m <sup>-3</sup>
ITM			
$\phi_{\text{eff}}$	effective coating loss angle	8.65e-8	–
$\Delta\bar{\alpha}$	effective thermal expansion difference	3.59e-6	K <sup>-1</sup>
$\bar{\beta}$	effective thermal refraction	2.35e-6	K <sup>-1</sup>
ETM			
$\phi_{\text{eff}}$	effective coating loss angle	1.24e-7	–
$\Delta\bar{\alpha}$	effective thermal expansion difference	4.54e-6	K <sup>-1</sup>
$\bar{\beta}$	effective thermal refraction	1.11e-6	K <sup>-1</sup>

Table 6.2: Values of fundamental constants, and material properties and variables for the 40m mirror coatings. If not specified, material properties are for the mirror coating.



# 7

## Conclusion and Future Directions

### 7.1 Conclusion

---

Using multi-wavelengths lasers a tractable strategy for sensing the arm cavity lengths of a complex gravitational-wave (GW) interferometer has been demonstrated. This method can be replicated and applied to any of the GW interferometer in the upcoming worldwide network such as advanced LIGO, advanced VIRGO and KAGRA.

The residual arm stability is 23.5 pm in root mean square integrated from 1 kHz to 10 mHz. This meets the requirement for advanced LIGO of 1.2 nm. With this amount of residual noise the arm lengths can be smoothly tuned to be at a desired value. Thus this ensures the feasibility of the planned full lock acquisition process.

The noise limits are now well understood and according to the noise study, the feasibility of the scheme in advanced LIGO has been confirmed. Therefore the use of this technique should allow for a significantly higher duty cycle in advanced LIGO.

### 7.2 Future Directions

---

#### 7.2.1 Application of Multi-Color Interferometry

Besides precise control of suspended Fabry-Pérot cavities, multi-wavelength readout also has the potential to improve performance of other optical systems. Here we present futuristic ideas which can potentially reduce the fundamental noise sources such as quantum noise and mirror thermal noise through the use of multi-wavelength readout, as well as an idea to precisely

## CHAPTER 7. CONCLUSION AND FUTURE DIRECTIONS

---

characterize an optical cavity.

### Multi-Wavelength Readout for Manipulating the Quantum Noise Limit

By resonating multiple laser beams with different wavelengths in a single interferometer, traditional quantum noise limits can potentially be modified.

One example is cancellation of quantum back-action for GW detectors [85]. Imagine a main carrier field resonating with high power in an interferometer arm cavity, and a low-power auxiliary laser beam with a different wavelength resonant only in the interferometer vertex (anti-resonant in the arm cavities). The high-power main carrier field would produce quantum radiation pressure noise on the test masses. The low-power auxiliary laser beam, on the other hand, would sense only the differential motion of the two input test masses, and therefore not be sensitive to GW signals. An optimal combination of the two carriers beam with Wiener filters could then be used to cancel the low-frequency back action noise, while not losing information from GWs.

Another idea is to resonate both carrier wavelengths in the arm cavities. The design of the optics could be made such that the optical properties for the different wavelengths are different leading to different frequency sensitivities for the two beams. For example, the input test masses could have higher transmittance for one wavelength over the other. By tuning different wavelengths and optimally combining their outputs, one may be able to shape the quantum noise spectrum in a much more flexible way than in the single wavelength case.

Multiple beams with different wavelengths could also potentially be used to manipulate the dynamics of test masses in optical cavities. In particular, it is well known that the multi-bounce laser fields in optical cavities modify the dynamics of the cavity mirrors via radiation pressure [28]. Under appropriate conditions this can result in modifications of the opto-mechanical coupling and a higher response against optical phase changes. For example, in GW detectors that use signal recycling cavities, two wavelengths of light appropriately detuned from the resonance of the signal-recycling cavity can result in a radiation pressure force that reduces the effective inertia of the test mass at low frequencies. This can significantly amplify the response of the interferometer to GW signals [86]. It is therefore possible that a multi-wavelength technique could allow for surpassing the standard quantum limit

over a broad frequency band.

### **Thermal Noise Estimation**

In a frequency regime where sensitivity is strongly limited by mirror thermal noise, it may be possible to use two different laser wavelengths to differentially sense the thermal noise in the two fields. It may then be possible to combine signals from the two lasers in order to yield one data stream representing the cavity length fluctuations and another with purely the thermal noise. This technique may be capable of giving a moderate decrease in the effective thermal noise. However, the differential frequency noise between the wavelengths would need to be investigated more precisely.

### **Precise Cavity Mode Characterization**

Since multi-wavelength metrology enables us to detune the laser frequency from one of the cavity resonances in a quasi-static manner, various longitudinal and spacial characteristics of the cavity can be precisely inspected. Precise scanning of a resonance can provide a measure of cavity finesse, while scanning over multiple free spectral ranges gives us a measurement of the absolute length of the cavity. The frequency spacing of transverse spatial modes can be obtained by inspecting the resonances of the fundamental and higher-order modes, therefore providing information about the cavity geometry and the figure error of the cavity optics. The power transmitted during scanning can also tell us the mode matching efficiency between an incident beam and cavity eigenmodes.

### **7.2.2 Modern Controls**

With the aid of the multi-color scheme, the arm Fabry-Pérot cavities can be controlled under any interferometric conditions for the main laser. However the remaining part of the interferometer is still controlled in a classic way and therefore engagement of this part is still probabilistic. For far-future interferometers, this part will become problematic because of the same reason as that for the arm cavities. A possible approach is to employ a modern control, which involves the machine learning and adaptive control. Perhaps such an intelligent control system may find out a proper combination of the

## **CHAPTER 7. CONCLUSION AND FUTURE DIRECTIONS**

---

signals that represents the length degrees of freedom and therefore stabilise the lengths automatically.



# Characterization of the Dual-Recycled Michelson Interferometer

From a practical point of view, the commissioning of the 2nd generation gravitational-wave (GW) interferometer can be separated into two parts — the arm cavities and dual-recycling Michelson interferometer (DRMI). In fact in the planned schedule of advanced LIGO, the commissioning of the DRMI starts in the Livingston observatory, and in parallel, the commissioning of an arm cavity starts in the Hanford observatory in this year, 2012. The main goal of these commissioning are verification of both the interferometric characteristics and mechanical characteristic, such as the suspensions. Besides the mechanical characterization, the multi-color interferometry is the main topic for the arm cavities and it has been described throughout this thesis. This chapter summarizes the other part of the commissioning, that is the DRMI.

## A.1 Overview

---

The main purpose of the dual-recycled Michelson interferometer (DRMI) commissioning includes demonstration and verification of the length sensing and control (LSC) scheme as well as verification of the performance of the suspension system. Perhaps the strong emphasis will be set on that of the suspension system, which can be precisely measured only by the interferometric means. In this context verification of the LSC should not take unnecessarily a long time such that the remaining commissioning time can be spent for the diagnosis of the suspension system and difficult (or perhaps unexpected) issues.

## APPENDIX A. CHARACTERIZATION OF THE DUAL-RECYCLED MICHELSON INTERFEROMETER

---

Prior to the commissioning works, the 40-meter prototype (see chapter 4) began characterization of the DRMI. There are two motivations. Firstly, in order to accelerate the commissioning at the LIGO sites, the procedure for the DRMI commissioning, or equivalently characterization, must be clearly summarized together with the underlying physics and reliable measurement techniques. The other motivation is, of course, the DRMI in the 40-meter prototype interferometer must be characterized before the upcoming full lock experiment.

### A.1.1 The Characterization List

In order to characterize the DRMI, the following measurements and adjustments are necessary. Some of them have been already performed at the 40-meter prototype interferometer as described in section A.5. This section summarizes the characterization list.

#### 1. Noise Budget

Producing the noise budget of the length degrees of freedom (DOFs) is essential in the GW interferometer. The noise budget must be continuously produced and monitored because the interferometer is so sensitive that a small modification could significantly degrade (or improve) the sensitivity and hence the noise budget can be used as an indicator for the health of the DRMI.

#### 2. Schnupp Asymmetry Measurement and its Adjustment

Generally there are two measurement types for measuring the asymmetry. They are categorized according to which major quantity, the amplitude or phase of a field, is measured. For the amplitude measurements, one can utilize the fact that the Michelson's power transmissivity and reflectivity are functions of the asymmetry. Therefore, for example, injecting an radio frequency (RF) amplitude modulation sidebands and measuring its transmissivity or reflectivity, one can estimate the asymmetry. For the phase measurement one can use the fact that the phase of a field rotates due to the round trip in one of Michelson's arms. Therefore measuring the difference in the phase rotations between two arms, one can estimate the asymmetry. As it will be

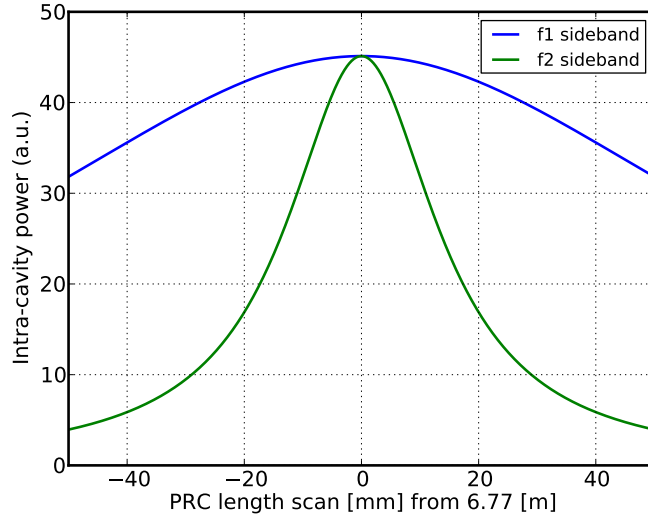


Figure A.1: PRC intra-cavity power of the sidebands against the macroscopic scan of the PRC length, calculated. The power of  $f_1$  and  $f_2$  sidebands are drawn in blue and green respectively. This is a calculation for the power-recycled Michelson interferometer (i.e. no SRM or arm cavities). In the calculation the fundamental modulation frequency of  $f_1 = 11065399$  Hz, the Schnupp asymmetry of  $l_{\text{sch}} = 0.364$  m, the transmissivity of the ITMs of  $t_i^2 = 0.0138$  and that of the PRM of  $t_p^2 = 0.056$  are assumed.

explained in section A.5.1, the latter method was chosen for the 40-meter prototype.

### 3. Recycling Cavity Lengths Measurement and their Adjustment

The lengths of the power recycling cavity (PRC) and signal recycling cavity (SRC) are critical in the sense that they can affect both the amplitude and phase of the fields, resulting in a different sensing matrix. The required precision for the PRC length is stricter than that for SRC because the linewidth of the PRC is narrower due to the fact that the PRC has a higher finesse.

A naive requirement can be set on the lengths by considering the resonant condition of the sidebands. Figure A.1 shows the PRC intra-cavity power of two sidebands as a function of the macroscopic PRC length when the power-recycled Michelson interferometer is locked. The  $f_2$  sideband has a narrower

## APPENDIX A. CHARACTERIZATION OF THE DUAL-RECYCLED MICHELSON INTERFEROMETER

---

linewidth because the phase of the  $f_2$  sideband rotates five times faster than that of the  $f_1$  sideband. If the requirement is set such that the intra-cavity power is allowed to be at 90% of its maximum, the corresponding amount in the PRC length is about 5 mm. Therefore the PRC length should be adjusted with this precision. On the other hand, the SRC length needs a precision of about 1.5 cm according to a similar macroscopic length scan.

The measurement can be done by several ways. An accurate and precise way is to introduce an additional laser, phase-locked to the main laser [87]. This technique allows one to scan the transmissivity of a cavity of interest along the frequency of the main laser when the cavity is locked to the main laser. Other techniques which don't introduce an additional laser can be found in references [88, 89, 90].

### 4. Recycling Gain Measurements

The recycling gain is a key factor in the modern GW interferometer because it determines the ultimate sensitivity. The measurement can be performed by simply measuring the intra-cavity powers. However if the mode overlap coefficient of the incident laser is far below 1, the power-build-up in the cavity also decreases and hence one would end up with wrong estimation. In fact this is the case for the 40-meter prototype at this time. The details are further described in section A.5.3.

### 5. Tuning of Locking Protocol

Tuning of the locking protocol includes the adjustment of the triggers and initial open-loop transfer function for the lengths control. Because the locking of the DRMI is nonlinear control, it is not so straightforward to quantitatively describe it. Under most of the situations, the tuning can be done empirically as it is relatively easier and faster.

Triggering can be done by using the DC photo detector (DCPD) signals for the power recycling cavity length (PRCL) and Michelson (MICH), as they couple mostly with the carrier. Or one can use the second-harmonic sidebands  $2f_1$  and  $2f_2$  as a power monitor. Some more descriptions about the triggers using the second-harmonic sideband fields can be found in section A.3.3. A special attention must be paid to a trigger for signal recycling cavity length (SRCL) because SRCL doesn't affect the carrier field and hence the  $2f_2$  demodulation must be employed.

## **6. Sensing Matrix Verification**

The sensing matrix is an important parameter in such a multiple-readout system. The sensing matrix can be used as an indicator for how precisely the interferometer is modeled. A new visualization technique is explained in section [A.2.1](#), and the experimental results are shown in section [A.5.4](#).

## **7. Measurement of Spot Positions in DRMI**

It is usually preferable to align the beam and optics in such a way that the beam hits the center of all the suspended optics. So for the reason, the spot position of each mirror needs to be measured and corrected.

If the beam is on a point off from the center of an optic, it increases the risk of beam being clipped by the lim of the optic or the structure supporting it. Moreover the angular actuators for a suspended optic are usually diagonalized such that the mirror reacts with a rotational axis crossing the center of the optic. This means a finite amount of the off-centering of the beam spot leads to undesired coupling from the angular actuator to the length, which potentially limits the ultimate sensitivity. The spot position can be measured by employing the standard dithering technique.

## **8. Calibration of Actuator responses**

Although calibration of the length actuators can be a part of the suspension commissioning, this impacts some of the measurements listed here. For example, an accurate measurement of the noise budget and sensing matrix can be done only if the calibration of the actuators are accurate. The details are described in section [A.5.2](#).

## **9. Diagonalization of LSC Output Matrix into the Canonical DOF basis**

As will be discussed in section [A.2](#) the interferometer is a multiple-input and multiple-output system. In such a complicated system, it is not practical to start from diagonalizing the input matrix. Instead the output matrix is a good starting point, as it can be straightforward in the sense that it only relies on the mechanical response of the suspensions.

As will be discussed in section [A.2.3](#), the only degree of freedom (DOF)

## APPENDIX A. CHARACTERIZATION OF THE DUAL-RECYCLED MICHELSON INTERFEROMETER

---

which needs to actuate multiple mirrors is MICH. Therefore the diagonalisation of output matrix contains only balancing of the MICH actuators.

### 10. Third Harmonic Demodulation Technique

Signals obtained by the third harmonic demodulation (THD) technique should be tested because this is a key for the full lock process (see section 3.5). The test should include the noise budget as well as the sensing matrix. Since the THD signal is inherently small compared with that associated with the fundamental modulation of  $f_1$  and  $f_2$ , one has to be careful about the noise performance so that the THD signals can hold and stabilise the DOFs with a sufficient stability during the lock progression. The measurement of the sensing matrix can be found in section A.5.4.

### 11. Measurement of Modulation Depth

The modulation depths must be monitored with an OSA or other devices. It is necessary for an accurate interferometer modeling.

## A.2 Interferometer as MIMO

---

The modern GW interferometer can be considered as a Multiple-Input and Multiple-Output (MIMO) system. The outputs from an interferometer, are obtained through the optical detection processes. These obtained signals are generally mixture of the signals associated with the canonical DOFs. Similarly, there are a number of actuation points in the interferometer and therefore one has to choose appropriate combination of those actuation points such that the length DOFs are successfully suppressed with small cross couplings.

### A.2.1 Sensing Matrix

The obtained signals from the frontal modulation scheme and the direct power measurements can be a mixture of all the length DOFs as the optical cavities are coupled to each other. If there are a number of PDs, producing the signals, the resultant set of the signals can be expressed by

$$S = \hat{M}L \tag{A.1}$$

---

## A.2. INTERFEROMETER AS MIMO

---

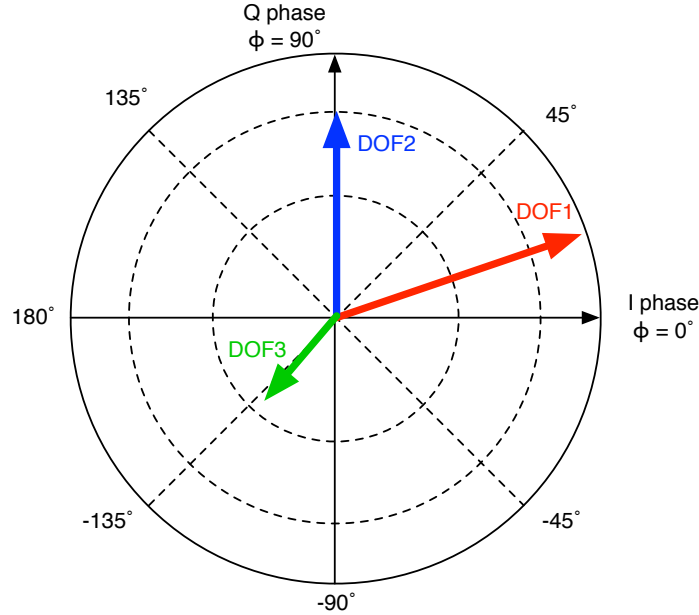


Figure A.2: The radar chart for visualization of input matrix.

where  $\mathbf{S}$  is a sensor vector containing both the I and Q signal from each PD as well as the DC power signals,  $\hat{\mathbf{M}}$  is the sensing matrix, and  $\mathbf{L}$  is the canonical length DOF. Therefore once the sensing matrix is measured one can reproduce the desired DOFs by applying the inverse of the matrix. However it is always reasonable to design the interferometer such that the matrix manipulation can be as less as possible to make the system tractable.

### A.2.2 Radar Chart

In this section we introduce a new visualization method for the sensing matrix. As explained in section 2.3.4, the demodulation scheme at a particular demodulation frequency produces two independent signals, that are in-phase (I-phase) and quadrature-phase (Q-phase) signals. Typically a custom-made PD is designed to observe one particular frequency component of an electric field as described in section A.3,

Therefore it is fair to say that a single PD produces the I and Q-signals, expect for the DCPDs. A complication arising here is that the length signal from all the DOFs show up in a single PD and each of them are with a

## APPENDIX A. CHARACTERIZATION OF THE DUAL-RECYCLED MICHELSON INTERFEROMETER

---

certain demodulation phase. Therefore under such a circumstance one can not easily estimate how much level of the desired or undesired signals are in the I-phase or Q-phase in a PD.

A comprehensive way to visualize the sensing matrix is the *radar chart* in which all the relevant DOF signals are shown in a single polar plane representing a certain PD. Figure A.2 shows an example of the radar chart for an RFPD. Each relevant DOF is drawn as an arrow, classified by color. In the figure “DOF1” is shown in red, “DOF2” in blue and “DOF3” in green. The length of the arrow represents the response of the DOF in unit of W/m. On the other hand the angle of the arrow represents the demodulation phase  $\phi_{\text{dem}}$  for its corresponding DOF. The angles is defined such that  $\phi_{\text{dem}} = 0^\circ$  corresponds to the ideal I-phase, and  $\phi_{\text{dem}} = 90^\circ$  for the ideal Q-phase.

For a practice let us discuss the example radar chart shown in figure A.2. Looking at the length of the arrows, one can find that the PD is the most sensitive to DOF1 while it is insensitive to DOF3. Looking at the angle of the arrows, one can find that the DOF2 shows up in purely Q-phase. Therefore it maybe a good strategy to take the Q-signal for controlling DOF2 in the early phase of the commissioning. Although DOF1 mostly shows up in the I-phase, some fraction of DOF1 leaks to the Q-phase as it is tilted from the pure I-phase axis. Thus one should be careful with the cross coupling.

### A.2.3 Output Matrix

Once the signals from the interferometer is diagonalized and reconstructed into the canonical DOF basis, the signals are passed to the servo filters and eventually feedback to the actuators to correct the DOFs. Before the signals are feedback to the actuation points, the DOF basis must be converted into the actuation point basis similarly to that of the input signal. The signal flow is illustrated in figure 4.11.

The output matrix converts the DOF signals into the actuator basis and hence enables us to actuate the DOF with a small cross coupling. The operation can be expressed by

$$\mathbf{x} = \hat{O}\mathbf{L}, \tag{A.2}$$

where  $\mathbf{x}$  denotes the position vector of the mirrors, and  $\hat{O}$  is the output matrix.

In the case of the DRMI, it is straightforward to feedback the PRCL signal to the PRM position and the SRCL signal to the SRM position. For the

## A.2. INTERFEROMETER AS MIMO

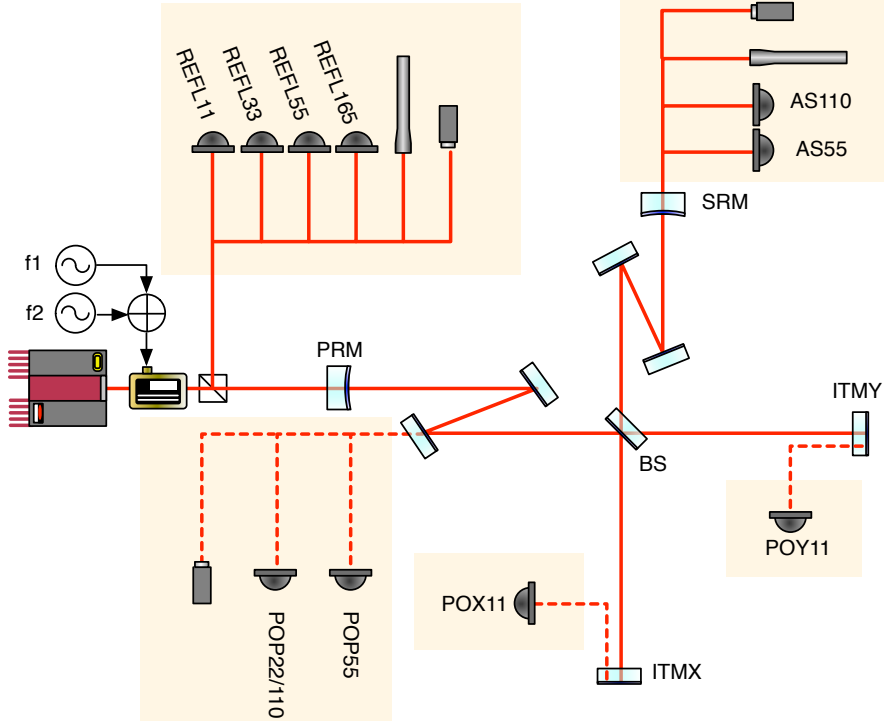


Figure A.3: Experimental arrangement of the DRMI characterization.

actuation of MICH, differential actuations on the position of ITMs can be relatively easy, because the feeding it back to BS needs to compensate the coupling to PRCL and SRCL by actuating both PRM and SRM simultaneously. In this case equation (A.2) can be expressed as

$$\begin{pmatrix} x_{\text{PRM}} \\ x_{\text{SRM}} \\ x_{\text{ITMX}} \\ x_{\text{ITMY}} \end{pmatrix} = \begin{pmatrix} 1 & 0 & 0 \\ 0 & 1 & 0 \\ 0 & 0 & 1/2 \\ 0 & 0 & -1/2 \end{pmatrix} \begin{pmatrix} L_{\text{PRCL}} \\ L_{\text{SRCL}} \\ L_{\text{MICH}} \end{pmatrix}. \quad (\text{A.3})$$

Note that, in the case of the full interferometer, this output matrix is not preferable as actuation on the ITMs leads to displacements in the arm cavities.

## APPENDIX A. CHARACTERIZATION OF THE DUAL-RECYCLED MICHELSON INTERFEROMETER

---

### A.3 Experimental Arrangement

---

Figure A.3 shows a schematic view of the experimental setup at the 40-meter prototype. The central DRMI part of the full interferometer is used for this test. Both the ETMs are misaligned such that the arm cavities don't interact with the DRMI.

The input laser is phase modulated at  $f_1$  and  $f_2$  (see table 4.1) with an electro-optic modulator (EOM). The power of the laser on PRM is estimated to about 700 mW with the transmissivity of 70% at the mode clear assumed.

A number of RFPDs are installed and their signals are demodulated at the specific frequencies. All the RFPDs are named as "PPFF", where "PPP" denotes the name of the port that the PD belongs to, and  $FF$  represents the demodulation frequency. For example, an RFPD tuned for signals at 11 MHz and placed at the REFL port, is called REFL11.

At the REFL port, four RFPDs are placed, that are REFL11, REFL33, REFL55 and REFL165. At the AS port AS55 and AS110 are placed. At the POP (Pick Off from Power recycling cavity) POP55 and POP22/110 are placed. POP22/110 is a broadband PD so that it can observe 22 and 110 MHz components. POX11 and POY11 are placed at the POX (Pick Off from ITMX) and POY (Pick Off from ITMY) port.

#### A.3.1 Macroscopic Cavity Lengths

To lock the recycling cavities, their macroscopic cavity lengths must be adjusted such that both upper and lower sidebands are simultaneously resonant to provide robust signals. This condition ensures that the carrier builds up when the arm cavities are engaged. Without the arm cavities, the recycling cavities are anti-resonant for the carrier and therefore the most of the incident field returns to the REFL port.

For PRC, the lengths are adjusted such that the upper and lower sidebands of  $f_1$  and  $f_2$  are resonant. Since the value of  $f_2$  is designed to be five times of  $f_1$ , the PRCL must satisfies,

$$f_1 = \left( \frac{1}{2} + j \right) f_{\text{FSR}}, \quad \text{(A.4)}$$

where  $j$  is an integer and  $f_{\text{FSR}}$  is the free spectral range (FSR). In the case of the 40-meter interferometer, the PRC length is limited by the available

---

### A.3. EXPERIMENTAL ARRANGEMENT

---

space confined by the vacuum envelope. As a result we chose  $j = 0$ , so that

$$L_{\text{PRCL}} = \frac{c}{4f_1} \approx 6.7 \text{ m}, \quad (\text{A.5})$$

where we used equation (2.15) to convert the FSR into a function of  $L_{\text{PRCL}}$ .

For SRC, the lengths are adjusted such that the carrier as well as the upper and lower sidebands of  $f_2$  resonate in the cavity. The idea is to let the SRCL couple mostly with the  $f_2$  sideband such that one can readout the SRCL signals from the signal of the  $f_2$  family. This solution is a mitigation to reduce the degrees of the mixture in the optical signals. Therefore the SRC length must satisfy the following condition,

$$f_2 = j f_{\text{FSR}}. \quad (\text{A.6})$$

Similarly to the PRC length, the feasible length is limited by the geometry of the vacuum envelope. So for the reason, we chose  $j = 2$ . So that

$$L_{\text{SRCL}} = \frac{c}{f_2} \approx 5.4 \text{ m}. \quad (\text{A.7})$$

The calculations shown above are valid as long as the arm cavity doesn't rotate the optical phases via the reflection, but it does in most of the cases. Therefore more precise design should be done with the presence of the arm cavities. In fact the macroscopic length of the 40-meter prototype have been designed with the effect of the arm cavities considered.

#### A.3.2 Schnupp Asymmetry

Philosophy to design the Schnupp asymmetry is to maximize the amount of the power in the  $f_2$  sidebands resonating in SRC. Such a condition enhances the signal of SRCL and is useful because the SRCL signal is one of the difficult DOFs among five. The finesse of SRC is the lowest in the optical cavities, and therefore the coupling with the fields is also the weakest. So for the reason, the SRCL signal must be enhanced by some means, or separated from the others at some level. An optimum Schnupp asymmetry [77] can be found as

$$l_{\text{sch}} = \frac{c}{2\pi f_2} \cos^{-1}(-r_{\text{PRM}}) \approx 3 \text{ cm}. \quad (\text{A.8})$$

## APPENDIX A. CHARACTERIZATION OF THE DUAL-RECYCLED MICHELSON INTERFEROMETER

---

### A.3.3 Second Harmonic Demodulation for Power Monitor

There are a few number of PDs, whose signals are demodulated at the second harmonic of the fundamental modulation frequency. The idea of demodulation at the second harmonic is that it provides the information of the intracavity powers. According to equation (2.45), the photo current at  $2\omega_m$  can be approximated by

$$i_{\text{PD}}(2\omega_m) \approx x_{-2}E_{-2}x_0^*E_0^* + x_{-1}E_{-1}x_1^*E_1^* + x_0E_0x_2^*E_2^* + \text{c.c.} \quad (\text{A.9})$$

If the carrier field is sufficiently small, it can be written as

$$i_{\text{PD}}(2\omega_m) = 2\text{Re}[x_{-1}E_{-1}x_1^*E_1^*], \quad (\text{A.10})$$

$$= 2P_1|x_1|^2. \quad (\text{A.11})$$

where  $P_1 = |E_1|^2 = |E_{-1}|^2$  is the power of the first harmonic sideband and we assumed that the  $x_1 = x_{-1}$  which is valid if either the carrier or sideband is resonant in a cavity. Therefore demodulating the photo current provides the amount of the sidebands resonating in a cavity. These signals are useful for triggering the control servos particularly for the SRCL control.

Figure A.4 shows a time stretch when the DRMI is locked. As designed, the  $f_1$  sideband in the PRC increases when the PRC and MICH are engaged and this is observed by the POP22 RFPD. Similarly the  $f_2$  sideband in SRC, which is monitored by the AS110 RFPD, increases when all the DOFs are engaged. Additionally the amount of the light at AS port becomes dramatically small because the MICH is brought to the dark fringe. The reflected light poses at a high value because the carrier light essentially doesn't enter the DRMI.

## A.4 Interferometer Modeling

---

It is essential to have a model of interferometer because all the measurements needs to be verified by models or some means. Otherwise the measured values are not going to give us any useful information.

### A.4.1 Model Interferometer

An interferometer model is built by using *Optickle* [91]. *Optickle* is a Matlab-based simulation package that enable us to simulate the frequency responses

## A.4. INTERFEROMETER MODELING

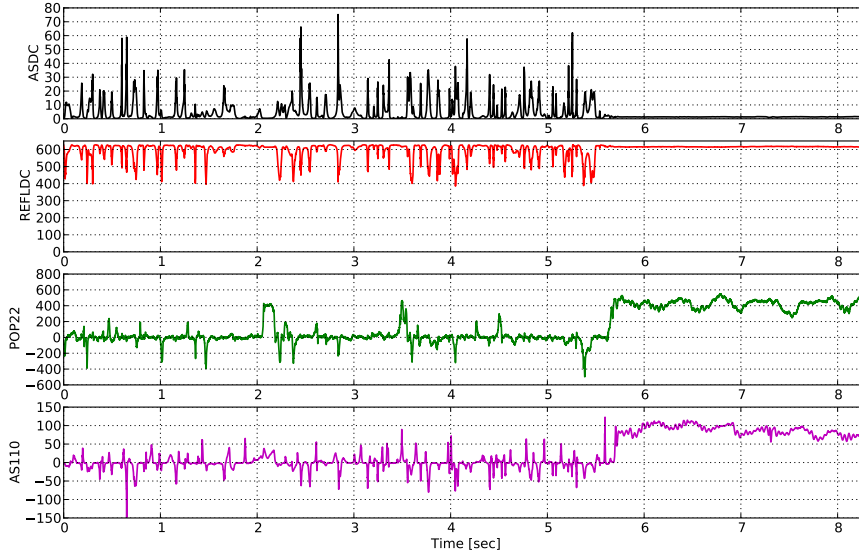


Figure A.4: Time stretch when the DRMI is locked. (top) The power of the light observed at the AS port in unit of mW. (2nd top) The power of the light observed at the REFL port in unit of mW. (3rd top) The power of the  $f_1$  sideband observed by POP22, uncalibrated. (bottom) The power of the  $f_2$  sideband observed by AS110, uncalibrated.

of a GW interferometer. Its calculation is based on the optic matrix [40] and the matrices include the elements which correspond to the necessary field components — the carrier and (higher order) sideband fields.

Figure A.5 is the predicted sensing matrix from the model. In the calculation, all the core optics are assumed to have loss of 50 ppm. To make the simulation setup more realistic, an attenuator is installed in the REFL port so that it decreases the power reaching to the PDs. Similarly an attenuator is installed also in the AS port for the same reason. The parameters used in the simulation are listed in table A.1. For the modulation frequencies and their depths, the values in table 4.1 are used.

## APPENDIX A. CHARACTERIZATION OF THE DUAL-RECYCLED MICHELSON INTERFEROMETER

---

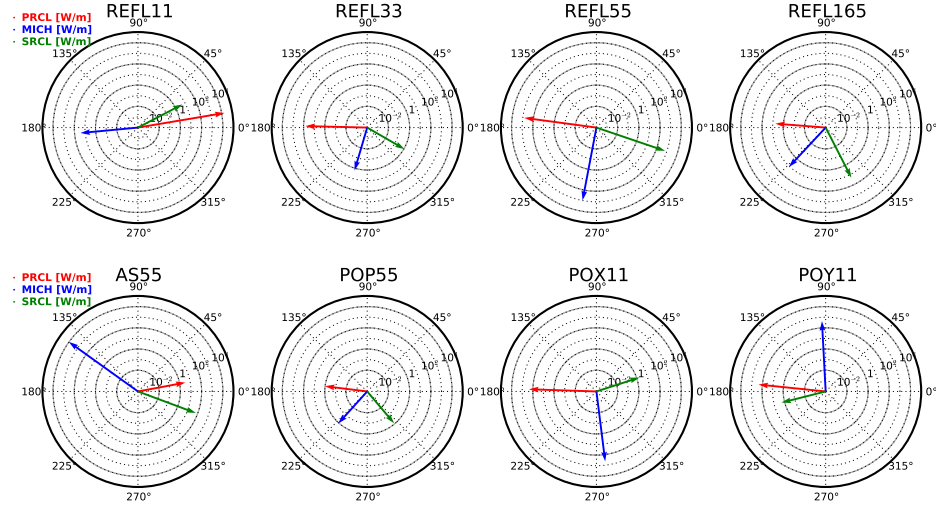


Figure A.5: Sensing matrix of the DRMI, simulated. (Red arrow) PRCL response (Blue arrow) MICH response (Purple arrow) SRCL signal. The radial axis is in unit of W/m.

### A.5 Characterization of the 40-meter Prototype

---

The commissioning of the DRMI in the 40-meter prototype interferometer has begun in the summer of 2011 and it is still on the way. In this section the results of the DRMI commissioning are described although all the items listed in section A.1.1 has not been achieved yet.

#### A.5.1 Measurement of Schnupp Asymmetry

The Schnupp asymmetry is estimated by measuring the difference between the retardation time of the light propagating in each of the Michelson's arm. In the technique two arm FP cavities are used to precisely measure the retardation. When one of the arms is locked by a demodulated signal from the AS port, its demodulation phase gives us the information about the retardation due to the fact that the field propagates the finite length of one of the Michelson's arms. Hence comparing the demodulation phase of two

## A.5. CHARACTERIZATION OF THE 40-METER PROTOTYPE

symbols	name	value	SI unit
$l_p$	PRC length	6.760	m
$l_{sch}$	Schnupp asymmetry	0.0364	m
$l_s$	SRC length	5.415	m
$T_p$	Power transmissivity of PRM	0.05637	-
$T_{BS}$	Power transmissivity of BS	0.5	-
$T_s$	Power transmissivity of SRM	0.09903	-
$R_{ar, itm}$	Power reflectivity of the anti-reflection surface of ITMs	500 ppm	-

Table A.1: Parameters, used for the model interferometer.

arms enable us to estimate the asymmetry.

The measurement was performed as follows. First of all, PRM, SRM and one of ETMs were intentionally misaligned. Then an arm cavity, say  $x$ -arm, is locked by using the signal derived from AS55. To determine the demodulation phase, the Q-phase signal was monitored because the magnitude of its response varies linearly with respect to the demodulation phase and it crosses zero when the phase is properly chosen while the I-phase signal varies quadratically. The response of the Q-phase signal can be measured by exciting the arm motion at a particular frequency and lock-in-detecting the Q-signal. After measuring the proper demodulation phases for both arms, one can obtain the difference in the demodulation phases. Thus one can estimate the asymmetry by

$$l_{sch} = \frac{c}{2\omega_{SB}} (\phi_{x,demod} - \phi_{y,demod}), \quad (\text{A.12})$$

where  $\omega_{SB}$  is the angular frequency of the RF modulation, and  $\phi_{x,demod}$  and  $\phi_{y,demod}$  denote the measured demodulation phases for the  $x$ -arm and  $y$ -arm respectively. As a result the Schnupp asymmetry was found to be  $3.64 \pm 0.32$  cm.

### A.5.2 Calibration of Coil Magnet Actuators

In order to conduct a set of the characterizations, the actuators' responses need to be calibrated. The calibration usually starts from measuring the Michelson fringe [57, 67] because the fringe pattern in its intensity and the

## APPENDIX A. CHARACTERIZATION OF THE DUAL-RECYCLED MICHELSON INTERFEROMETER

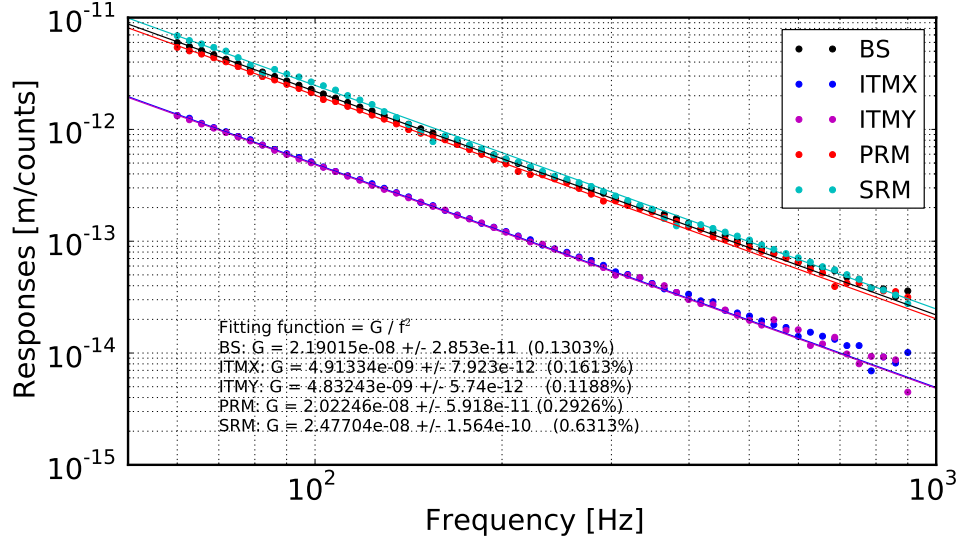


Figure A.6: AC response of the coil magnet actuators. The values listed in the plot are the fitting results.

demodulated signals at the AS and REFL ports are merely sinusoidal curves and hence relatively easy to handle. The demodulated signal can be expressed by

$$[\text{REFLQ or ASQ}] = \frac{\lambda H_{\text{MICH}}}{4\pi} \sin\left(\frac{4\pi\delta l}{\lambda}\right), \quad (\text{A.13})$$

where  $H_{\text{MICH}}$  is the optical gain of the Michelson interferometer in unit of watts per meters. Letting the Michelson freely swing, one can estimate the optical gain by measuring the peak-to-peak values. Once the optical gain is calibrated, one can proceed to a calibration of BS and ITMs by exciting them and monitoring the response.

At high frequencies, the mirrors can be approximated by a free mass, and therefore the actuator responses are approximated by,

$$A = G \times \left(\frac{1 \text{ Hz}}{f}\right), \quad (\text{A.14})$$

where  $G$  is a constant in unit of m/V or m/counts. Figure A.6 shows the

## A.5. CHARACTERIZATION OF THE 40-METER PROTOTYPE

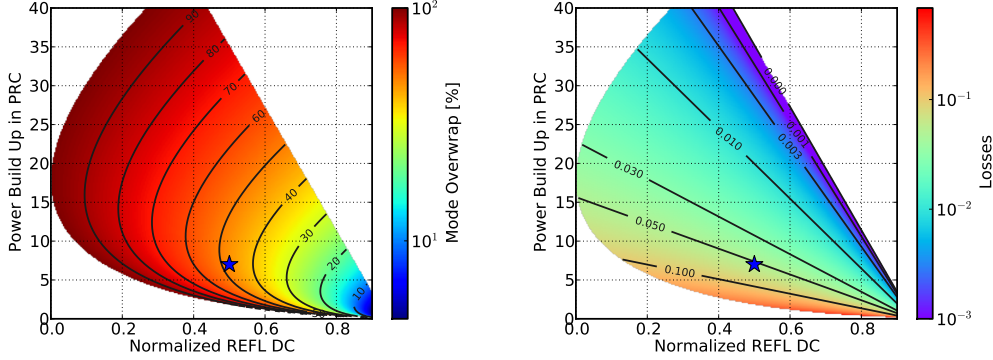


Figure A.7: Contour maps of the mode overwrap and the loss in the power recycling cavity. The  $x$ -axis is the normalized DC power at the REFL port and the  $y$ -axis is the cavity power-build-up. (Left) Contour map of the mode overwrap. (Right) Contour map of the losses in the Michelson. In both plots, a blue star indicates the measured value in the 40-meter prototype.

measured actuator responses for BS, PRM, SRM, and ITMs at high frequencies.

### A.5.3 Measurement of the Power Recycling Gain

The recycling gain of the PRC has been estimated in the following steps — (1) Measurement of the power of two specific optical fields, that are the reflected light from the cavity and the intra-cavity build up. (2) Calculation of the mode overwrap of the incident beam to the cavity and loss in the cavity based on the measured two values. (3) Estimation of the power recycling gain using the obtained loss and mode overwrap values.

To measure the power of the reflected light and power-build up, the PRC is locked on a resonance for the carrier, which can be done by flipping the sign of the PRCL control signal. During the measurement SRM and ETMs are intentionally misaligned to avoid undesired interference. The power build up  $P$ , recycling gain  $G_p$  and the measured power reflectivity of the PRC  $R_{\text{meas}}$

## APPENDIX A. CHARACTERIZATION OF THE DUAL-RECYCLED MICHELSON INTERFEROMETER

---

are related via,

$$P \equiv \zeta G_p = \zeta \frac{1 - R_p}{(1 - \sqrt{R_p R_m})^2}, \quad (\text{A.15})$$

$$R_{\text{meas}} = \zeta R_{\text{cav}} + (1 - \zeta) R_p, \quad (\text{A.16})$$

$$(\text{A.17})$$

where  $\zeta$  is the mode over wrap,  $R_p$  and  $R_m$  are the power reflectivity of the PRM and estimated Michelson respectively, and  $R_{\text{cav}}$  is the reflectivity of power-recycled Michelson interferometer defined by

$$R_{\text{cav}} = \left( \frac{\sqrt{R_m} - \sqrt{R_p}}{1 - \sqrt{R_p R_m}} \right)^2, \quad (\text{A.18})$$

Assuming that the loss comes only from the Michelson interferometer, we can define the loss as,

$$L = R_m^{(s)} - R_m, \quad (\text{A.19})$$

where  $R_m^{(s)}$  is the designed power reflectivity of the Michelson. The mode overwrap  $\zeta$  and loss  $L$  are shown in figure A.7 as a function of  $R_{\text{meas}}$  and  $P$ .

According to the measurement the DC light at the REFL port was measured to be at 50% of its maximum when the power-recycled Michelson is locked and hence  $R_{\text{meas}} = 0.5$ . The power-build-up was found to be 7 by looking at the POP DCPD. Substituting the two values into the above equations, we found the mode overwrap of  $\zeta = 47.4\%$  and the loss of  $L = 5.3\%$ . This situation corresponds to a recycling gain of  $G_p = 15$ , which is smaller than the designed value of about 40. It is unknown why the recycling gain is so small and loss is so large at this time. According to a measurement of the beam shape of the incident field, a mode overwrap of more than 95% was expected and this number contradicts the obtained mode overwrap of 47.4%. A possible hypothesis can be a clipping in the recycling cavity, which can introduce a large amount of loss and reduce the mode overwrap considerably.

### A.5.4 Verification of the Sensing Matrix

The sensing matrix was measured when the DRMI was kept locked. The measurement was performed by exciting a particular DOF at 238 Hz, at which the control servos don't affect the sensor signals, and by lock-in detecting the

## A.5. CHARACTERIZATION OF THE 40-METER PROTOTYPE

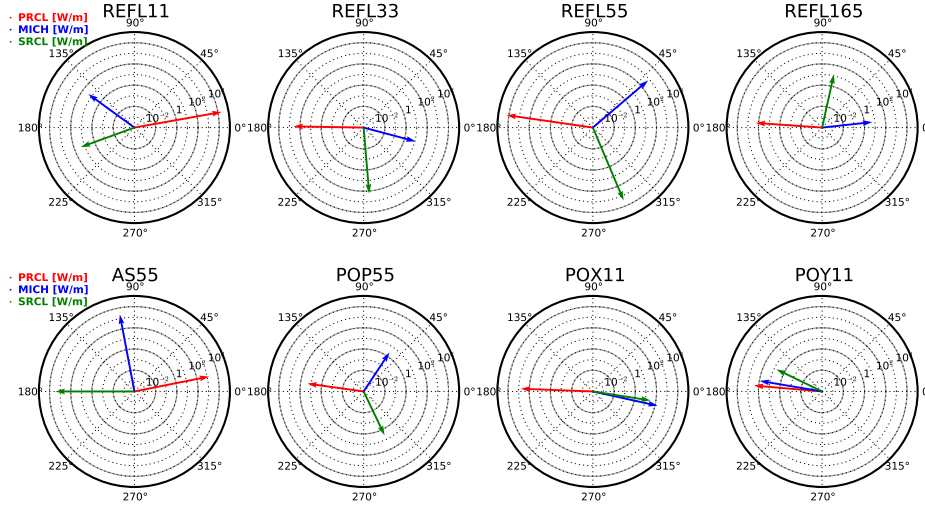


Figure A.8: Sensing matrix of the DRMI, measured. (Red arrow) PRCL response (Blue arrow) MICH response (Purple arrow) SRCL signal. The demodulation phases are rotated such that the PRCL signal shows up in the same angle as that of figure A.5. The radial scale is also the same as that of figure A.5.

signals at every ports. Figure A.8 shows a resultant sensing matrix formed by all the available RFPDs. Comparing with the expected sensing matrix shown in figure A.5, we find that the measured matrix doesn't agree with it at all. The optical gains and demodulation phases are different from that of the simulation. This needs further investigations together with the low power recycling gain issue described in section A.5.3.



# B

## Triple Resonant EOM

As described in section 4.3, it is necessary to impose phase modulations on the incident field at three different radio frequencies (RFs). A possible way to do it is to sum three RF signals electrically and then apply it on an electro-optic modulator (EOM). We call this device *triple resonant EOM*. In this chapter, the detail of the triple resonant EOM is presented.

### B.1 Modulation Methods

---

There are two methods which can impose three phase modulations with a single EOM. The first one is to attach three independent pairs of electrodes on an EOM crystal and drive each pair at a different frequency. The other solution is to drive a pair of electrodes by electrically summed signals at once. In the 40-meter prototype, the latter solution has been chosen because it could potentially make the modulation depth higher than that of the former solution as the depth is in proportion to the length of the electrodes [48].

One drawback in the single electrode method is that the impedance matching can be difficult as the impedance should be matched at three different frequencies simultaneously. On the other hand, the impedance matching in the three-electrodes method is relatively easy since the electrodes are essentially decoupled and hence they are dealt as three different circuits. In fact, so for the reason, aLIGO employs the three-electrodes method [92] with an RTP ( $\text{RbTiOPO}_4$ ) crystal.

## APPENDIX B. TRIPLE RESONANT EOM

---

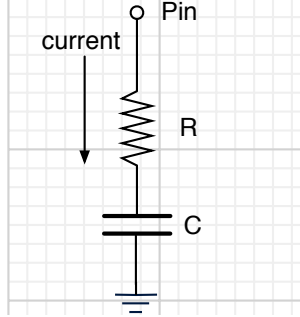


Figure B.1: Equivalent circuit of an EOM. The resistance  $R$  corresponds to the loss in the EOM and the capacitance  $C$  corresponds to the crystal.

### B.2 The Circuit

---

Since the modulation depth is generally proportional to the applied voltage across the crystal, one needs to study the electrical aspect of the EOM.

#### B.2.1 Optimally Coupled EOM

An EOM crystal can be electrically dealt as a capacitor [48, 93]. More generally, the equivalent circuit can be considered as a combination of a capacitor and resistor as depicted in figure B.1. If the EOM is optimally coupled to the RF source by a proper impedance matching, the voltage across the EOM can be expressed by

$$V_{\text{EOM}} = \frac{V_{\text{in}}}{j\omega C \sqrt{RR_0}}, \quad (\text{B.1})$$

where  $V_{\text{in}}$  is applied voltage,  $C$  is the capacitance of the crystal,  $R$  is the resistance of the crystal,  $R_0$  is the characteristic impedance (or the output impedance of a source). If the crystal doesn't have loss the voltage across the crystal can be high because there are no elements which consumes the RF power provided from the source.

Loss can be characterized by the  $Q$ -value defined as,

$$Q \equiv \frac{\text{Im}[Z]}{\text{Re}[Z]}, \quad (\text{B.2})$$

where  $Z$  is the impedance of the equivalent circuit. To characterize losses in the triple resonant circuit,  $Q$ -value is used.

## B.2. THE CIRCUIT

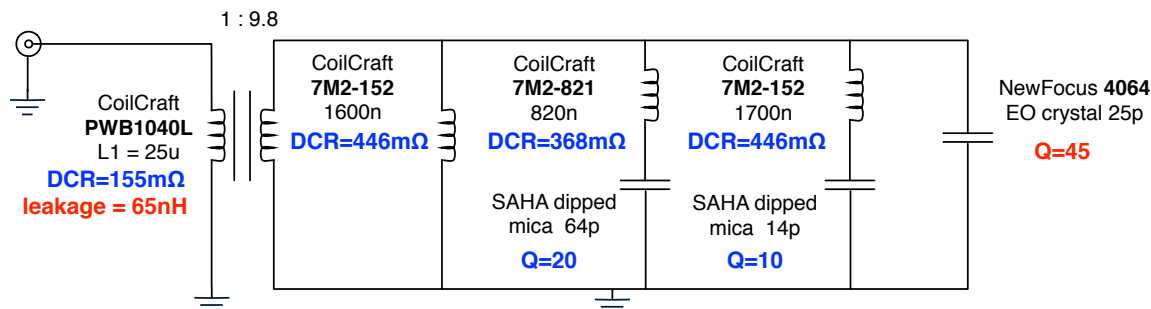


Figure B.2: Schematic of the designed circuit for the triple resonant EOM. The values in blue are losses according to the data sheets. The values in red are losses according to measurements. A three-way RF power combiner (Mini-Circuit ZFSC-3-13), which is attached to the input side of the circuit, is not shown in this schematic.

### B.2.2 The Designed Circuit

The triple resonant circuit consists of a transformer and resonant circuit formed by  $L C$  combinations as show in figure B.2. In the design, the EOM itself is included as a part of the resonant circuit. The value of each element is chosen to achieve high gains at 11, 29.5 and 55 MHz. The addition of a transformer not only provides a step-up of the voltage across the crystal, but also performs impedance matching.

In this circuit configuration, generally the value of components can not uniquely be chosen. In fact scaling each component by a factor of  $k$  allows us to change the values while the resonant frequencies remain the same [94]. For instance one can increase all the capacitances as  $C \rightarrow Ck$  and also decrease all the inductances as  $L \rightarrow L/k$ , resulting in the same resonant frequencies. However a small factor for  $k$  is preferable because the modulation depth is determined by the capacitance of the crystal according to equation (B.1). So for the reason, it is necessary to keep  $k$  as small as possible in order to obtain a high amplification.

The number of turns ratio  $n$  in the transformer can be chosen at the end of the design phase to achieve a proper impedance matching. A trans-

## APPENDIX B. TRIPLE RESONANT EOM

---

former decreases the input impedance of the circuit  $Z_{\text{circuit}}$  by  $n^2$ , so that the resultant input impedance  $Z_{\text{in}}$  is expressed by

$$Z_{\text{in}} = \frac{Z_{\text{circuit}}}{n^2}. \quad (\text{B.3})$$

The objective at this point is to make the input impedance closer to the characteristic impedance of  $50 \Omega$ . Since the transformer steps up the voltage by  $n$ , it is desired to make  $Z_{\text{circuit}}$  as high as possible or equivalently make the losses as small as possible. In the current design,  $n = 9.8$  is chosen because it brings  $Z_{\text{in}}$  to a range of  $10\text{-}50 \Omega$  at the three frequencies.

### B.3 Performance Test

---

A modulation depth was measured with an optical spectrum analyzer by scanning the frequency of the voltage applied on the triple resonant EOM. Figure B.3 shows the result when the applied voltage is fixed at  $1 \text{ V}$  in root mean square (RMS). Gains of about 9 and 8 are achieved at 11 and 55 MHz respectively compared with the raw response of  $13 \text{ mrad/V}_{\text{rms}}$ .

Since the triple resonant EOM forms a voltage divider with the output impedance of the source, the expected voltage across the EOM can be estimated from the measured input impedance,

$$V_{\text{EOM}} = \frac{2nZ_{\text{in}}}{Z_0 + Z_{\text{in}}} V_{\text{in}}, \quad (\text{B.4})$$

where  $Z_{\text{in}}$  is the input impedance of the triple resonant EOM. By multiplying a modulation efficiency of  $13 \text{ mrad/V}_{\text{rms}}$  to the above equation, one can estimate the modulation depths. The expected depth is also drawn in the figure as the dashed curve. The height of each resonance is well agreed with that of the expected curve and their shapes are well matched below 50 MHz. The discrepancy at around 55 MHz is not understood, but it could be due to a stray capacitance in the measurement device. According to the loss model as shown in figure B.2, a limiting factor for the peak height is losses in the circuit — all of them contributes to reduction of the peak height at each resonance more or less.

---

### B.3. PERFORMANCE TEST

---

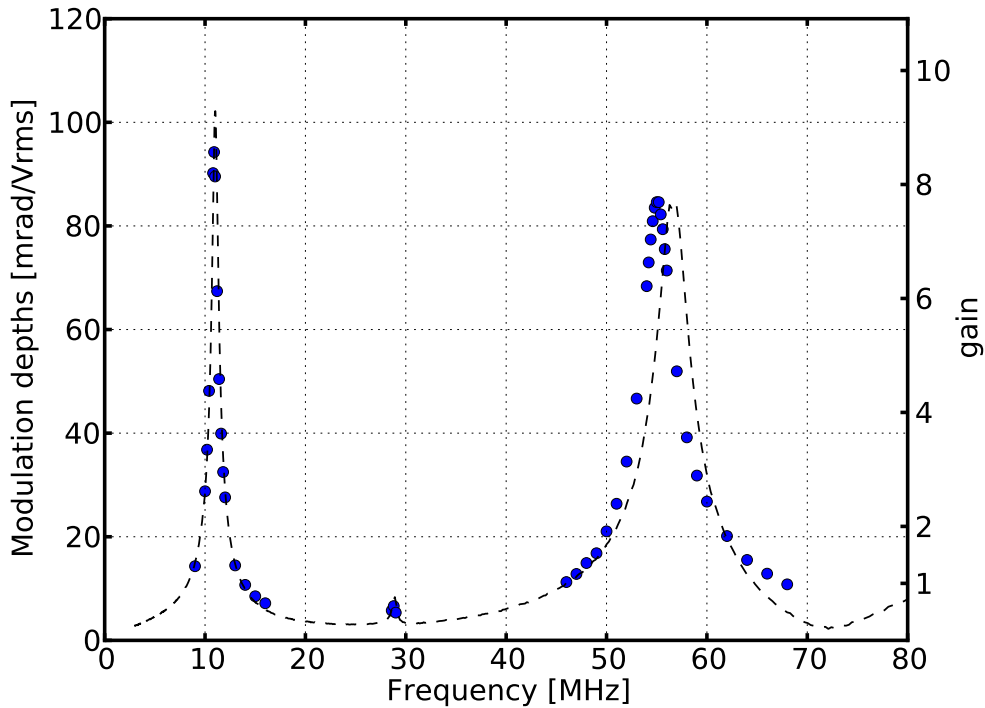


Figure B.3: The measured modulation depth as a function of the input frequency. The  $x$ -axis is frequency in MHz. The  $y$ -axis in the lefthand side is normalized modulation depths in unit of  $\text{rad}/V_{\text{rms}}$ , and that of the righthand side represents the corresponding gains. (Dots) the measured depths. (Dashed curve) the expected depth estimated from the observed input impedance of the circuit.



# Acknowledgement

It was quite lucky for me that I was able to work at the Caltech LIGO 40-meter laboratory for  $\sim 2.5$  years.

First of all, I am grateful to professor Rana Adhikari for hiring me and giving me an honorable mouse hat.

I thank professor Masa-Katsu Fujimoto for giving me an attractive and instructive talk about gravitational-wave when I was a under-graduate student.

I am grateful to Dr. Koji Arai who has supervised me for a long time of approximately 5 years without complaining. I learned most of the interferometric techniques from him.

I would like to thank the people who have worked with me at the 40-meter laboratory – Steve Vass, Bob Taylor, Daphen Pino, Rob Ward, Jamie Rollins, Aidan Brooks, Suresh Doravari, Joe Betzwieser, Alberto Stochino, David Yeaton-Massey, Jenne Driggers, Zach Korth, Den Martynov, Kevin Kuns, Joon Ho Lee and Larisa Thorne. These people are really nice.

I would like to thank the Caltech LIGO people – Alan Weinstein, Eric Gustafson, Hiro Yamamoto, Frank Seifert, Alastair Heptonstall, Jan Harms, Vladimir Dergachev, Greg Ogin, Leo Singer, Tara Chelermongsak, Haixing Miao and Eric Quintero.

I would like to thank the people who visited the laboratory and helped me out — Hartmut Grote, Valera Frolov, Bryan Barr, Katrin Daphl, Mirko Prijatelj, Yuta Michimura, John Miller, Matt Evans, Lisa Barsotti, Chris Wipf, Keiko Kokeyama and Anamaria Effler.

I thank my parents and grandmother for allowing me to do the research.

I would like to express my gratitude to my wife, Rie, who has patiently supported me and often took me out of the laboratory in holidays.



# Bibliography

- [1] A. Einstein. *Preuss. Akad. Wiss. Berlin Sitzber*, (1918).
- [2] A. Einstein. “The Foundation of the General Theory of Relativity”. *Annalen der Physik*, 49, (1916).
- [3] R. A. Hulse, J. H. Taylor. “Discovery of a pulsar in a binary system”. *Astrophysical Journal Letters*, 195:L51–L53, (1975).
- [4] J. Taylor, J. Weisberg. “Further experimental tests of relativistic gravity using the binary pulsar PSR 1913+ 16”. *The Astrophysical Journal*, 345:434–450, (1989).
- [5] M. Valtonen *et al.* “A massive binary black-hole system in OJ 287 and a test of general relativity”. *Nature*, 452(7189):851–853, (2008).
- [6] M. Ando, the TAMA Collaboration. “Current status of the TAMA300 gravitational-wave detector”. *Classical and Quantum Gravity*, 22(18):S881, (2005).
- [7] H. Lück *et al.* “Status of the GEO600 detector”. *Classical and Quantum Gravity*, 23:S71, (2006).
- [8] F. Acernese *et al.* “The Virgo status”. *Classical and Quantum Gravity*, 23:S635, (2006).
- [9] A. Abramovici *et al.* “LIGO: The Laser Interferometer Gravitational-Wave Observatory: The Laser Interferometer Gravitational-Wave Observatory”. *Science*, 256(5055):325–333, (1992).
- [10] K. Kuroda *et al.* “Large-scale cryogenic gravitational wave telescope”. *International Journal of Modern Physics D*, 8:557–579, (1999).
- [11] J. Abadie *et al.* “Predictions for the rates of compact binary coalescences observable by ground-based gravitational-wave detectors”. *Classical and Quantum Gravity*, 27(17):173001, (2010).
- [12] A. J. Mullavey *et al.* “Arm-length stabilisation for interferometric gravitational-wave detectors using frequency-doubled auxiliary lasers”. *Opt. Express*, 20(1):81–89, (2012).
- [13] K. Izumi *et al.* “Multicolor cavity metrology”. *J. Opt. Soc. Am. A*, 29(10):2092–2103, (2012).

## BIBLIOGRAPHY

---

- [14] B. Schutz. “A first course in general relativity”. Cambridge University Press, (1985).
- [15] S. L. Shapiro, S. A. Teukolsky. “Black holes, white dwarfs, and neutron stars”. Wiley-VCH, (1983).
- [16] M. Maggiore. “Gravitational waves”. Oxford University Press, (2008).
- [17] C. Cutler, D. E. Holz. “Ultrahigh precision cosmology from gravitational waves”. *Phys. Rev. D*, 80:104009, (2009).
- [18] “ATNF pulsar online catalogue”. <http://www.atnf.csiro.au/research/pulsar/psrcat/>.
- [19] B. Abbott *et al.* “Beating the Spin-Down Limit on Gravitational Wave Emission from the Crab Pulsar”. *The Astrophysical Journal Letters*, 683(1):L45, (2008).
- [20] The LIGO Scientific Collaboration and The Virgo Collaboration. “An upper limit on the stochastic gravitational-wave background of cosmological origin”. *Nature*, 460(7258):990–994, (2009).
- [21] J. Weber. “Gravitational-Wave-Detector Events”. *Phys. Rev. Lett.*, 20:1307–1308, (1968).
- [22] R. Forward. “Wideband laser-interferometer gravitational-radiation experiment”. *Physical Review D*, 17(2):379–390, (1978).
- [23] N. Mio, M. Ohashi, editors. “Study report on gravitational wave antenna technology -Handbook on interferometer- (in Japanese)”. Ministry of Education, Culture, Sports, Science and Technology, (1992).
- [24] P. R. Saulson. “Fundamentals of Interferometric gravitational wave detectors”. World Scientific, (1994).
- [25] R. W. P. Drever. “Fabry-Perot cavity gravity-wave detectors in The detection of gravitational waves”, pages 306–328. Cambridge University Press, (1991).
- [26] B. J. Meers. “Recycling in laser-interferometric gravitational-wave detectors”. *Phys. Rev. D*, 38:2317–2326, (1988).
- [27] J. Mizuno. “Comparison of optical configurations for laser-interferometric gravitational-wave detectors”. PhD thesis, Universitat Hannover, (1995).
- [28] A. Buonanno, Y. Chen. “Quantum noise in second generation, signal-recycled laser interferometric gravitational-wave detectors”. *Phys. Rev. D*, 64:042006, (2001).

---

## BIBLIOGRAPHY

---

- [29] A. Buonanno, Y. Chen, N. Mavalvala. “Quantum noise in laser-interferometer gravitational-wave detectors with a heterodyne readout scheme”. *Phys. Rev. D*, 67:122005, (2003).
- [30] J. Abadie et al. “A gravitational wave observatory operating beyond the quantum shot-noise limit”. *Nature Physics*, 7(12):962–965, (2011).
- [31] M. Punturo et al. “The Einstein Telescope: a third-generation gravitational wave observatory”. *Classical and Quantum Gravity*, 27(19):194002, (2010).
- [32] C. Caves. “Quantum-Mechanical Radiation-Pressure Fluctuations in an Interferometer”. *Physical Review Letters*, 45(2):75–79, (1980).
- [33] C. Caves. “Quantum-mechanical noise in an interferometer”. *Physical Review D*, 23(8):1693–1708, (1981).
- [34] G. González. “Suspensions thermal noise in the LIGO gravitational wave detector”. *Classical and Quantum Gravity*, 17(21):4409, (2000).
- [35] G. M. Harry et al. “Titania-doped tantala/silica coatings for gravitational-wave detection”. *Classical and Quantum Gravity*, 24(2):405, (2007).
- [36] M. Evans et al. “Thermo-optic noise in coated mirrors for high-precision optical measurements”. *Phys. Rev. D*, 78:102003, (2008).
- [37] D. J. Schroeder. “Astronomical Optics”. Academic Press, 2nd edition, (1999).
- [38] M. Rakhmanov. “Dynamics of Laser Interferometric Gravitational Wave Detectors”. PhD thesis, California Institute of Technology, (2000).
- [39] R. Drever et al. “Laser phase and frequency stabilization using an optical resonator”. *Applied Physics B: Lasers and Optics*, 31(2):97–105, (1983).
- [40] A. Freise, K. Strain. “Interferometer Techniques for Gravitational-Wave Detection”. *Living Reviews in Relativity*, 13:1, (2010).
- [41] L. Schnupp. “Internal modulation schemes”. In *Presented at the European Collaboration Meeting on Interferometric Detection of Gravitational Wave, Sorrento, Italy*, (1988).
- [42] K. Arai et al. “New signal extraction scheme with harmonic demodulation for power-recycled Fabry-Perot-Michelson interferometers”. *Physics Letters A*, 273(1-2):15–24, (2000).
- [43] D. A. Kleinman. “Theory of Second Harmonic Generation of Light”. *Phys. Rev.*, 128:1761–1775, (1962).

## BIBLIOGRAPHY

---

- [44] P. A. Franken *et al.* “Generation of Optical Harmonics”. *Phys. Rev. Lett.*, 7:118–119, (1961).
- [45] J. A. Armstrong *et al.* “Interactions between Light Waves in a Nonlinear Dielectric”. *Physical Review*, 127:1918, (1962).
- [46] P. D. Maker *et al.* “Effects of Dispersion and Focusing on the Production of Optical Harmonics”. *Phys. Rev. Lett.*, 8:21–22, (1962).
- [47] J. A. Giordmaine. “Mixing of Light Beams in Crystals”. *Phys. Rev. Lett.*, 8:19–20, (1962).
- [48] A. Yariv. “Optical Electronics in Modern Communications”. Oxford University Press, 5th edition, (1997).
- [49] S. Somekh, A. Yariv. “Phase-matchable nonlinear optical interactions in periodic thin films”. *Applied Physics Letters*, 21:140, (1972).
- [50] K. Goda. “Development of Techniques for Quantum-Enhanced Laser-Interferometric Gravitational-Wave Detectors”. PhD thesis, Massachusetts Institute of Technology, (2008).
- [51] S. Greenstein, M. Rosenbluh. “Dynamics of cw intra-cavity second harmonic generation by PPKTP”. *Optics Communications*, 238(4–6):319 – 327, (2004).
- [52] A. E. Siegman. “Lasers”. University Science, (1986).
- [53] G.-D. Xu *et al.* “Third-harmonic generation by use of focused Gaussian beams in an optical superlattice”. *Optical Society of America Journal B*, 20:360, (2003).
- [54] C. Zhang, Y.-Q. Qin, Y.-Y. Zhu. “Perfect quasi-phase matching for the third-harmonic generation using focused Gaussian beams”. *Optics Letters*, 33:720, (2008).
- [55] J. Camp *et al.* “Guided lock acquisition in a suspended Fabry-Perot cavity”. *Optics Letters*, 20:2463, (1995).
- [56] A. Yoichi. “Active Vibration Isolation for a Laser Interferometric Gravitational Wave Detector using a Suspension Point Interferometer”. PhD thesis, University of Tokyo, (2006).
- [57] R. Adhikari. “Sensitivity and Noise Analysis of 4 km Laser Interferometric Gravitational Wave Antennae”. PhD thesis, Massachusetts Institute of Technology, (2004).

## BIBLIOGRAPHY

---

- [58] F. Acernese *et al.* “Lock acquisition of the central interferometer of the gravitational wave detector Virgo”. *Astroparticle Physics*, 21(5):465–477, (2004).
- [59] K. Tochikubo. “Development of a 300-m Fabry-Perot cavity with automatic alignment”. PhD thesis, University of Tokyo, (1999).
- [60] M. Rakhmanov. “Doppler-Induced Dynamics of Fields in Fabry -Perot Cavities with Suspended Mirrors”. *Applied Optics*, 40:1942, (2001).
- [61] Y. Aso *et al.* “Stabilization of a Fabry-Pérot interferometer using a Suspension-Point Interferometer”. *Phys. Lett. A*, 327, (2004).
- [62] K. Numata, J. Camp. “Interferometric testbed for nanometer level stabilization of environmental motion over long time scales”. *Appl. Opt.*, 47(36):6832–6841, (2008).
- [63] R. W. P. Drever. “Outline of a Proposed Design for a First Receiver for Installation in the Long-Baseline Facilities, of Fabry-Perot Type”. LIGO Document T870001, (1987).
- [64] M. Evans *et al.* “Lock acquisition of a gravitational-wave interferometer”. *Optics Letters*, 27(8):598–600, (2002).
- [65] M. Evans. “Lock Acquisition in Resonant Optical Interferometers”. PhD thesis, California Institute of Technology, (2002).
- [66] O. Miyakawa *et al.* “Lock Acquisition Scheme For The Advanced LIGO Optical configuration”. *Journal of Physics: Conference Series*, 32:265–269, (2006).
- [67] R. L. Ward. “Length Sensing and Control of a Prototype Advanced Interferometric Gravitational Wave Detector”. PhD thesis, California Institute of Technology, (2010).
- [68] D. A. Shaddock. “Digitally enhanced heterodyne interferometry”. *Opt. Lett.*, 32(22):3355–3357, (2007).
- [69] O. P. Lay *et al.* “Coherent range-gated laser displacement metrology with compact optical head”. *Opt. Lett.*, 32(20):2933–2935, (2007).
- [70] S. Miyoki, S. Telada, T. Uchiyama. “Expansion of linear range of Pound-Drever-Hall signal”. *Appl. Opt.*, 49(28):5217–5225, (2010).
- [71] K. Agatsuma *et al.* “Direct Measurement of Thermal Fluctuation of High-Q Pendulum”. *Physical Review Letters*, 104(4), (2010).

## BIBLIOGRAPHY

---

- [72] L. Barsotti, M. Evans. “Lock Acquisition Study for Advanced LIGO”. LIGO Document T1000294-v1, (2010).
- [73] B. Slagmolen *et al.* “Advanced LIGO Arm Length Stabilisation System Design”. LIGO Document T0900144-v4-D, (2010).
- [74] K. Goda *et al.* “A quantum-enhanced prototype gravitational-wave detector”. *Nature Physics*, 4(6):472–476, (2008).
- [75] O. Miyakawa *et al.* “Measurement of optical response of a detuned resonant sideband extraction gravitational wave detector”. *Phys. Rev. D*, 74:022001, (2006).
- [76] R. L. Ward *et al.* “DC readout experiment at the Caltech 40m prototype interferometer”. *Classical and Quantum Gravity*, 25(11):114030, (2008).
- [77] A. Stochino. “Design and Characterization of Optical Cavities and Length Sensing and Control System of an Advanced Gravitational Wave Interferometer”. PhD thesis, Universita’ di Siena, (2010).
- [78] J. E. Geusic, H. M. Marcos, L. G. Van Uitert. “Laser oscillations in nd-doped yttrium aluminum, yttrium gallium and gadolinium garnets”. *Applied Physics Letters*, 4(10):182–184, (1964).
- [79] T. J. Kane, R. L. Byer. “Monolithic, unidirectional single-mode Nd: YAG ring laser”. *Optics Letters*, 10(2):65–67, (1985).
- [80] J. Driggers, J. Rollins. “Advanced Suspension Diagnostic Procedure”. LIGO Document G1101001-v1 (internal), (2011).
- [81] S. Schilt *et al.* “Frequency discriminators for the characterization of narrow-spectrum heterodyne beat signals: Application to the measurement of a sub-hertz carrier-envelope-offset beat in an optical frequency comb”. *Review of Scientific Instruments*, 82(12):123116, (2011).
- [82] B. Slagmolen *et al.* “Adv. LIGO Arm Length Stabilisation Requirements”. LIGO Document T0900095-v2, (2009).
- [83] D. Yeaton-Massey, R. X. Adhikari. “A new bound on excess frequency noise in second harmonic generation in PPKTP at the  $10^{-19}$  level”. *Opt. Express*, 20(19):21019–21024, (2012).
- [84] D. H. Wolaver. “Phase-Locked Loop Circuit Design”. PTR Prentice Hall, (1991).

---

## BIBLIOGRAPHY

---

- [85] H. Rehbein *et al.* “Local readout enhancement for detuned signal-recycling interferometers”. *Phys. Rev. D*, 76:062002, (2007).
- [86] F. Khalili *et al.* “Negative optical inertia for enhancing the sensitivity of future gravitational-wave detectors”. *Phys. Rev. D*, 83:062003, (2011).
- [87] A. Stochino, K. Arai, R. X. Adhikari. “Technique for in situ measurement of free spectral range and transverse mode spacing of optical cavities”. *Appl. Opt.*, 51(27):6571–6577, (2012).
- [88] A. Araya *et al.* “Absolute-Length Determination of a Long-Baseline Fabry-Perot Cavity by Means of Resonating Modulation Sidebands”. *Appl. Opt.*, 38(13):2848–2856, (1999).
- [89] M. Rakhmanov, M. Evans, H. Yamamoto. “An optical vernier technique for in situ measurement of the length of long Fabry-Pérot cavities”. *Measurement Science and Technology*, 10(3):190, (1999).
- [90] M. Rakhmanov *et al.* “Characterization of the LIGO 4 km Fabry-Perot cavities via their high-frequency dynamic responses to length and laser frequency variations”. *Classical and Quantum Gravity*, 21(5):S487, (2004).
- [91] M. Evans. “Optickle”. LIGO Document T070260, (2007).
- [92] V. Quetschke. “Electro Optic Modulators and Modulation for Enhanced LIGO and beyond”. LIGO Document G080406, (2008).
- [93] G. Heinzl. “Advanced optical techniques for laser-interferometric gravitational-wave detectors”. PhD thesis, Max Planck Institute Fur Quantenoptik, (1999).
- [94] K. Izumi. “Development of triple resonant EOM for advanced detectors”. LIGO Document G1000297-v1, (2010).